THERMAL RADIO EMISSION FROM THE SURFACES OF VENUS AND MERCURY

by

Bruce Douglas Chapman

A.B. University of California, Berkeley

(1981)

Submitted to the Department of Earth, Atmospheric, and Planetary Sciences

in Partial Fufillment of the Requirements of

the Degree of

DOCTOR OF PHILOSOPHY

at the

MASSACHUSETTS INSTITUTE OF TECHNOLOGY

SEPTEMBER 1986

© Massachusetts Institute of Technology 1986

Signature of Author _____
Department of Earth, Atmospheric, and Planetary Sciences
July 16, 1986

Certified by _____
is Supervisor

Accepted by _____
Chairman, Department Committee on Graduate Students

MASSACHUSETTS INSTITUTE OF TECHNOLOGY
JUL 1986
LIBRARIES

WITHDRAWN
FROM
MIT LIBRARIES

Abstract

The thermal radio emission from the surfaces of Venus and Mercury has been measured with the Very Large Array. Observations of Venus at a wavelength of 20 and 6 cm confirm the Pioneer Venus radiometric measurements which found regions of low emissivity associated with the highland regions of Aphrodite Terra, Beta Regio, and Maxwell Mons. The λ = 20 cm VLA observations indicate emissivities as low as 0.56 $\pm$ 0.05 for Maxwell and 0.62 $\pm$ 0.07 for Aphrodite, in agreement with the reflectivity and emissivity determined from Pioneer Venus measurements. Observations of Mercury by the VLA show substantial brightness temperature variations over the disk resulting from the solar insolation, as expected.

The disk-averaged brightness temperature of Venus at λ = 20 cm was found to be 623 $\pm$ 28 K on October 3, 1983 and 615 $\pm$ 45 K on November 12, 1983. These brightness temperatures correspond to emissivities of 0.84 $\pm$ 0.03 and 0.83 $\pm$ 0.06 , respectively, for a physical surface temperature of 734 K. At λ = 6 cm, the disk-averaged brightness temperature of Venus was 635 $\pm$ 15 K on November 12, 1983. The disk-averaged brightness temperature of Mercury at λ = 6 cm was found to be 337 $\pm$ 16 K on April 5, 1985, when Mercury was near inferior conjunction. At λ = 2 cm, the disk-averaged brightness temperature of Mercury was 320 $\pm$ 6 K on April 4, 1985. The brightness temperature variation over the disk of Mercury exceeded 100 K at both wavelengths.

Polarization measurements were made concurrently with the total intensity measurements. The average degree of polarization reached 13% at the limb of Mercury, and 14% at the limb of Venus. The degree of polarization of Mercury is consistent with a dielectric constant of 2.1 $\pm$ 0.2, while the degree of polarization of Venus is consistent with a dielectric constant of 2.5 $\pm$ 0.5. These values are significantly smaller than those indicated by radar measurements, and by the VLA emissivity measurements of this thesis, probably because of surface roughness.

The low emissivities found for Maxwell and Aphrodite suggest that the surface of these regions is characterized by a very high dielectric constant (as high as 24). These high dielectric constants may be a result of inclusions of conducting minerals (such as pyrites) in the surface at those locations.

Thesis Supervisor : Gordon H. Pettengill

Title : Professor of Planetary Physics

Acknowledgements

I would like to thank Gordon H. Pettengill for his support and supervision of the research undertaken for this thesis. His insight, intuition, and experience were indispensible assets , and his advise and direction were the driving forces behind much of this work.

I would also like to thank Peter G. Ford, who often provided valuable computer expertise (especially regarding image processing), in addition to taking the time to explain in detail various aspects of the Pioneer Venus radar experiment, and its results.

I would like to thank David Staelin for his suggestions regarding the interpretation of the low emissivities found at the highland areas of Venus, and for his ideas concerning the polarization results.

I would like to thank the staff at the Very Large Array, particularly Pat Crane and Rick Perley, for their advise and assistance. I would also like to thank Alan Bridle for scheduling time for me at Charlottesville.

I would like to thank Doug Mink and G. Kaplan for providing some of the source positions used in the observations.

I would like to thank my past and present officemates, Rich Wagner, Niall Slowey, and Laurence Page, whose friendship, advise, and encouragement were greatly appreciated.

I would like to thank my parents, Frances Chapman and Lynn Chapman, for allowing me to pursue my interests early on in life, and for their continuing support.

Most of all, I would like to thank my wife, Andrea, whose love, encouragement, and companionship were sorely needed at times. Without her internal energy and support, this thesis might not have been realized.

Table of Contents

1. Introduction..... 11

2. Data Reduction and Observational Results..... 16

2.1 Observing Strategy..... 16

2.2 Data Calibration..... 20

2.3 Image Construction..... 22

2.4 Results of Observations..... 25

2.4.1 Visibility Measurements - General Comments..... 27

2.4.1.1Visibility Measurements - Venus Data..... 31

2.4.1.2 Visibility Measurements - Mercury Data..... 35

2.4.2 Stokes I maps - General Comments..... 38

2.4.2.1Stokes I maps - Venus data..... 41

2.4.2.2Stokes I maps - Mercury data..... 56

2.4.3 The Polarization Intensity Maps..... 64

2.5 Reliability of Images..... 71

3. Polarization Properties..... 73

3.1 Theory..... 73

3.2 Comparison with Observations - General Comments..... 79

3.2.1 Comparison with Observations - Mercury Data..... 82

3.2.2 Comparison with Observations - Venus Data..... 87

3.3 Discussion of Results..... 102

4. Deduced Results 103

4.1Emissivity of the Venus Surface 103

4.1.1 λ = 20 cm Observations 106

4.1.2 λ = 6 cm Observations 110

4.2 Surface Temperatures and Emissivities of Mercury 112

4.3 Physical Interpretation of the Results 115

4.3.1 Comparison with Radar Measurements 115

4.3.2 Comparison with Models of the Surface 119

4.3.3 Physical Interpretations 121

5. Conclusions 123

Appendix 125

A1 Brightness Temperature Calculations 125

A2 Relationship between the Ratio of Emission Coefficients and η 126

A3 Corrections to λ = 6 cm Data 130

A4 Calculated Visibilities of a Disk 132

References 136

Biographical Note 144

List of Figures

Figure	Page	Description
2-1	29	The typical location in the uv plane of the visibility measurements. Points plotted are for the October 3, 1983 dataset.
2-2	32	Visibility data versus the projected spacing y/λ, where y is the projected spacing and λ is the wavelength, for the data obtained October 3, 1983 at λ = 20 cm of Venus.
2-3	33	November 12, 1983 λ = 20 cm Venus visibility data.
2-4	34	November 12, 1983 λ = 6 cm Venus visibility data (model added to data between y/λ = 0 and 7000 wavelengths.
2-5	36	April 4, 1985 λ = 2 cm Mercury visibility data.
2-6	37	April 5, 1985 λ = 6 cm Mercury visibility data.
2-7	42	Contour-grey scale plot of Venus - October 3, 1983 λ = 20 cm.
2-8	43	Planetocentric coordinates corresponding to figure 2-12. Stipled area is not illuminated by the sun.
2-9	44	Histogram of T_B for figure 2-12.
2-10	45	Brightness temperature of each pixel of figure 2-12 versus azimuth angle counterclockwise from South.
2-11	47	Contour-grey scale plot of Venus - November 12, 1983 λ = 20 cm.
2-12	48	Planetocentric coordinates corresponding to figure 2-17 and 2-21. Stipled area is not illuminated by the sun.
2-13	49	Histogram of T_B for figure 2-17.
2-14	50	Brightness temperature of each pixel of figure 2-17 versus azimuth angle counterclockwise from South.

Figure	Page	Description
2-15	52	Contour-grey scale plot of Venus - November 12, 1983 λ = 6 cm.
2-16	53	Histogram of T_B for figure 2-21.
2-17	54	Brightness temperature of each pixel of figure 2-21 versus azimuth angle counterclockwise from South.
2-18	55	Average brightness temperature versus azimuth angle counterclockwise from South for both Venus November 12, 1983 λ = 20 cm and λ = 6 cm data. λ = 20 cm data indicated by x's, λ = 6 cm data by circles.
2-19	57	Contour-grey scale plot of Mercury - April 4, 1985 λ = 2 cm.
2-20	58	Planetocentric coordinates corresponding to figure 2-25 and 2-29. Stipled area is not illuminated by the sun.
2-21	59	Histogram of T_B for figure 2-25.
2-22	60	Average brightness temperature versus azimuth angle counterclockwise from South for Mercury April 4, 1985 λ = 2 cm.
2-23	61	Contour-grey scale plot of Mercury - April 5, 1985 λ = 6 cm.
2-24	62	Histogram of T_B for figure 2-29.
2-25	63	Average brightness temperature versus azimuth angle counterclockwise from South for Mercury April 5, 1985 λ = 6 cm.
2-26	66	Polarization intensity of Venus on October 3, 1983 at λ = 20 cm.
2-27	67	Polarization intensity of Venus on November 12, 1983 at λ = 20 cm.
2-28	68	Polarization intensity of Venus on November 12, 1983 at λ = 6 cm.
2-29	69	Polarization intensity of Mercury on April 4, 1985 at λ = 2 cm.
2-30	70	Polarization intensity of Mercury on April 5, 1985 at λ = 6 cm.
3-1	76	Polarization ellipse
3-2	82	Contour-grey scale plot of the degree of polarization of the emissions from the surface of Mercury on April 5, 1985 at λ = 6 cm.

Figure	Page	Description
3-3	83	The degree of polarization (m) versus arcseconds from the center of the disk for the April 5, 1985 λ = 6 cm Mercury dataset. Theoretical curves for the expected m (convolved with a gaussian corresponding to the resolution) for dielectric constants of 2, 3, 4, and 5 have also been drawn.
3-4	88	Contour-grey scale plot of the degree of polarization of the emissions from the surface of Venus on October 3, 1983 at λ = 20 cm.
3-5	89	The degree of polarization (m) versus arcseconds from the center of the disk for the October 3, 1983 λ = 20 cm Venus dataset. Theoretical curves for the expected m (convolved with a gaussian corresponding to the resolution) for dielectric constants of 2, 3, 4, and 5 have also been drawn.
3-6	96	Contour-grey scale plot of the degree of polarization of the emissions from the surface of Venus on November 12, 1983 at λ = 20 cm.
3-7	97	The degree of polarization (m) versus arcseconds from the center of the disk for the November 12, 1983 λ = 20 cm Venus dataset. Theoretical curves for the expected m (convolved with a gaussian corresponding to the resolution) for dielectric constants of 2, 3, 4, and 5 have also been drawn.
4-1	105	Topographic map of the surface of Venus
4-2	108	Emissivity versus azimuth angle measured counterclockwise from South for Venus October 3, λ = 20 cm data.
4-3	109	Emissivity versus azimuth angle measured counterclockwise from South for Venus November 12, 1983 λ = 20 cm data.
4-4	114	Average brightness temperature versus azimuth angle counterclockwise from South for both Mercury observations (λ = 6 cm and λ = 2 cm). Circles indicate λ = 2 cm data, while boxes indicate λ = 6 cm data.
A-1	129	Geometry of transmission
A-2	131	The ratio of the expected brightness temperature at λ = 20 cm and at λ=6 cm versus the atmospheric attenuation coefficient at a) λ = 20 cm and b) λ = 6 cm, and versus c) the emissivity of the surface.

Figure	Page	Description
A-3	124	Theoretical visibility function for a disk versus $\beta = yR/\lambda D$, where y is the projected interferometer spacing, λ is the wavelength, R is the radius of the planet, and D is the distance to the planet. Curves are for zero spacing fluxes of 4.4 to 5.8 Jy incremented 0.1 Jy.
A-4	125	Theoretical disk visibility function versus β for zero spacing fluxes of 0.3 to 0.75 Jy and 0.9 to 1.1 Jy incremented 0.05 Jy.
A-5	126	Theoretical visibility versus β corresponding to figure 2-8, of zero spacing fluxes ranging from 4.4 to 5.8 Jy incremented 0.1 Jy.

List of Tables

2-1	Observational data.....	19
2-2	Observational planetary characteristics.....	26
2-3	β's corresponding to observed visibility nulls.....	30
2-4	Summary of Results of Observations.....	39
2-5	Noise level of maps.....	40
3-1	Mercury April 5, 1985 λ = 6 cm degree of polarization.....	84
3-2	Venus October 3, 1983 λ = 20 cm degree of polarization.....	90
3-3	Venus November 12, 1983 λ = 20 cm degree of polarization....	98

Chapter 1. Introduction

Passive remote sensing from the Earth of the other planets in our solar system at radio wavelengths is critically dependent on the angular resolution of the observations. Low resolution observations have the highest potential signal to noise ratio. However, if significant brightness variations occur on a scale less than the resolution, it may be desirable to increase the resolution at the expense of signal to noise. While relatively low resolution radio observations have yielded precise measurements of the brightness temperatures of planetary surfaces and atmospheres, and have helped establish the physical characteristics of the planets, high resolution observations are required if an investigation is to be made of the smaller than global scale surface features that may exist. Given the enormous apertures necessary to achieve resolutions of even one arcsecond at centimeter wavelengths, and given the small angular size of a planet, interferometry is the most practical method for high resolution mapping of radio emissions from the planets.

Radio-wavelength observations of the planets, particularly of Venus and Mercury (with which this thesis will concern itself), are complemented by ongoing radar studies. Radar observations give us a unique perspective on these worlds, as less than half of Mercury's surface has been reliably mapped at visible wavelengths (due to its proximity to the sun, distance, and limited coverage by the Mariner 10 spacecraft encounter) and virtually none of Venus' surface (due to its perpetual cloud cover) . Observations of Venus by radar, both spacecraft and Earth-based, have provided detailed maps of the topography and surface reflectivity. Radar observations of Mercury have not yet been pursued quite as vigorously, but optical and infrared images have been made of portions of its surface during spacecraft flybys.

Spacecraft visits to Venus and Mercury have considerably improved understanding of these planets. *In situ* measurements of the composition of the Venus atmosphere and surface, optical imagery of the surface of Mercury, and radar altimetry and reflectivity mapping of the surface of Venus are among the spacecraft achievements.

Earth-based radio observations of Venus and Mercury, however, in addition to being free from mission schedules, allow a greater potential flexibility in the measurements. As with Earth-based radar measurements, radio observations may be made with existing instruments at a variety of wavelengths, resolutions, and planetary illuminations, distances, and orientations. The particular parameters of an observing session will depend on the nature of the emissions that are being investigated.

Troitskii (1954) and Heiles and Drake (1963) recognized that the polarization of the radio emissions from the surfaces of planets depends upon the dielectric constant of the emitting layer, and upon the angle between the direction of propagation and the normal to the surface. For instance, the enhanced polarized emission observed towards the limb of a planet indicates that the radiation originates in the surface of that planet rather than from its atmosphere. This effect was, in fact, observed from Venus at a wavelength of 21 cm (Heiles and Drake, 1963; Clark and Spenser, 1964; Pollack and Sagan, 1965) and, subsequently, from the Moon (e.g. Davies and Gardner, 1964) and from Venus at a wavelength of 10.6 cm (Clark and Kuz'man, 1965). In order to resolve the polarized emission, the observations were made using radio interferometers. Most of these polarization measurements suggested lower values for the dielectric constant than had been found by radar methods. In 1972, high resolution interferometric observations at several wavelengths of the polarized emission from Venus indicated a significant discrepancy between the observed data and that predicted by the theoretical model (Berge, Muhleman, and Orton, 1972; Muhleman, Orton, and Berge, 1979) assuming values of the dielectric constant obtained by radar measurements.

Observations of the polarized emission from Mercury (Cuzzi, 1973; Cuzzi, 1974) at a wavelength of 3.71 cm indicated a low value for the dielectric constant, but a Monte Carlo analysis of surface roughness effects found that the observations were, nevertheless, compatible with a reasonable value for the dielectric constant.

Observations of the Venus radio spectrum have demonstrated that at wavelengths greater than about 4 cm, the emissions arise predominantly from the surface. At wavelengths less than 4 cm, the emissions are dominated by radiation from the atmosphere (Muhleman, Orton, and Berge, 1979) . There are also indications that, at wavelengths longer than about 20 cm, the brightness temperature falls off more rapidly than would be expected (Condon, Jauncey, and Yerbury, 1973; Muhleman, Berge, and Orton, 1973). The brightness temperature has been found to range from 400 K at 1 cm to 700 K at 10 cm, and back down to 500 K at wavelengths greater than 20 cm (Warnock and Dickel, 1972). Previous radio observations of the Venus surface at a wavelength of 11.1 cm have indicated a variation of 18 K in brightness temperature depending on illumination (Goldstein, 1972).

The spectrum of Mercury's radio emission has been measured by different investigators at several wavelengths and at varying solar illuminations. The variations with phase of the brightness temperature have been used to develop a thermal model that provides iteratively a measure of the inverse thermal inertia $(\kappa\rho c)^{-1/2}$ where κ is the total thermal conductivity, and ρc is the heat capacity per unit volume; and the loss tangent $\tan \Delta = \lambda\kappa_\lambda /(2 \pi \varepsilon^{1/2})$ (Where λ is the wavelength, κ_λ is the power absorption coefficient, and ε is the dielectric constant) (Morrison, 1969; Morrison, 1970; Morrison and Klein, 1970; Cuzzi, 1973; Cuzzi, 1974). These thermal parameters characterize the epilith of the planet from which conclusions have been drawn about the composition of the top surface layer. The disk averaged brightness temperature of Mercury at various wavelengths indicates that Mercury is, thermophysically, similar to the Moon (Morrison and Klein, 1970; Cuzzi, 1974).

Radar observations of the planets have been reviewed by Evans (1969) and Pettengill (1978), who describe how surface imagery, topography, reflectivity, scattering characteristics, and radar cross section may be derived from radar measurements. Ground-based observations of Venus have revealed a radar specific cross section that increases

from 0.02 at a wavelength of 3.8 cm to 0.15 at a wavelength of 23 cm, and a surface whose rms slopes range from 3.7° to 6.6°, depending on wavelength, and whose surface reflectivity is 0.15 ± 0.03, with variations in scattering, reflectivity, and topography readly apparent in imaged regions (Pettengill, 1978). Ground-based observations of Mercury, which is a far more difficult target, have indicated a radar cross section of 0.06 over a wavelength of 3.8 cm to 70 cm, and rms slopes of 6° to 9.7°, in close correspondence with the values found for the Moon. Because of low echo strengths, only relatively crude information on the distribution of reflectivity and altitudes has been obtained (Pettengill, 1978; Zohar and Goldstein, 1974).

Spacecraft observations of Venus and Mercury have provided information about those planets that would be impossible to determine from Earth. For instance, the Pioneer Venus atmopheric probes measured the thermal profile of the atmosphere during their descent (Seiff *et al*, 1980). The Venera mission to Venus provided high resolution radar observations of the Northern hemisphere (Alexandrov *et al*, 1986). Mariner 10 imaged over a third of the surface of Mercury, revealing a heavily cratered surface not unlike the Moon's (Wood and Head, 1976). Spacecraft missions have clearly made substantial contributions to understanding these and other planets in our solar system.

Many results from the Pioneer Venus spacecraft have been used during the research of this thesis. In particular, observations of radar reflectivity, topography, and radio emission have been used extensively in interpreting the data. The altimetry data revealed three topographic regions : upland rolling plains, highlands, and lowlands (Masursky et al, 1980). The data also indicated that a strong correlation exists between altitude and surface roughness (Pettengill et al, 1980). A mean value for the reflectivity of 0.12 ± 0.03, corresponding to a dielectric constant of 4.2 ± 0.8, was found for Venus; in the highlands, values of reflectivity average 0.28 ± 0.07, corresponding to a dielectric constant of 11 ± 4, and occasionally reached as high as 0.4 (Pettengill, Ford, and Nozette, 1982).

Radio emissivities as low as 0.54 ± 0.05 were found for these same regions (Ford and Pettengill, 1983).

The objective of the research presented here was to produce high resolution maps of the thermal radio emission from the surfaces of Venus and Mercury. In particular, by determining the emissivity of the highland areas of Venus, we hoped to confirm and extend the Pioneer Venus data in those regions. In addition, previous polarization observations of the planets, though noisy and of low resolution, have indicated anomalously low values for the bulk dielectric constant of the surface of Venus. Observations of Mercury were undertaken, despite the difficulty of the observations stemming from its small angular size and proximity to the Sun, primarily as an aid in understanding the Venus observations, but also because of the intrinsic interest in observing this seldomly studied planet.

Chapter 2. Data Reduction and Observational Results

2.1 Observing Strategy

The Very Large Array (VLA) [1], located on the plains of San Augustin, central New Mexico, stretches out in a 'Y' to cover some 40 kilometers of desert. The 27 twenty-five meter diameter transportable telescopes (9 telescopes on each arm of the array) capture the radiation flux originating in an observed patch of sky and transmit its characteristics back to a control building for cross correlation and other computer processing. Its design and construction is indicative of the sophistication of radio interferometry today, with respect to its instrumentation as well as its capability for processing the vast amounts of data that result from each observing program. All of the observational data presented in this thesis were obtained at the VLA.

In order to observe astronomical objects at the VLA, an "observe" file must first be created that specifies the position, wavelength, bandwidth (a total of 100 MHz for each of the observations presented in this thesis), start and stop time, proper motions, epoch, and gain code for every source observed. The array can be subdivided into sub-arrays, and each sub-array may be set to observe independently of the others, at any available wavelength.

The calibration strategy was to surround each planetary observation with short integrations on a known position calibrator. Position calibrators were selected from the VLA calibration manual. To provide a polarization and flux density fiducial, at least one observation was made of the source 3C286 during each observing session.

[1] The National Radio Astronomy Observatory is operated by Associated Universities, Inc., under contract with the National Science Foundation. Detailed descriptions of the VLA may be found in **An Introduction to the Very Large Array**, (National Radio Astronomy Observatory), and in **Synthesis Mapping; Proceedings of the NRAO-VLA Workshop Held at Socorro, New Mexico, June 21-25, 1983**, (Thompson and D'Addario, Eds.). An excellent description of radio interferometry may also be found in **Galactic and Extra-Galactic Radio Astronomy** (Fomalont and Wright, 1974).

The position of Venus on October 3, 1983 was determined by interpolation of the apparent positions given in the Astronomical Almanac (1983). The positions of Venus at five minute intervals on November 12,1983 were supplied by D. Mink (private communication, 1983). The positions of Mercury on April 4 and 5, 1985 were supplied by G. H. Kaplan (private communication, 1985).

Table 2-1 lists relevant information for the observations undertaken at the VLA. Four standard configurations of antennas along the 'arms' of the array are available, and are rotated on an approximately 15 month schedule. The 'A' configuration has the largest extent, while 'B', 'C', and 'D' are progressively more compact. In the A configuration, the shortest baseline is approximately 8/9 of the longest baseline of the D configuration. The scale factor between adjacent configurations is 3.285.

The A configuration was chosen for the Venus observations to take advantage of its high resolution. The hybrid A/B configuration for the Mercury observations was dictated by the schedule of the VLA in the context of Mercury's location *vis-a-vis* the sun.

During the observing runs the received radio frequency signals, converted to an intermediate frequency (IF) from four dual polarization channels (one left circular (A, B) and one right circular (C, D) polarization channel for each of two duplicate polarizations) for each antenna, were sampled, digitized, and cross-correlated (with the signals from each of the other antennas) or self-multiplied to obtain 8 cross-correlated outputs ($A_nA_m^*$, $C_nC_m^*$, $A_nC_m^*$, $C_nA_m^*$, $B_nB_m^*$, $D_nD_m^*$, $B_nD_m^*$, and $D_nB_m^*$ for each interferometer pair, where m and $n \neq m$ represent the antennas in the pair) and four auto-correlated outputs ($A_nA_n^*$, $B_nB_n^*$, $C_nC_n^*$, $D_nD_n^*$ from each antenna, n). Each cross-correlated result was divided by the geometric mean of the corresponding auto-correlated measurements of the two telescopes involved to produce the normalized visibilities (*i.e.* $A_nA_m / (A^2_n A^2_m)^{1/2}$, $C_nC_m / (C^2_n C^2_m)^{1/2}$, $A_nC_m / (A^2_n C^2_m)^{1/2}$, $C_nA_m / (C^2_n A^2_m)^{1/2}$, etc., where the squared terms stand for the auto-correlations) (Hjellming and Basart, 1982b). These visibilities were vector averaged over 10 second periods to form the complex visibilities

that comprise the results of the observations. The data was additionally compressed by averaging over 30 second intervals. The number of visibility data records (see Table 2-1) is the number of 30 second integrations of the planetary source that were obtained for each interferometer pair.

These measurements occurred over a range of projected spacings, due to the variety of physical separations between the telescopes, and due to the foreshortening of the apparent spacings during the rotation of the Earth. The uv range reflects the maximum and minimum distances between the origin and the visibility measurements in the Fourier transformed projected baseline plane (see section 2.3).

Table 2-1
Observational data

Source	Date	λcm	VLA Config.	(epoch 1950) RA of Planet	Dec of Planet	Hrs on Planet	*Visibility Records K	UV Range Kλ	Flux Jy 3C286	Position Calibrator	Flux Jy of Calibrator
Venus	10/03/83	20	A	$09^h56^m48.5^s$	08°31'33"	8.5	546	1 - 200	14.51	0952+179	1.070
Venus	11/12/83	20	A	$12^h11^m36.9^s$	00°01'26"	5.5	422	1 - 175	14.51	1148-001	2.71
Venus	11/12/83	6	A	$12^h11^m36.8^s$	00°01'27"	2.5	201	8 - 500	7.41	1148-001	1.930
Mercury	04/04/85	2	A/B	$00^h45^m16.2^s$	07°44'30"	4.5	330	5 - 200	3.44	0106+013	2.985
Mercury	04/05/85	6	A/B	$00^h42^m34.9^s$	07°13'48"	9.0	634	1 - 100	7.41	0106+013	4.35

* each visibility record is a 30 second observation by an interferometer pair

2.2 Data Calibration

The visibility data was calibrated by using the ensemble of software programs written specifically for this purpose that are available at the VLA (following the strategy outlined by Perley, 1985). First, listings of average flux values, and the associated rms's of the position calibrators (see section 2.1) were scanned for each antenna pair. Rms values that were unusual (much less or much greater than the noise) or average values that were much greater or much less than the expected flux of the position calibrator, invited careful inspection. If the data indicated a systematic deviation from the norm involving suspect antennas, or if the data showed signs of man-made interference, that data was flagged out and did not play a role in the subsequent calibration steps. Some of these judgements were made by the on-line computer system during the acquisition of the data, and were based upon some 300 parameters that measure the performance of each antenna (Hjellming, 1982).

The fluxes of the position calibrators were extrapolated from the assumed flux of 3C286, which was observed in every observing run. See Table 2-1 for the flux assumed for 3C286 during each observation, and the derived fluxes of the position calibrators. The flux of the position calibrator was then used to extrapolate the flux density of the planetary source.

The actual calibration of the planetary data was based upon the short, periodic observations of the amplitude and phase of the position calibrator. The VLA calibration software used iterative and non-linear least squares methods to solve for the complex 'gains' that transformed the 'raw' position calibrator visibility data such that the amplitudes were equal to the flux density of the position calibrator, and the visibility phases were close to zero. The complex gains were then applied to the planetary data, yielding a calibrated visibility database (Hjellming, 1982). The calibrated visibility data may also be corrected for position offsets, known time errors, Faraday rotation (λ = 20 cm only), etc. All corrections and calibrations were entered into gain tables (the raw visibility data were not

directly altered). The entries in the gain tables could then be applied to the data, while preserving the original, measured visibilities.

These corrected and calibrated data were used during the subsequent image construction. The image construction was facilitated by the Astronomical Image Processing System (AIPS). AIPS is described in detail in the 'AIPS cookbook', available from the VLA.

2.3 Image Construction

The source brightness distribution I(x,y) is the Fourier transform of the true, two-dimensional visibility function $V_{true}(u,v)$.

$$V(u,v) = \int dxdy\ I(x,y)\ e^{2\pi i(xu + yv]}$$

The observed visibility function is a product of the true visibility function and an error function E(u,v), a bandwidth loss function B(u,v), and a sampling function S(u,v). The flagging, calibration and corrections of the raw visibility data (discussed above) represent attempts to undo the effects of E(u,v) S(u,v) B(u,v) so that V_{obs} is as close to V_{true} as possible (Hjellming, 1982). The Fourier transform of V_{true} is evaluated by using a Fast Fourier Transform (FFT) algorithm. Since this method requires that the visibilities are known on a regular, rectangular grid (the sides given by a power of 2), the data is first 'gridded' by convolving the data with a function that defines the visibility function at the 'grid points'. Because of this discrete sampling, emission outside of the field of view will be reflected within the field of view (Fomalont and Wright, 1974). This 'aliasing' effect may be minimized by selecting a 'good' convolving function (Sramek, 1982). Tapering and weighting functions are also convolved with the visibility data to weight down the outer edge of the uv coverage, which will tend to suppress small scale sidelobes and increase the beam width; and to offset the concentration of uv data near the origin, which will tend to lessen the sidelobes caused by gaps in the uv data (Sramek, 1982). Following gridding, the convolved visibility function is Fourier transformed *via* the FFT, resulting in an image that is called the 'dirty map'. Because of the finite sampling of the noisy data, the dirty map is not a complete representation of the source brightness distribution (Cornwell, 1982) , and is resplendent with sidelobes (which, of course, may be masked by noise if the signal is weak). The synthesized beam may be generated by setting each value of V(u,v)

for which a baseline exists to 1, and taking a Fourier transform of this result. In this way we create a dirty map of a unit point source, also known as the point spread function.

Maps of the Stokes parameters I,Q,U, and V were made for each database. The physical interpretation of these parameters is as follows (Kraus, 1966) :

1. I is the total intensity of the received radiation.
2. Q is the in-phase difference in linearly polarized intensity 90° apart in position angle.
3. U is the in-phase difference in linearly polarized intensity 90° apart in position angle in a frame rotated 45° from components used to determine Q.
4. V is the difference in left and right circulary polarized intensities.

Unlike most VLA images, the Stokes I maps of the planetary disks were characterized by a plateau of emissions with well defined circular edges. The CLEAN deconvolution algorithm (Clark, 1980), devised originally for point sources, was found to be inefficient for these sources because of the enormous number of CLEAN components that were required. On the other hand the maximum entropy method (AIPS task VM, see Cornwell and Evans, 1985) was found to be ideal for this type of source structure. The Q and U maps, on the other hand, required the use of CLEAN, to preserve the negative map components that VM would eliminate as unreal. (See section 2.5).

As expected, the Stokes parameter V had no signal above the noise in any map. The total intensity Stokes I map was deconvolved *via* the maximum entropy method (see above). Due to the uneven resolution that VM produces, the maps were convolved with gaussians corresponding in width to the synthesized beams. The AIPS task CONV also multiplies the data by a unit conversion factor, F, so that the resultant data is in units of Jy /pixel.

The Q and U maps were CLEANed , and then combined to produce polarization intensity maps. The polarization intensity (PI) is just $\sqrt{Q^2+U^2}$ (Kraus, 1966), and was obtained by applying the AIPS task COMB (see the AIPS cookbook). The PI maps were

convolved with gaussians corresponding in width to the synthesized beams, in order to maintain uniformity with the Stokes I maps. The angle of the linear polarization (PA) may be obtained similarly by COMB *via* 1/2 $\tan^{-1}$ (U/Q) (Kraus, 1966). The degree of polarization was obtained by using COMB to divide the polarization intensity map by the total intensity map. Total intensity map minimums were set to minimize the effects of division by values close to zero. Naturally, the degree of polarization values have meaning only over the disk of the planet .

Because of the lack of data at short projected spacings, and the large angular extent of the disk (greater than 40 resolution elements in diameter), the sidelobes of the λ = 6 cm Venus dirty map were not adequately removed during the VM deconvolution process. A model of a disk with a flux of 5 Jy was,therefore, used to supply the missing uv components to the visibility data in an effort to stabiize the low spatial frequency structure, as follows:

Data at a wavelength of 20cm were obtained at projected spacings as small as 1000 wavelengths on November 12, 1983, while for the same date, at λ = 6 cm, the minimum projected spacing was 8000 wavelengths. In order to compensate for the lack of data at short projected spacings at λ = 6 cm, the following procedure was followed:

1. A subset of the data (projected spacings less than 7000 wavelengths) of the data at λ = 20 cm, was initialized and copied to a temporary file.
2. A model of a disk (flux = 5 Jy) was created *via* the AIPS task UVMOD and inserted into the temporary database.
3. The temporary database was combined with the λ = 6 cm data.

The visibility data were then mapped, deconvolved by VM, and convolved with a gaussian corresponding to the resolution.The sidelobes of the resultant image were much lower than those resulting from use of the original data alone (see Figure 2-15).

2.4 Results of Observations

See Table 2-2 for a list of the physical characteristics and orientations of the planets on the dates of observations. Mercury reached inferior conjunction on April 3, 1985, while Venus reached inferior conjunction on August 25, 1983, and greatest enlongation on November 4, 1983. Venus, on October 3, 1983, was illuminated only over a third of its visible surface, while on November 12, 1983, over half the disk was illuminated. Both Mercury observations took place when virtually the entire disk of the planet was in shadow.

Planetocentric coordinates of Venus and Mercury on the dates of the observations were obtained by the method described in the Astronomical Almanac (1983, 1985) , and by Davies *et al* (1980). The location of surface features on Mercury were drawn from Wood and Head (1976), while for Venus they were drawn from Pettengill *et al* (1980). See Figures 2-8, 2-12, and 2-20.

During the October 3, 1983 observations, an artifact appeared at the center of the image, due to an intermittent fault in the acquisition of the data (since corrected) (Crane, 1984). This artifact manifested itself as a few pixels of substantially reduced brightness at the very center of the disk of the planet.

Table 2-2
Observational planetary characteristics

Source	Date	Distance A.U.	Ang. Radius arcsec	Sub Earth Lat. degrees	Sub Earth Long. degrees	Phase
Venus	10/03/83	0.4546	18."6	+5.°2	16°	0.289
Venus	11/12/83	0.7490	11."3	+0.°6	110°	0.543
Mercury	04/04/85	0.5890	5."7	-6.°6	207°	0.005
Mercury	04/05/85	0.5862	5."7	-6.°5	213°	0.005

Radius assumed in calculating β : Venus r = 6120 km; Mercury r = 2439 km

2.4.1Visibility Measurements - General Comments

Figure 2-1 shows a plot of the typical uv coverage obtained during the observations of the planets Venus and Mercury. The uv coverage shows how completely an aperture has been synthesized, and is simply the location of the data in the (spatial) Fourier space. Each point represents an observation of the visibility function at that uv coordinate. A sample of the approximately 500,000 visibility measurements of Venus obtained on October 3, 1983 is plotted. Each visibility measurement represents a 30 second observation by an interferometer pair.

Inspection of the data (see below) shows the agreement of the data with that expected for a uniformly bright disk. The visibility function for a disk is:

$$V(u,v) = \iint_{disk} S\cos(\beta)dydz = S\, J_1(2\pi\beta)/(\pi\beta) \qquad (2.3)$$

where J_1 is the Bessel function of first order and first kind with $\beta = yR/\lambda D$, the parameter y is the interferometer spacing, λ is the wavelength, R is the radius of the planet, D is the distance to the planet, and S is a constant that may be associated with the zero spacing flux density for the planet (Pollack and Sagan, 1965).

Table 2-3 lists the location of the nulls of the observed visibility function for each planetary database. In order to allow direct comparison with Muhleman, Orton, and Berge (1979), the radius for Venus used in obtaining β was chosen as 6120 kilometers, and includes the effects of refraction by the atmosphere (the physical radius of Venus is 6050 km. The value of 6120 km was chosen to facilitate comparisons with previous results). Tabulated for comparison are the location of the visibility nulls found by Muhleman, Orton, and Berge (1972) (MOB) and the location of the visibility nulls predicted by equation 2.3 for a perfect disk. The radius for Mercury used in obtaining β was chosen as 2439 km (Astronomical Almanac, 1985). See appendix A4 for calculations of v(u,v) for various values of S as a function of β. These curves may be compared directly with the data to

extrapolate the zero spacing flux of the emissions. A comparison of the location of the visibility nulls of Figures A-3, A-4 and A-5 with the location of the visibility nulls listed in Table 2-3 confirms that the visibilities of Venus and Mercury correspond quite closely to that of a disk.

Figures 2-2 to 2-6 are plots of the measured visibility functions *versus* interferometer spacing in wavelengths (i.e. $\sqrt{u^2 + v^2}$) for each of the planetary observations. As Figure 2-1 implies, however, this data was obtained at a wide variety of azimuths. In general, about one tenth of the visibility measurements were plotted. In addition, for clarity, only visibility data for projected spacings corresponding to the first few nulls were plotted.

The errors following the measured zero spacing fluxes (see sections 2.4.1.1 and 2.4.1.2) were obtained by estimating the measurement uncertainties when comparing the visibility functions with the theoretical curves for a disk (Figures A-3, A-4, and A-5). The brightness temperatures were obtained by the method of appendix A1.

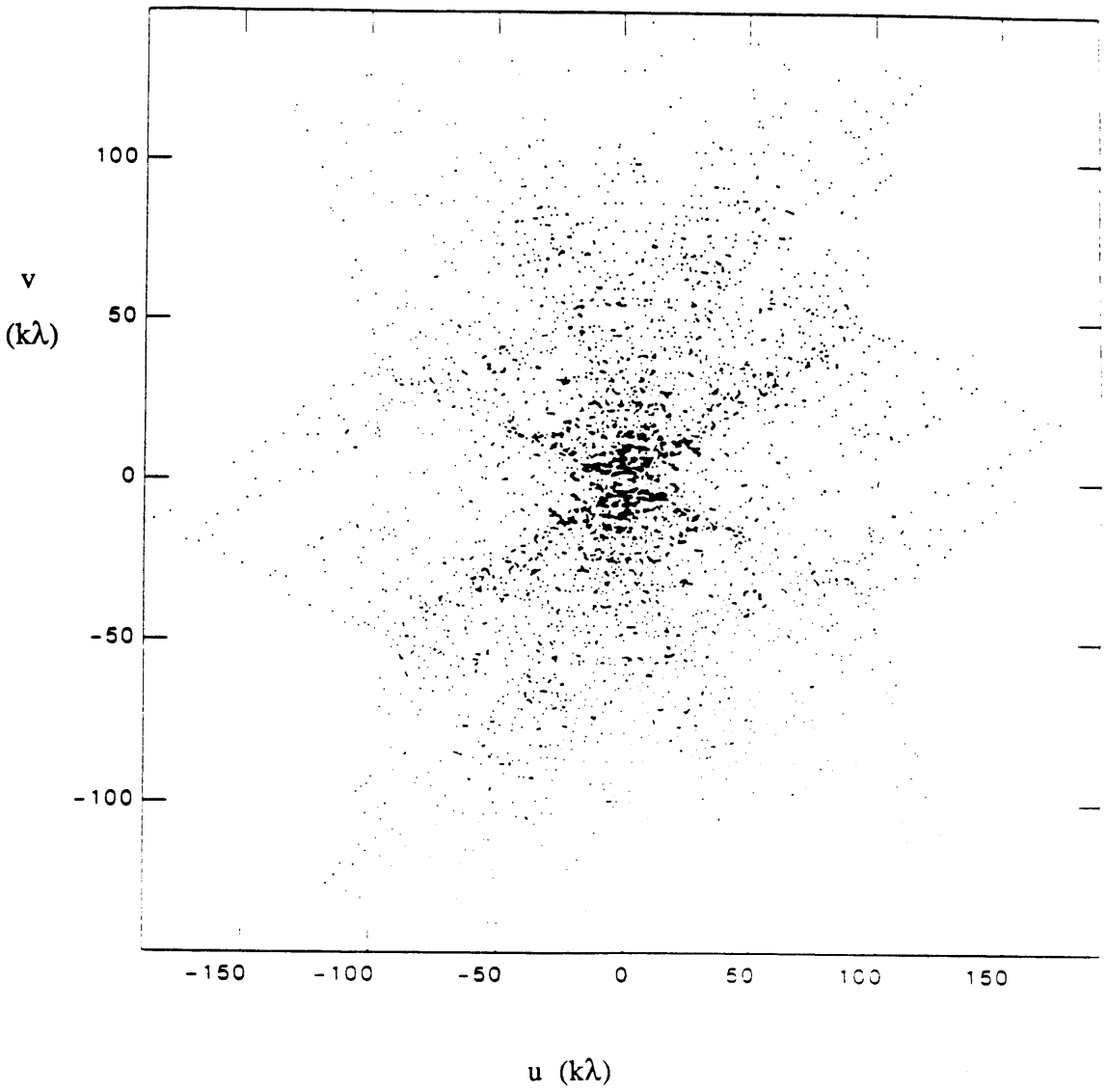


Figure 2-1
The typical location in the uv plane of the visibility measurements. Points plotted are for the October 3, 1983 dataset.

Table 2-3

β's corresponding to observed visibility nulls

Source	Date	Wavelength	Null	β (circular disk)	β (VLA data)	β (MOB *)
Venus	10/3/83	20	1st	0.61	0.63 ± 0.01	0.6204 ± 0.0025
Venus	10/3/83	20	2nd	1.11	1.13 ± 0.01	
Venus	10/3/83	20	3rd	1.62	1.79 ± 0.01	
Venus	11/12/83	20	1st	0.61	0.60 ± 0.01	0.6204 ± 0.0025
Venus	11/12/83	6	1st	0.61	0.609 ± 0.005	0.6179 ± 0.0009
Venus	11/12/83	6	2nd	1.11	1.06 ± 0.02	1.1267 ± 0.0009
Venus	11/12/83	6	3rd	1.62	1.64 ± 0.02	1.635 ± 0.003
Venus	11/12/83	6	4th	2.12	2.13 ± 0.02	2.14 ± 0.004
Venus	11/12/83	6	5th	2.62	2.64 ± 0.02	
Mercury	4/4/85	2	1st	0.61	0.65 ± 0.01	
Mercury	4/4/85	2	2nd	1.11	1.14 ± 0.01	
Mercury	4/4/85	2	3rd	1.62	1.63 ± 0.01	
Mercury	4/4/85	2	4th	2.12	2.15 ± 0.01	
Mercury	4/5/85	6	1st	0.61	0.644 ± 0.003	
Mercury	4/5/85	6	2nd	1.11	1.113 ± 0.003	

Assumed radius : Venus r = 6120 km; Mercury r = 2439 km

* MOB : Muhleman, Orton, and Berge, 1979.

2.4.1.1 Visibility Measurements - Venus Data

Figure 2-2 shows that portion of the data obtained on October 3, 1983 at a wavelength of 20 cm with projected uv spacings of less than 50,000 wavelengths. The zero spacing flux is 1.1 ± 0.05 Jy, which corresponds to a disk averaged brightness temperature of 623° ± 28° K (See appendix A1). Figure 2-3 is a plot of the visibility data *versus* interferometer spacing obtained on November 12, 1983 at λ = 20 cm. The zero spacing flux for this date is 0.4 ± 0.03 Jy (see Table 2-2 and note the smaller angular size of the disk on this date as compared to the October 3 data,) which corresponds to a brightness temperature of 615° ± 45° K. Observations by Berge, Muhleman, and Orton (1972) measured the disk averaged brightness temperature of Venus to be 617° ± 25° K at λ = 21.1 cm. However, their determination was made for planetary apparitions not corresponding to the measurements made here. See Table 2-2 for the sub-Earth longitude of the orientations observed on October 3 and November 12, 1983.

Figure 2-4 is a plot of the visibility of Venus obtained at a wavelength of 6 cm on November 12, 1983. The flux is greater for this data compared with the λ = 20 cm data because of the greater flux of Venus at λ = 6 cm primarily as a result of the λ^{-2} factor in the Rayleigh-Jeans law; see appendix A1). To stabilize the low spatial frequency behavior of the observations, a model of a disk (total flux of 5 Jy) was added to the data for projected spacings of 0 to 7000 wavelengths, as discussed previously. The disk-averaged flux of Venus as indicated by the data is 4.6 ± 0.1 Jy and corresponds to a brightness temperature of 636° ± 15° K. Previous observations by Berge, Muhleman, and Orton (1972) at λ = 6 cm indicated an average brightness temperature of 655° ± 30° K.

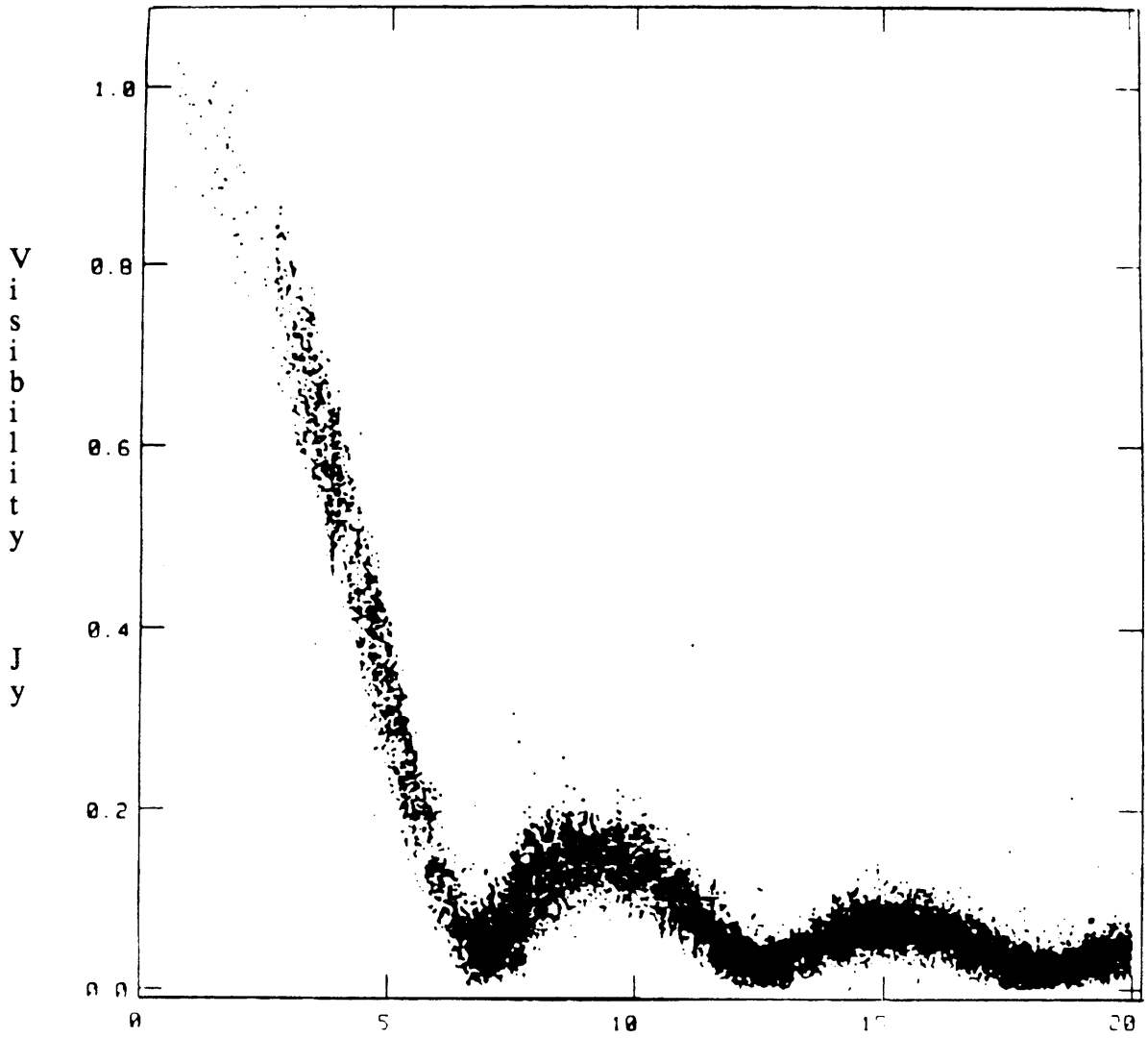


Figure 2-2
Visibility data (in Jy) versus the projected spacing y/λ, where y is the projected spacing and λ is the wavelength, for the data obtained October 3, 1983 at λ = 20 cm of Venus.

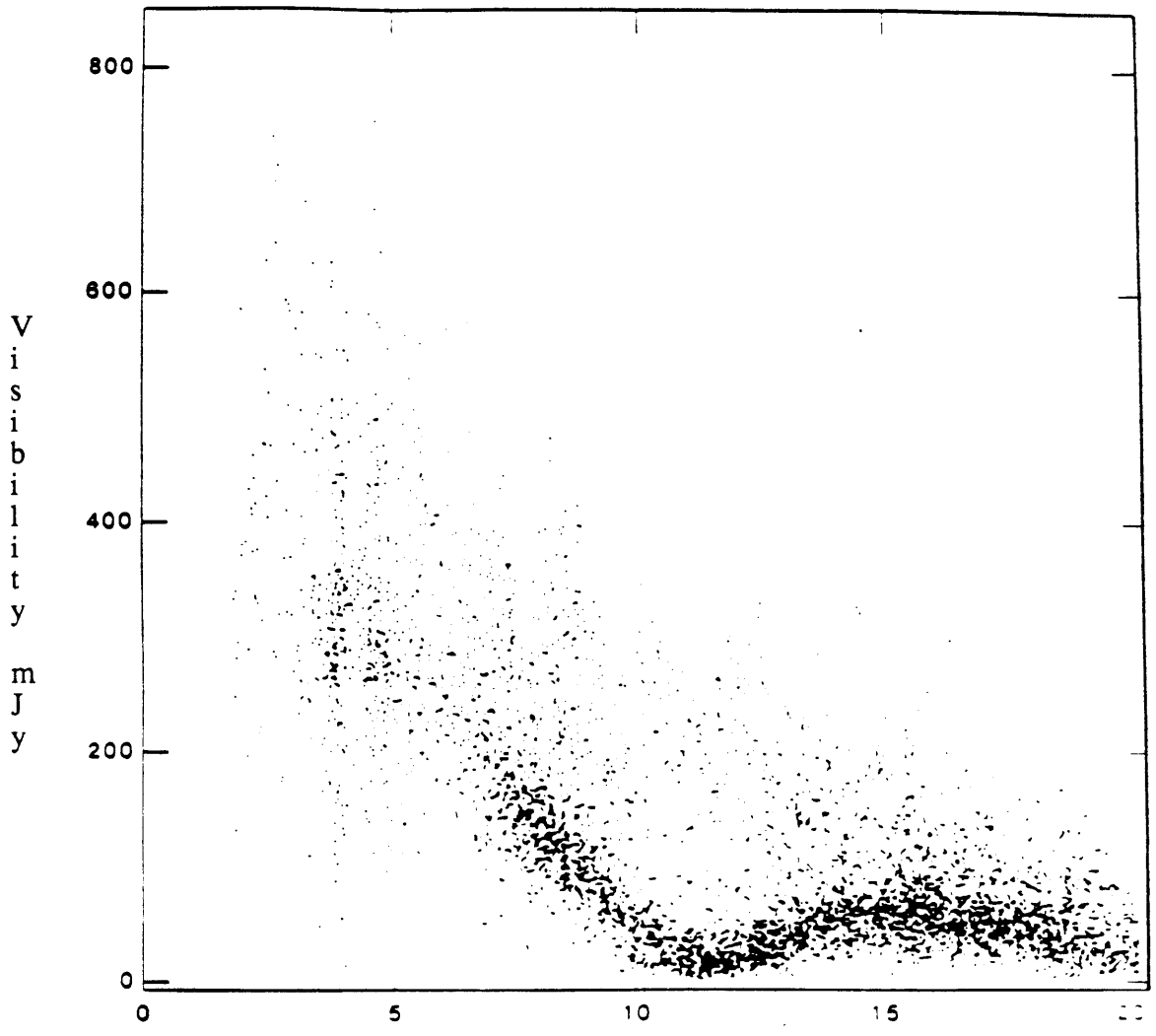


Figure 2-3
November 12, 1983 λ = 20 cm Venus visibility data

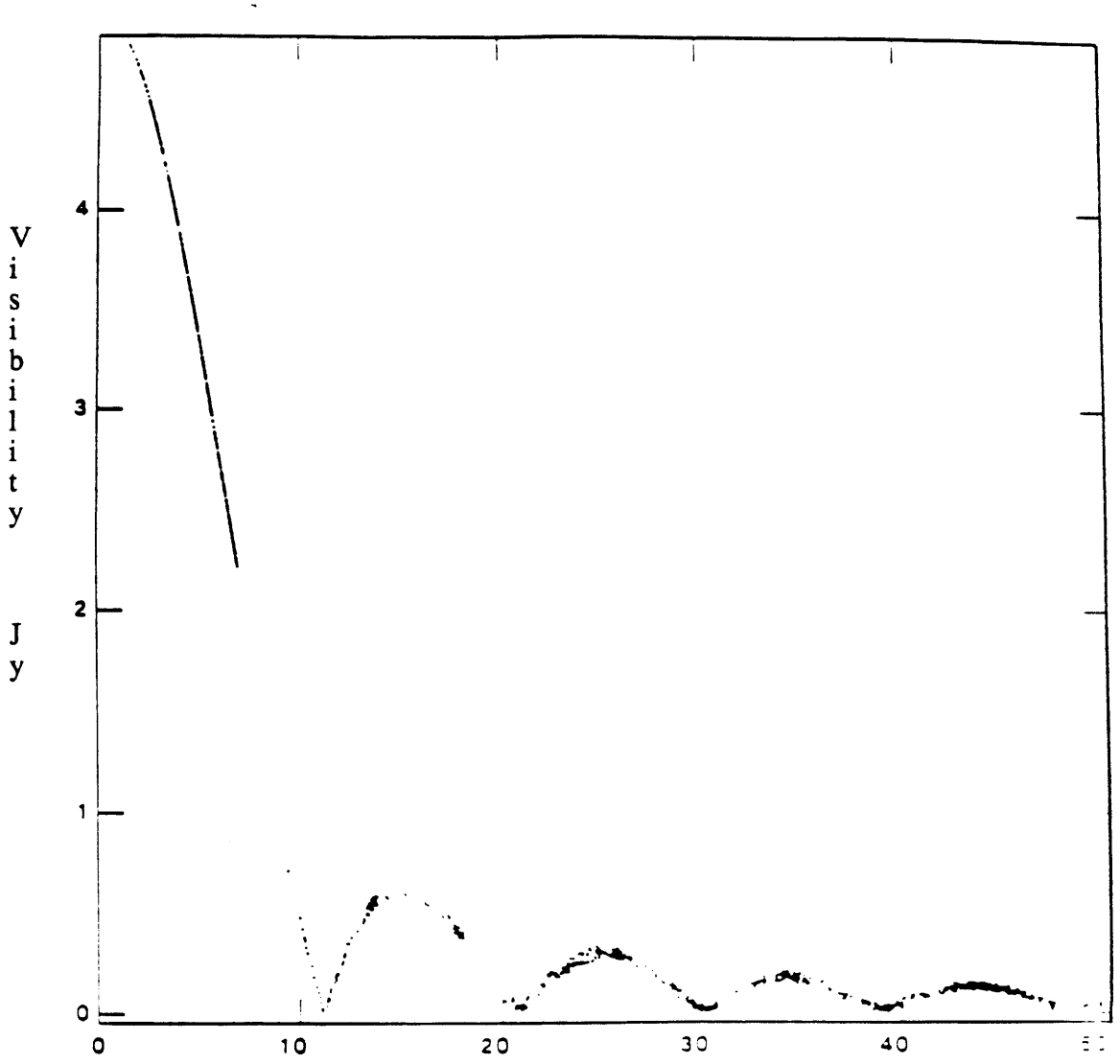
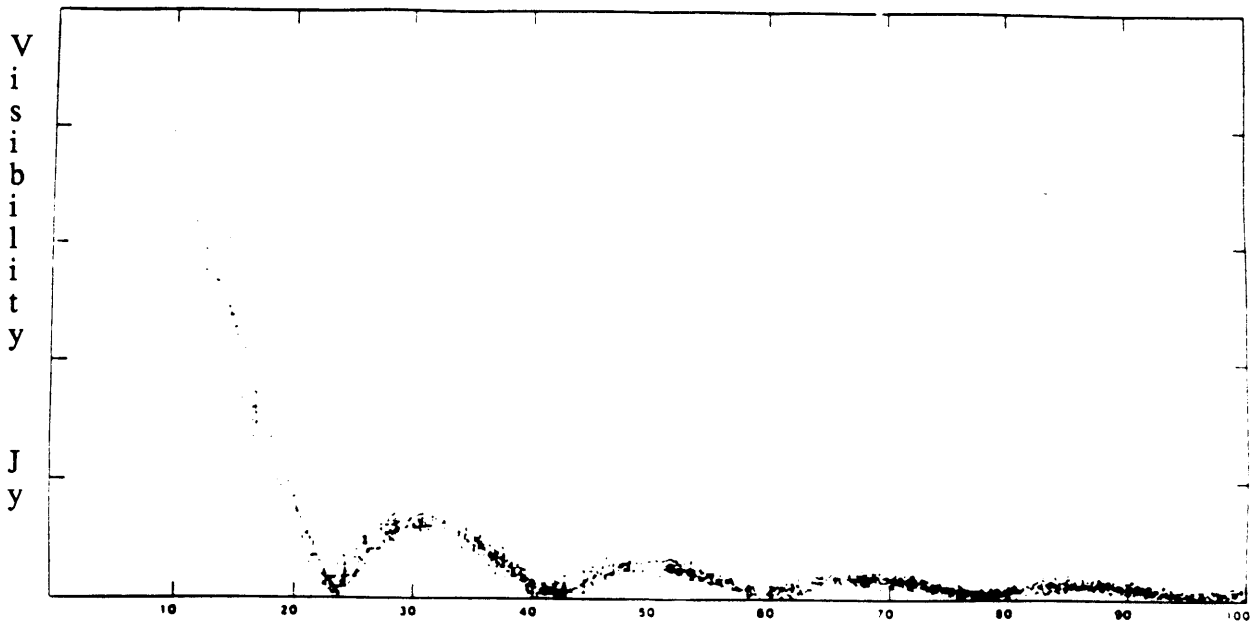


Figure 2-4
November 12, 1983 λ = 6 cm Venus visibility data (model added to data between y/λ=0 and 7000 wavelengths.

2.4.1.2 Visibility Measurements - Mercury Data

Figures 2-5 and 2-6 are plots of the visibility data *versus* projected spacing obtained for the planet Mercury. Mercury was within 2 degrees of the sun on April 4 and April 5, 1985. At λ = 2 cm very little interference was noted. At λ = 6 cm, where the primary antenna beam size is larger (9' *versus* 4'), some data were adversely affected by solar interference through the sidelobes of the antenna pattern. Anomalously large fluxes were eliminated, as well as data that systematically differed from the majority. Overall, only a small fraction (about one in one thousand) of the visibility measurements were eventually flagged as bad. We feel that the likelihood that bad data still exist in the database is no greater than for any of the other observational databases presented here.

The zero spacing flux of the April 4, 1985 λ = 2 cm data is 5.3 $\pm$ 0.1 Jy corresponding to a disk-averaged brightness temperature of 320° $\pm$ 6° K. For April 5, 1985, the data indicates an unresolved flux of 0.62 $\pm$ 0.03 Jy, implying a corresponding brightness temperature of 337° $\pm$ 16°K.



Interferometer Spacing

(K λ)

Figure 2-5
April 4, 1985 λ = 2 cm Mercury visibility data.

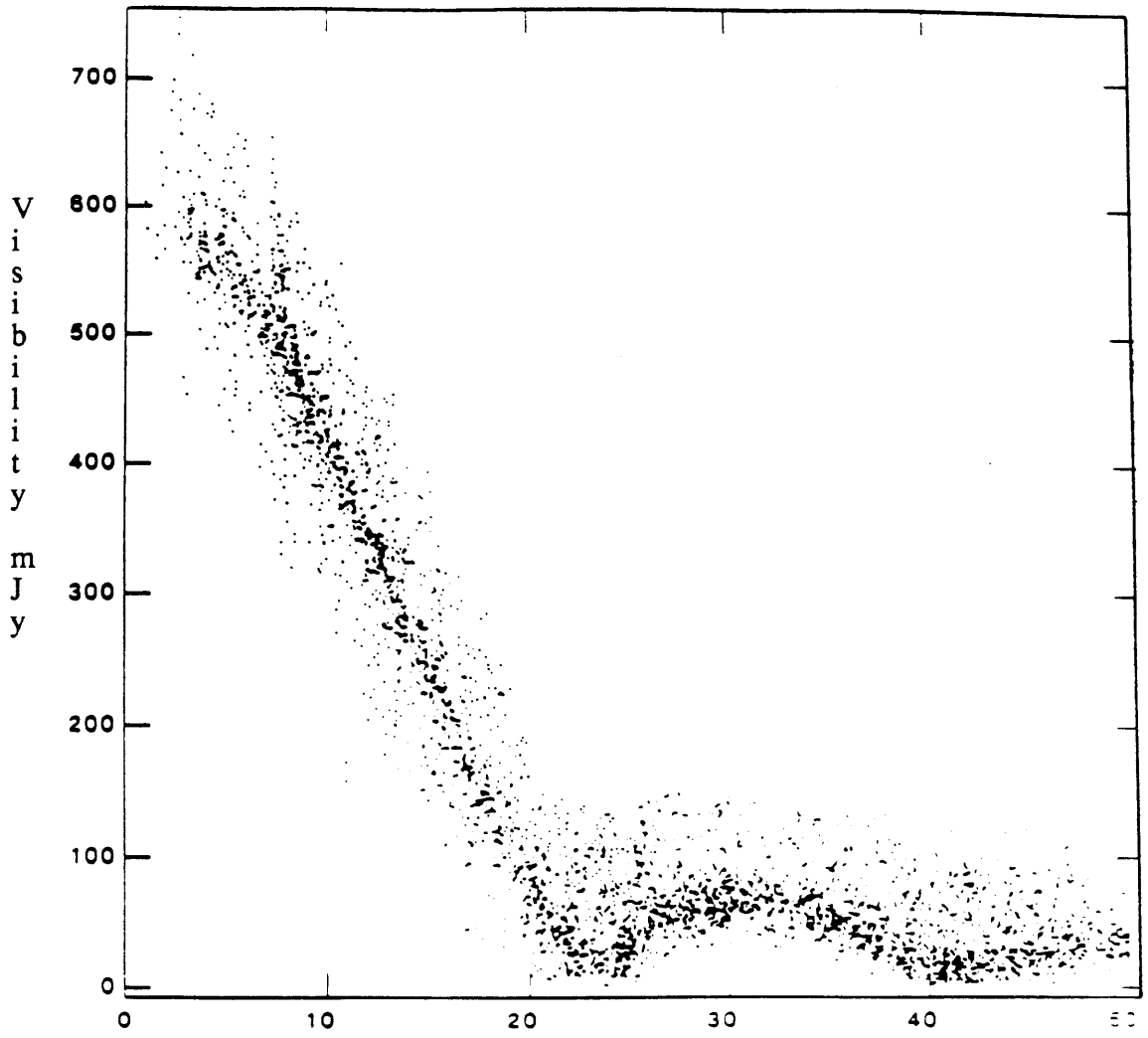


Figure 2-6
April 5, 1985 λ = 6 cm Mercury visibility data.

2.4.2 Stokes I maps - General Comments

See Appendix A1 for a brief discussion of the Rayleigh-Jeans approximation to Planck's law, and the method used for obtaining the brigntness temperature from the source flux. Table 2-4 lists the results of these calculations for each observation. F is the convolution factor; pix size is the size of the image pixels (in arcseconds); the resolution is the half power beam width of the synthesized beam (in arcseconds; and, for the given distance of the planet, the linear resolution at the center of the disk in kilometers); S is the average flux density; and T_B is the brightness temperature. T_B(avg) is the average brightness temperature found by averaging the map pixel values, while T_B(zero-spacing) is the T_B extrapolated to the projected spacing of zero from the visibility data. Measurement uncertainties and errors are primarily responsible for the difference in the T_B's, which generally agree within the margin of error.

Refer to Table 2-5 for typical noise variations found in the maps. The rms noise was determined from those pixels in the VM images that lay outside of the disk of the planets, by summing the squares of the pixel values, dividing by the number of pixels, and taking the square root. The theoretical time-bandwidth noise expected for a point source observation for each synthesis (100 MHz bandwidth), weighting each correlator measurement the same (see Napier and Crane, 1982) are tabulated along with the rms noise values of the maps.

The contour intervals for each map (Figures 2-7, 2-11, 2-15, 2-19, and 2-23) are indicated at the bottom of each page. To help distinguish local minima and maxima, a grey scale has been added. Darker greys are associated with higher brightness temperatures.

Table 2-4

Summary of results of observations

Observation	λ cm	F	Pix Size arcsec	Resolution arcsec	Resolution km (center)	S(avg) mJy/pix	T_B(avg) K	T_B(zero spacing) K
VENUS : 10/03/83	20	18.1296	0."25	1."00	330	1.17 ± 0.029	636 ± 16	623 ± 28
VENUS : 11/12/83	20	15.2339	0."30	1."10	600	1.33 ± 0.098	600 ± 44	615 ± 45
VENUS : 11/12/83	6	6.1691	0."15	0."35	190	1.64 ± 0.038*	653 ± 15*	635 ± 15
MERCURY : 4/4/85	2	7.0819	0."10	0."25	110	3.50 ± 0.278	305 ± 24	320 ± 6
MERCURY : 4/5/85	6	12.5900	0."15	0."50	210	1.64 ± 0.051	320 ± 10	337 ± 16

$T_B = \lambda^2_{cm}\ (10^{-4})\ S_{Jy}(10^{-26})\ 4.2545x10^{10}\ ("^2/str)/[F\ \theta^2_{pix"}\ 2(1.38x10^{-23}J/K)]$

$T_B = 1540.8\ \lambda^2_{cm}\ S_{Jy} / [F\ \theta^2_{pix"}\ ]$

* These results have been reduced by 8%. See Appendix A3 for a discussion.

Table 2-5
Noise level of maps

Source	Date	Wavelength cm	Total flux Jy	RMS Noise mJy	K	Time-bandwidth noise mJy[1]
Venus	10/03/83	20	1.1	0.029	16	0.0126
Venus	11/12/83	20	0.4	0.098	44	0.0129
Venus	11/12/83	6	4.6	0.038*	15*	0.0155
Mercury	04/04/85	2	5.3	0.278	24	0.0866
Mercury	04/05/85	6	0.62	0.051	10	0.0081

* These results have been reduced by 8%. See Appendix A3 for a discussion.

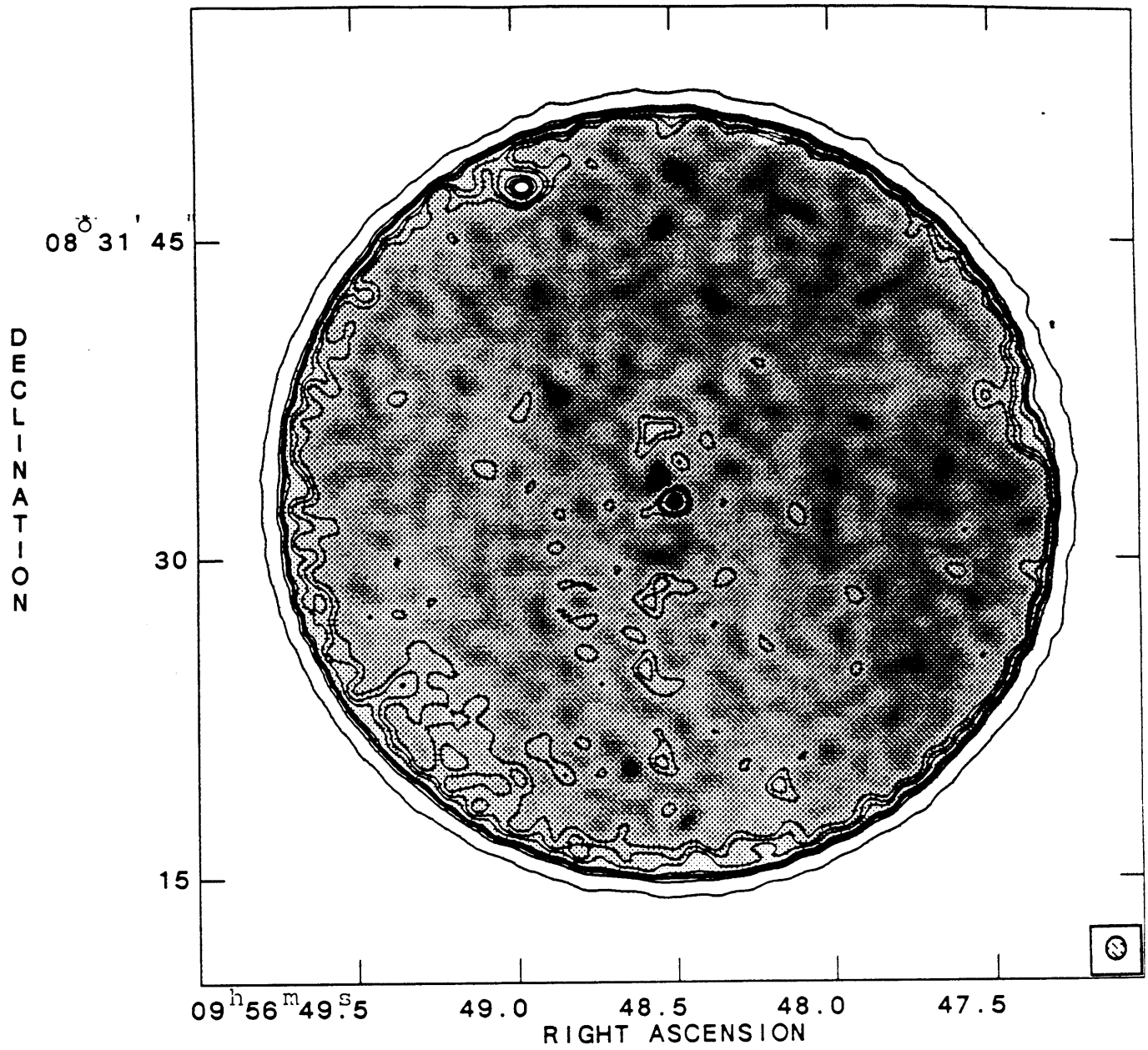
[1] from Napier and Crane (1982)

2.4.2.1 Stokes I Maps - Venus Data

The deconvolved image of Venus at a wavelength of 20 cm, made on October 3, 1983, is shown in Figure 2-7. Figure 2-8 shows the relationship of Figure 2-9 to the surface features and planetocentric coordinates. The unilluminated portion of the planet is indicated by grey shading.

A comparison of Figure 2-7 with Figure 2-8 reveals that the low brightness area in the northern hemisphere coincides with the location of Maxwell Montes (Pettengill et al, 1980). At 90° longitude, we see a low brightness feature associated with the location of Aphrodite Terra, remarkable for its visibility even at the limb, and a tribute to the transparency of the Venus atmosphere at λ = 20 cm. At the center of the disk, an artifact caused by rounding errors during the acquisition of the data (Crane, 1984) is present. We indentify this as a negative artifact due to its location precisely at the center of the map, and to the lack of surface features corresponding to that location. Associated with this negative artifact is an adjacent positive one.

Figure 2-9 is a histogram plot of the map values in Figure 2-7. Each bin is 10°K wide. This plot indicates the symmetry of the data, and the magnitude of the noise. The number of pixels is relative, in that the size of the image versus the size of the disk will determine the absolute relationship between the number of noise pixels and the number of planet pixels. Figure 2-10 is a plot of every pixel T_B value of the Figure 2-7 image, plotted as a function of the azimuth angle measured from the center of the disk, counterclockwise starting from South. At 105 degrees azimuth, we see Aphrodite, located on the limb of the planet, dropping down to 450 K. At 205 degrees azimuth, Maxwell reaches brightness temperatures as low as 405 K. A few scattered low T_B's (and high T_B's) are due to the artifact at the center of the image. Recall that Pioneer Venus atmospheric probes found that the atmospheric temperature at an altitude of 11 km (which is the maximum altitude of Maxwell from the mean) was only 80 K cooler than at mean altitude (Seiff et al, 1980), while here we see brightness temperatures as much as 250° K cooler than the mean. See



S(Jy x 10^{-4})	2	7	8	8.25	8.5	9	10	10.5	11	13	Peak = 1.44 mJy
T_B (K)	109	381	435	449	462	490	544	571	598	707	Peak = 784 K

Figure 2-7

Contour-grey scale plot of Venus - October 3, 1983 λ = 20 cm. Note cool temperatures associated with Maxwell Montes (11 o'clock near limb) and Aphrodite Regio (2:30 o'clock at limb). The central "hole" is an artifact.

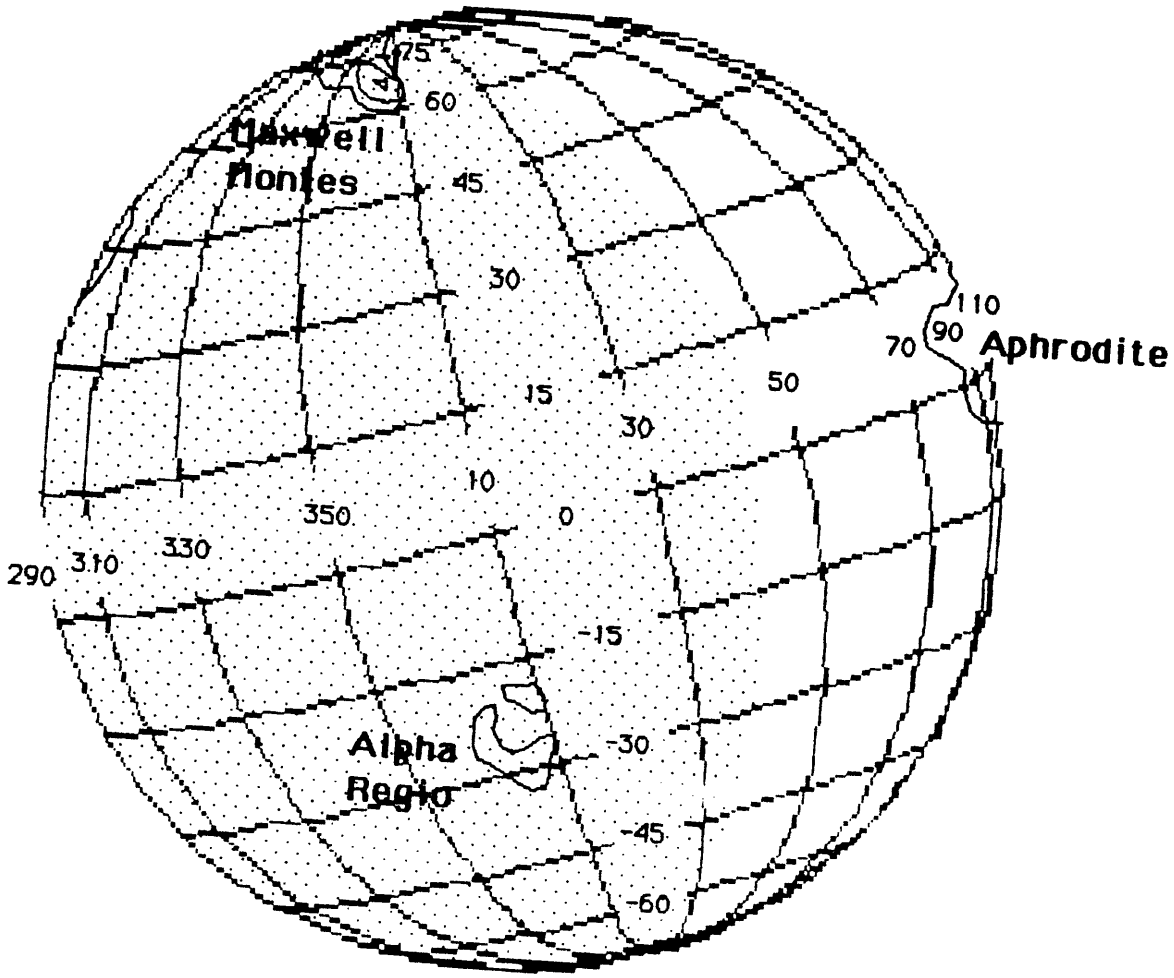


Figure 2-8
Planetocentric coordinates corresponding to Figure 2-7. Stippled area is not illuminated by the sun.

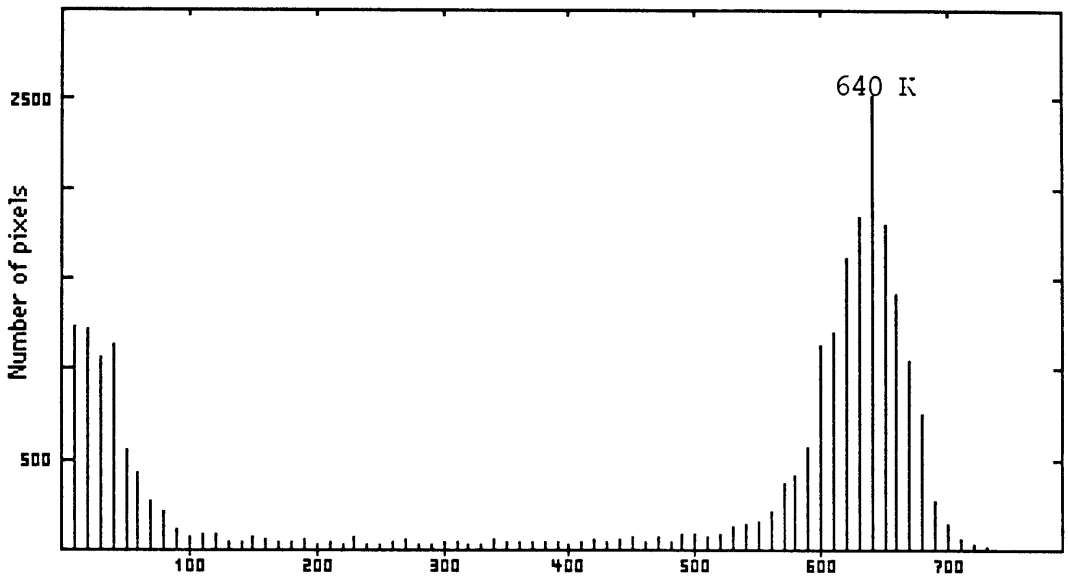


Figure 2-9
Histogram of T_B for Figure 2-7.
Venus - October 3, 1983 at λ = 20 cm

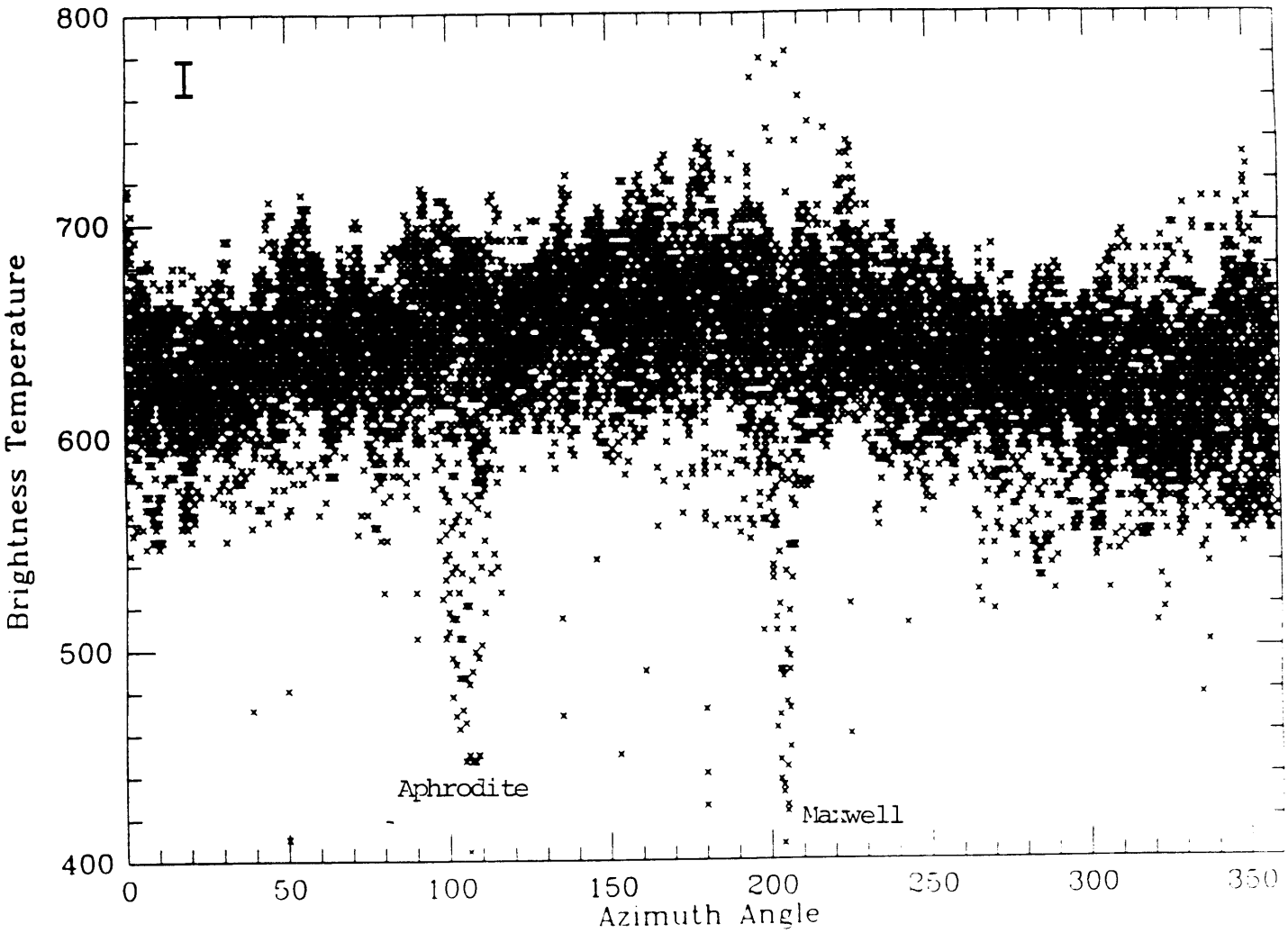
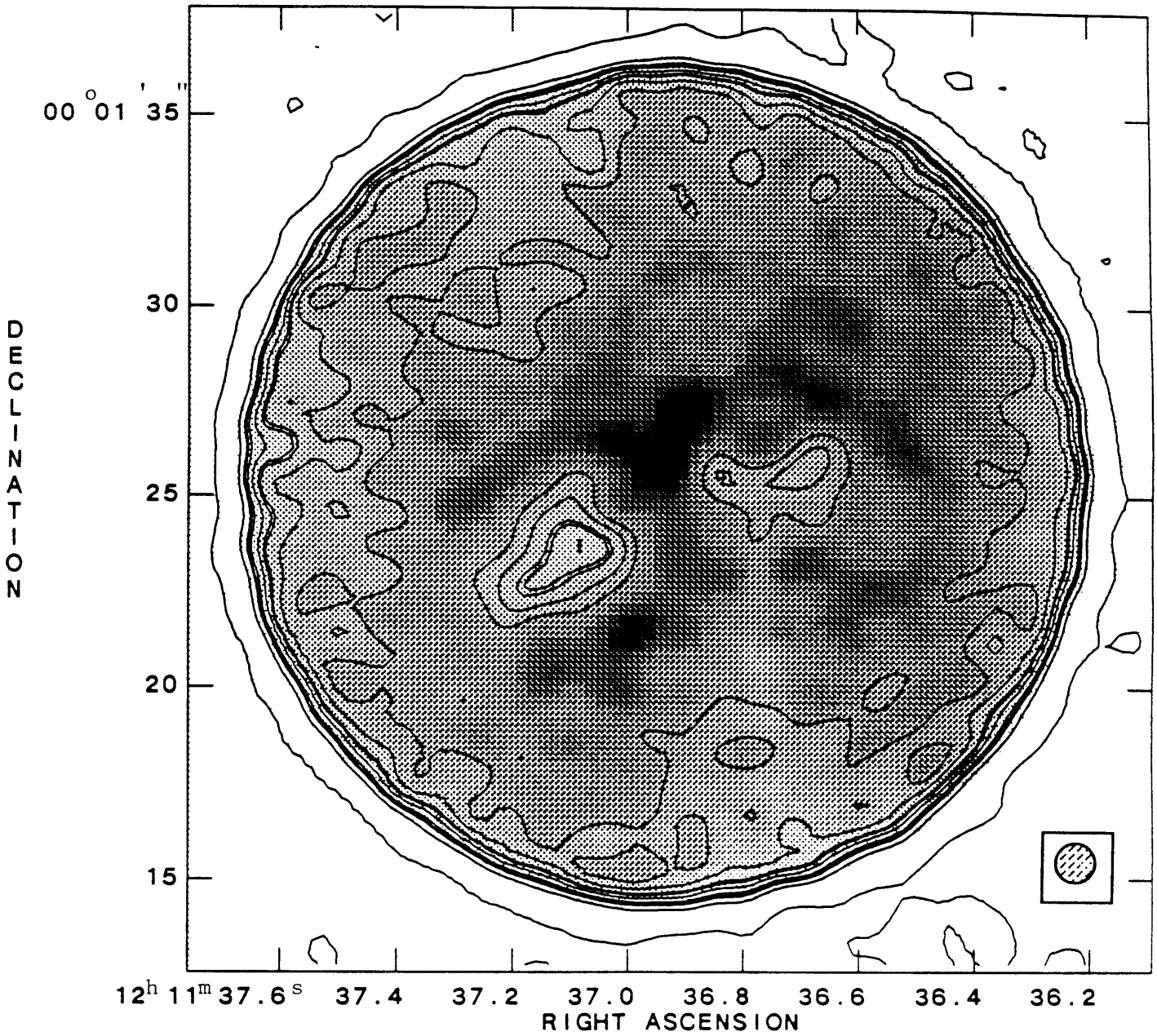


Figure 2-10
Brightness temperature of each pixel of Figure 2-7 versus azimuth angle counterclockwise from South.

section 4.1.1 for a discussion of the probable reasons for this effect. In section 2.3, we noted that the image from which these points were extracted was convolved with a gaussian of 1 arcsecond full width half maximum. As can be seen, the average brightness temperature is approximately 40° ± 10° K higher towards the Northeast, on the celestial sphere, than towards the Southwest. This is in agreement with the illumination of Venus on that date, although how the illumination could induce such a variation in brightness temperature is not obvious. Previous measurements indicated a smaller T_B dependence (18° K) on illumination (Goldstein, 1972).

The November 12, 1983 deconvolved image of Venus (λ = 20 cm) is shown in Figure 2-11. As can be seen by Figure 2-12, this orientation of Venus is dominated by Aphrodite Terra. The angular radius of Venus is smaller on this date, reducing the surface resolution as compared to the October 12, 1983 data. Figure 2-13, again, is a histogram plot of the brightness temperature values with a bin width of 10°K. Figure 2-14 is a plot of every pixel value versus azimuth from the data of Figure 2-11. Pixels at azimuths of 90 and 300 degrees where Thetis and Ovda Aphrodite are located, indicate brightness temperatures as low as 515 K near Thetis, and 450 K for Ovda. This plot is too complex to ascertain whether a systematic (diurnal) temperature variation is in evidence. However, Figure 2-11 does show that the limb of the unilluminated portion of the planet falls off more gradually than in the case of the illuminated hemisphere. Slightly to the North of Aphrodite, a region of high brightness temperatures adjacent to Ovda and Thetis reaches values as high as 772 K. Approximately 25 pixels exceed 735 K. These high T_B's may indicate either higher than average physical temperatures and/or emissivities (see section 4.3.1), or 'sidelobe' structure arising from the reduced brightness of Aphrodite.



S(Jy x 10^{-4})	2	7	8.25	8.5	9	10	10.75	11	12	13	Peak 1.7164 mJy
T_B(K)	90	315	371	382	405	450	483	494	539	584	Peak 772 K

Figure 2-11
Contour-grey scale plot of Venus - November 12, 1983 λ = 20 cm. Note the two cool regions associated with Aphrodite Regio near center.

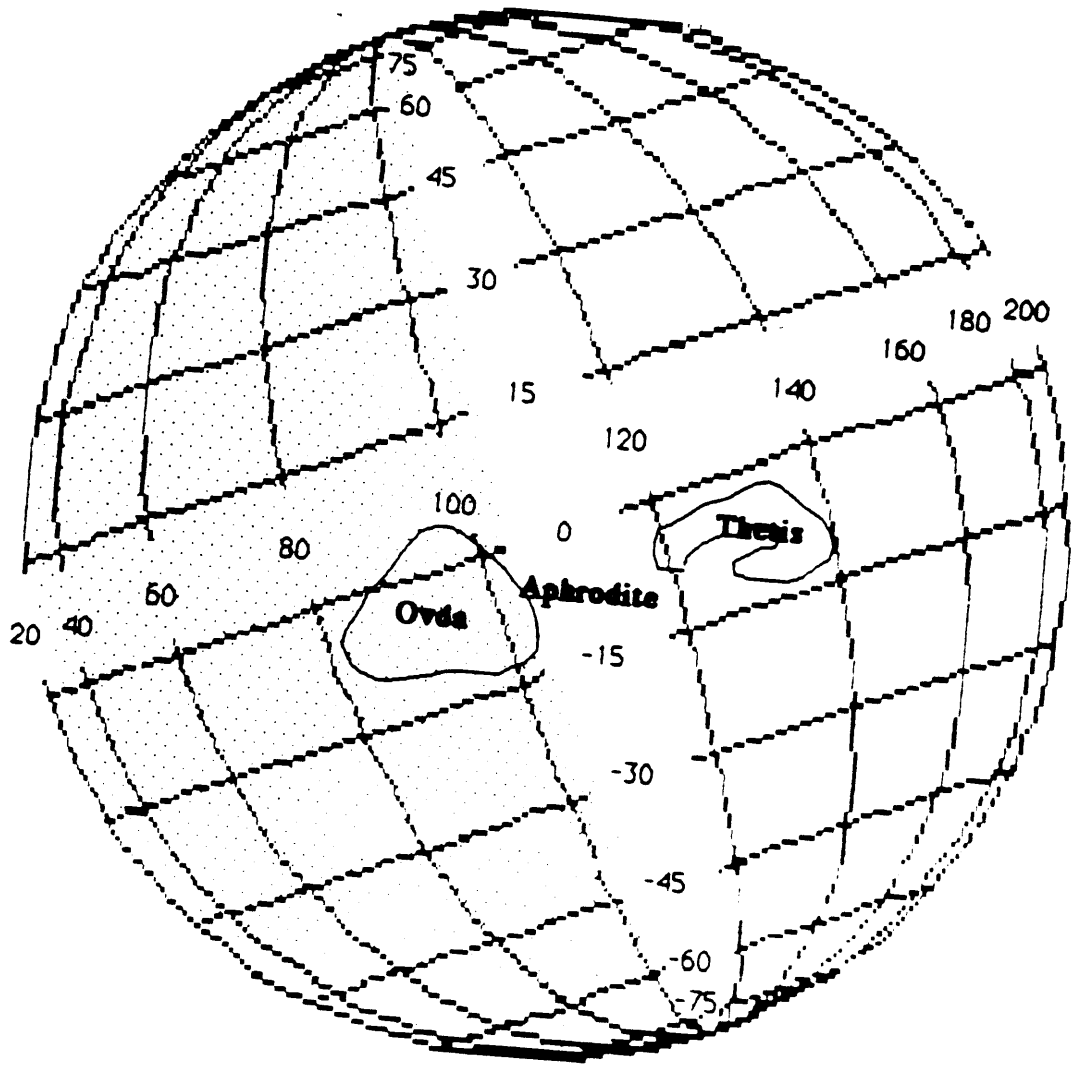


Figure 2-12
Planetocentric coordinates corresponding to Figure 2-11 and 2-15. Stippled area is not illuminated by the sun.

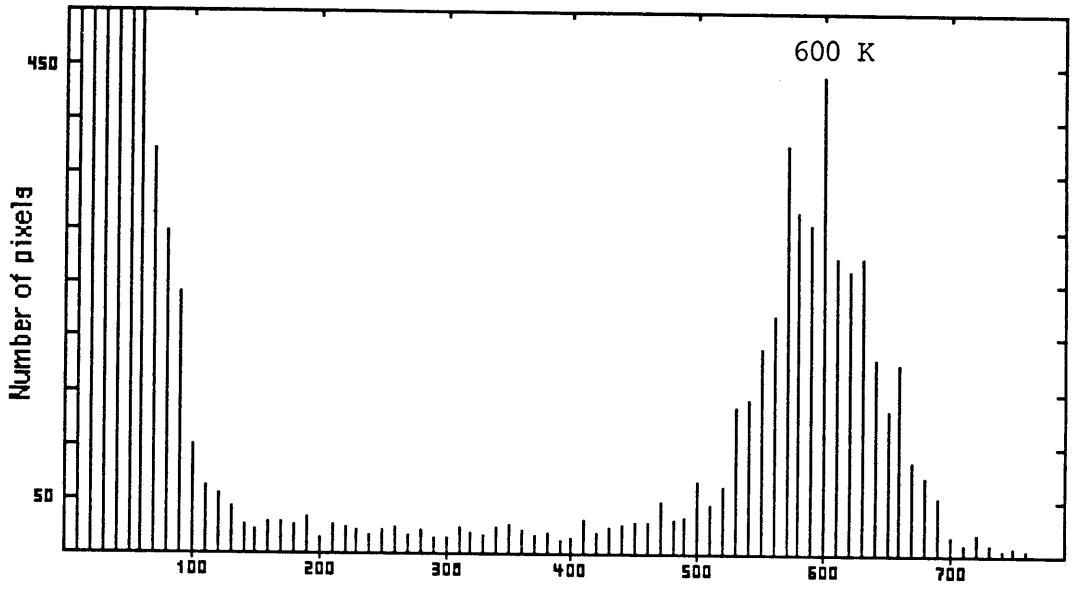


Figure 2-13
Histogram of T_B for Figure 2-11.
Venus - November 12, 1983 at λ = 20 cm

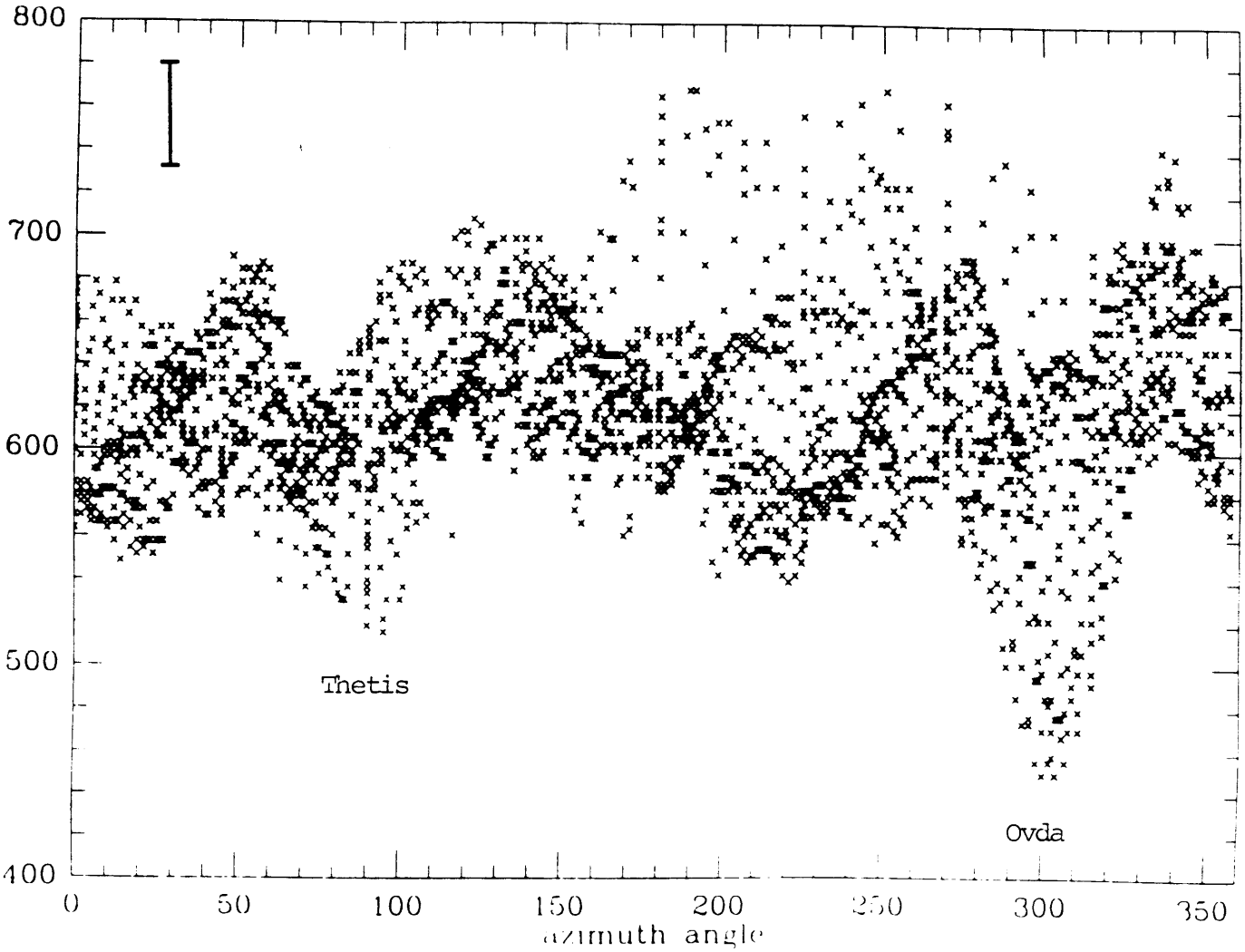
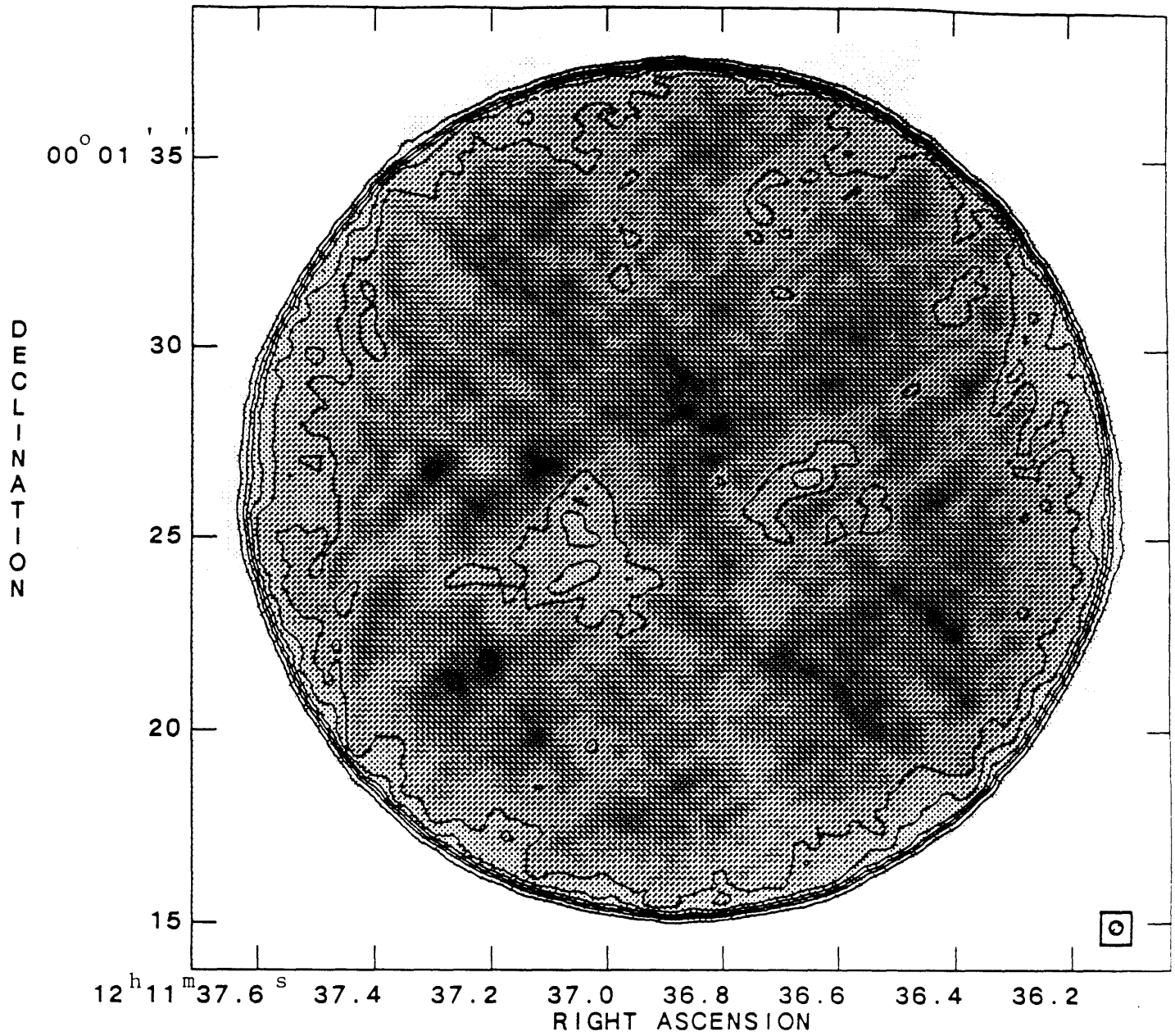


Figure 2-14
Brightness temperature of each pixel of Figure 2-11 versus azimuth angle counterclockwise from South.

Observed on the same date as Figure 2-11, Figure 2-15 differs in the wavelength of the observations. These 6 cm observations yield a resolution better by a factor of 3 than the 20 cm observations of Figure 2-11, but offer more difficulty in reconstruction, mainly because of the more restricted range of baselines available. Some sidelobe structure is still present in this image, as may be seen, for example, by the deviation from circularity of the outermost brightness contours. As discussed in Appendix A3, the flux values were reduced by 0.08 . A histogram plot of the brightness temperature values are displayed in Figure 2-16, with the width of each bin measuring 10° K. Figure 2-17, which plots the measured T_B's *versus* azimuth shows Aphrodite's presence, but artificial features at the limb caused by the difficulty of cleaning this image (see section 2.3) confuse this plot. Brightness temperatures as low as 450 K are found at the location of Aphrodite. Figure 2-18 is a comparison of the average brightness temperatures at λ = 6 cm and λ = 20 cm.



S(Jy x 10^{-4})	4.6	7.4	9.2	11	12.9	14.7	19.3	Peak 2.0 mJy
T_B(K)	184	294	368	442	514	588	772	Peak 797 K

Figure 2-15

Contour-grey scale plot of Venus - November 12, 1983 λ = 6 cm. Aphrodite Regio near center is more highly resolved than with λ = 20 cm result shown in Figure 2-11.

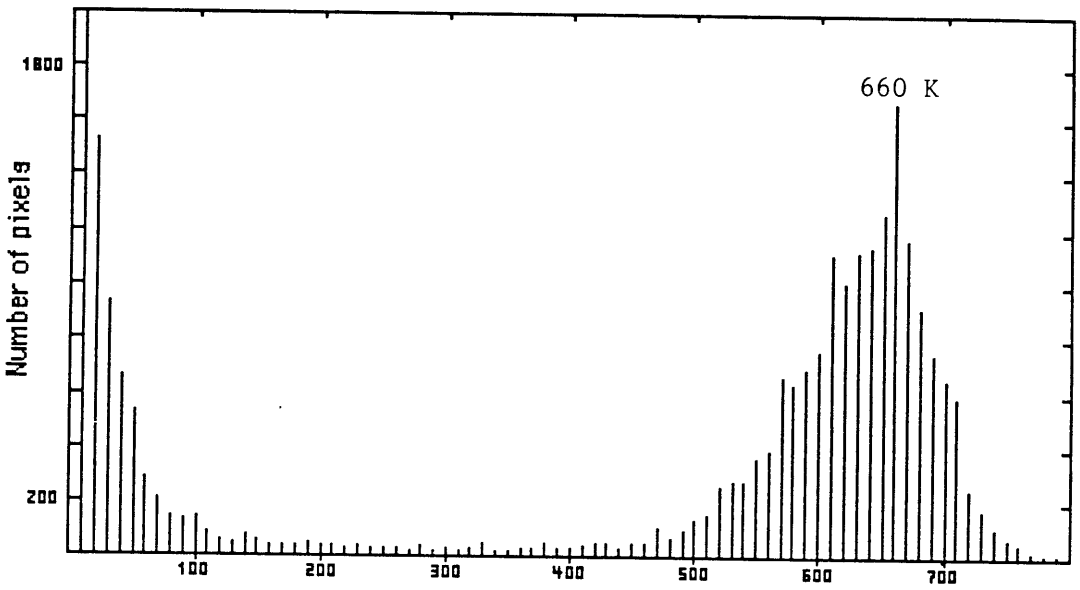


Figure 2-16
Histogram of T_B for Figure 2-15.

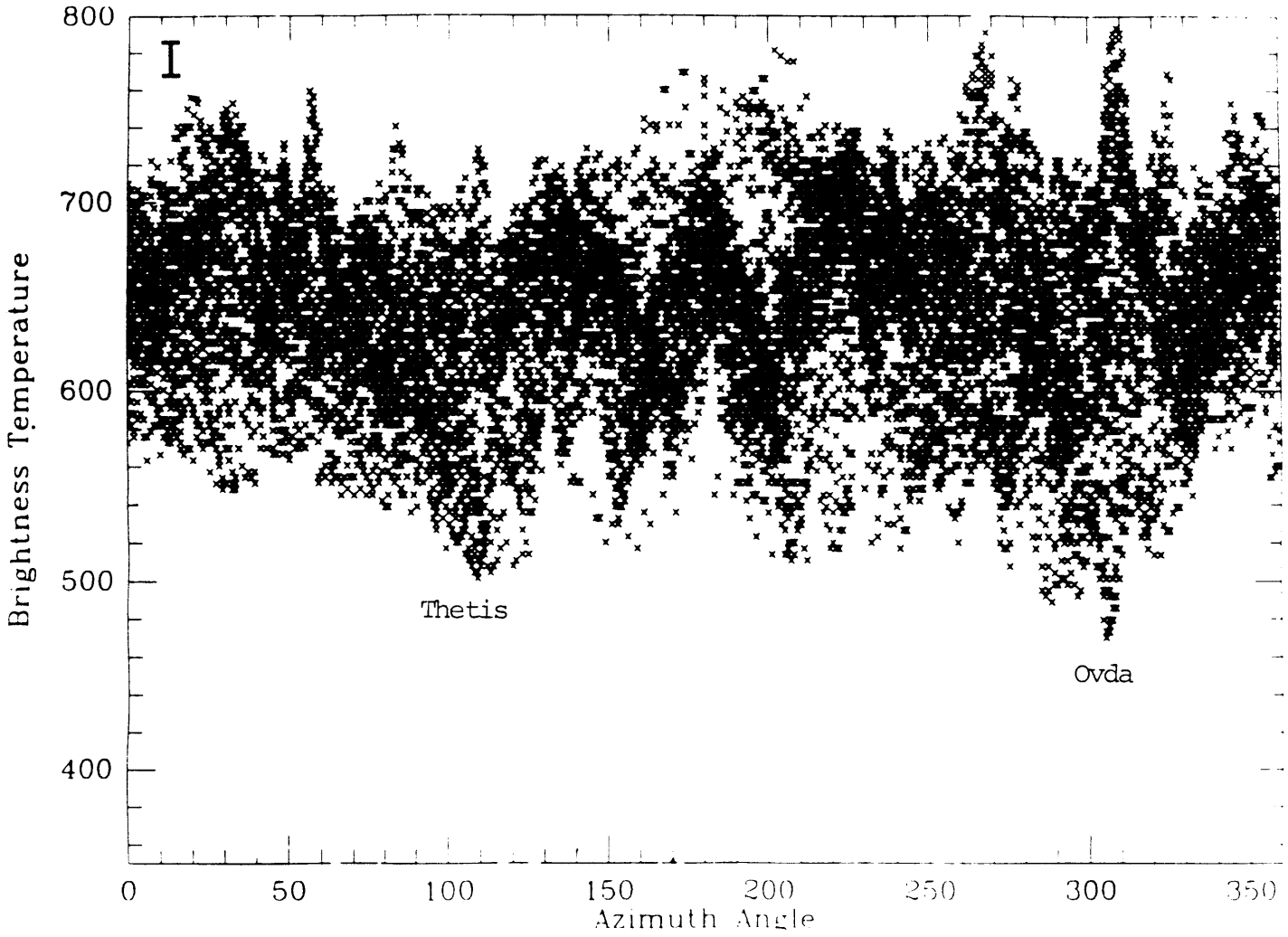


Figure 2-17
Brightness temperature of each pixel of Figure 2-15 versus azimuth angle counterclockwise from South.

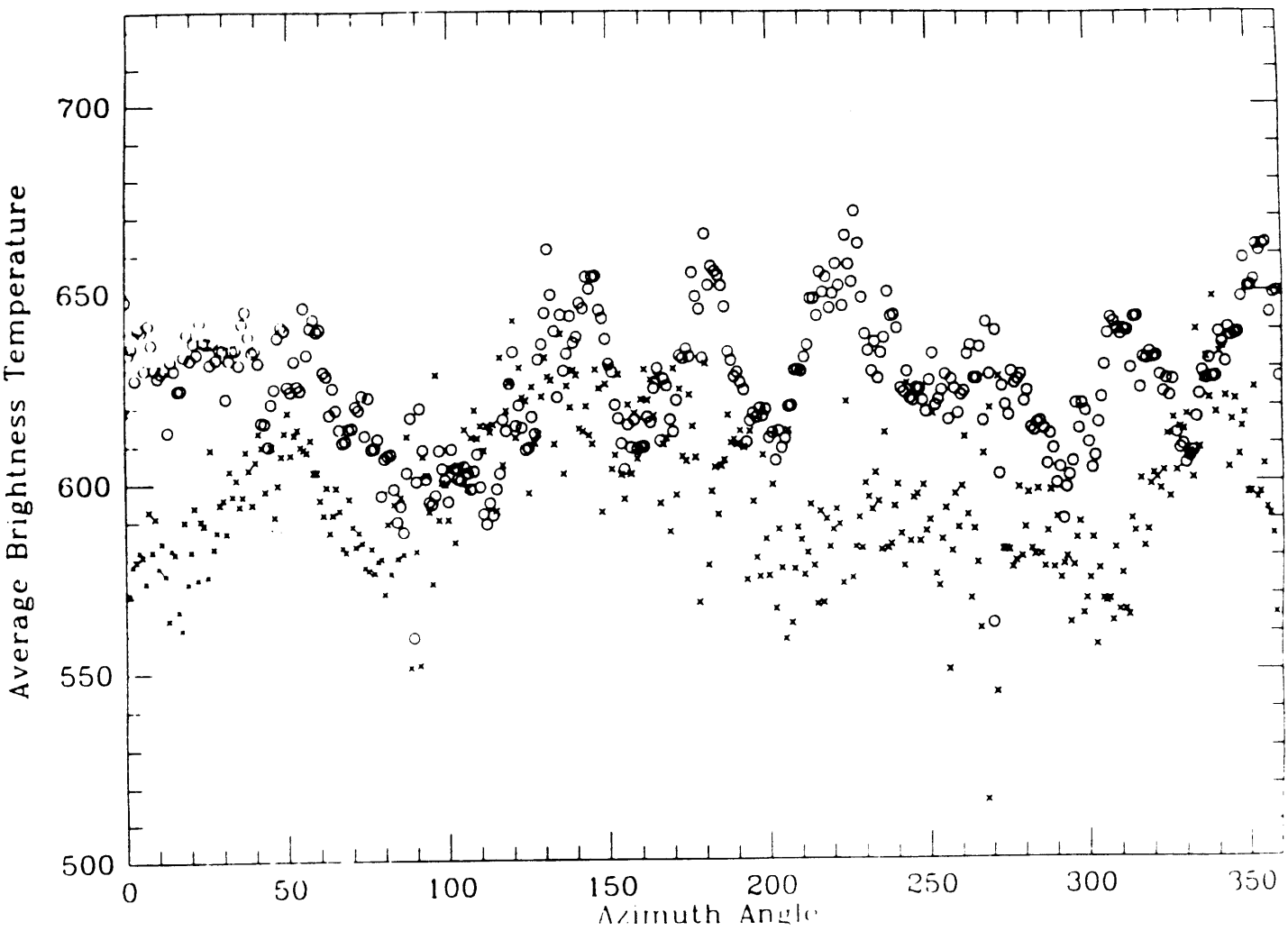


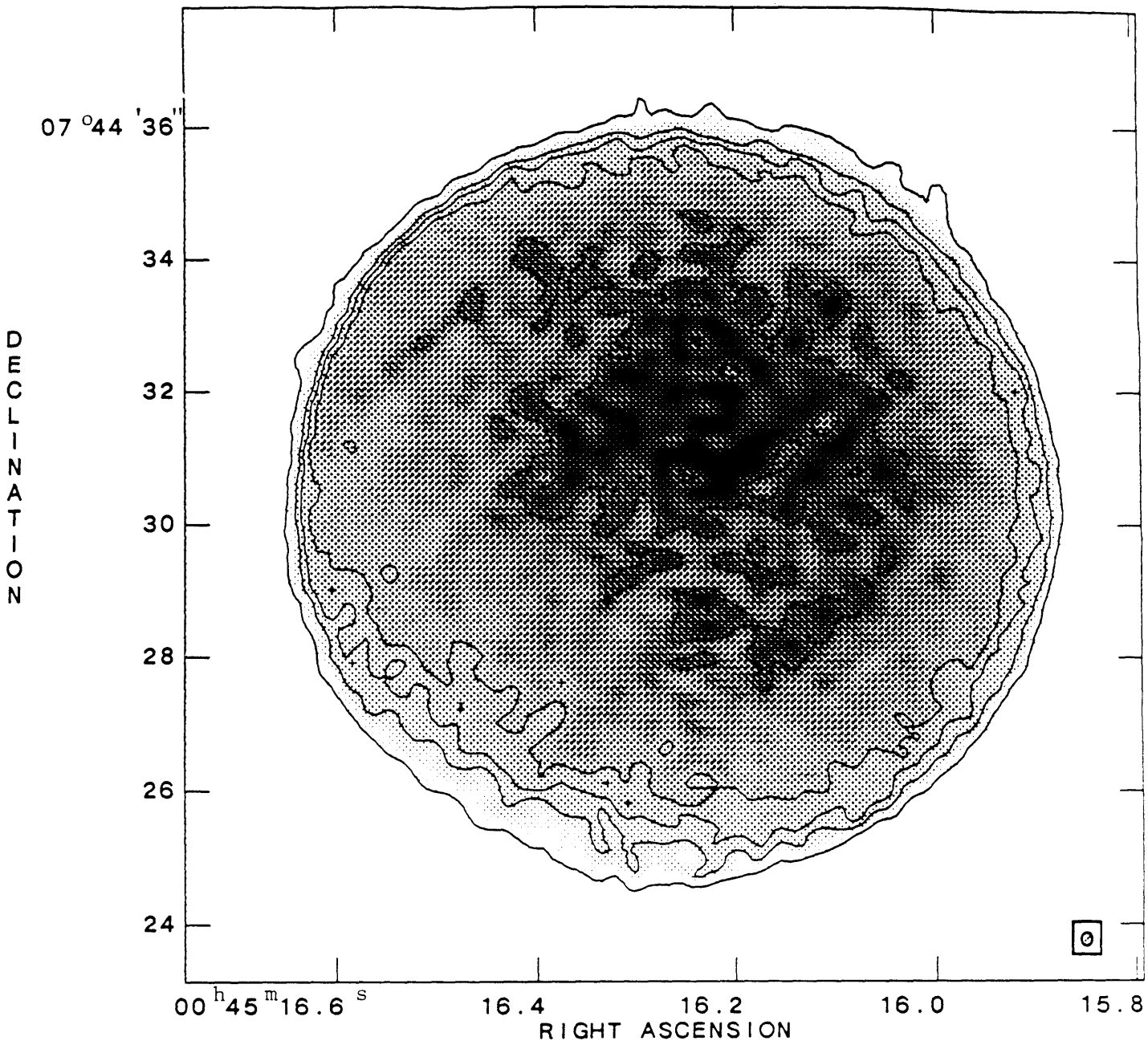
Figure 2-18
Average brightness temperature at each azimuth *versus* azimuth angle counterclockwise from South for both Venus November 12, 1983 λ = 20 cm and λ = 6 cm data. λ = 20 cm data indicated by x's, λ = 6 cm data by circles.

2.4.2.2 Stokes I Maps - Mercury Data

On April 4, 1985 the planet Mercury was observed at a wavelength of 2 cm. The VM map appears in Figure 2-19. The planetocentric coordinates are shown in Figure 2-20, where the unlit side of Mercury is indicated by the grey shading. As can be seen, virtually the entire disk of the planet is in shadow. The location of known surface features, including Caloris, are indicated. Figure 2-21 shows a histogram of the brightness temperature values, with each bin 5° K in width. Figure 2-22 indicates the variation in average brightness temperature as a function of azimuth, measured counter-clockwise from South. The average values range from 260 K at 300 to 350 degrees azimuth to 320 K at 100 to 250 degrees in azimuth.

Figure 2-23 is an image of nearly the same orientation of Mercury (April 5, 1985) at a wavelength of 6 cm. The resolution is a factor of 2 worse at this wavelength. Figure 2-24 is a histogram plot of these brightness temperature values. Figure 2-25, which again is a plot of the average brightness temperature as a function of angle, is clearly similar in form to Figure 2-22, though the changes in average brightness temperature are more indistinct. Brightness temperatures range from 350 K at 90 degrees in azimuth to 250 K at 270 degrees in azimuth.

Most notably apparent in the total intensity maps of Mercury, is, unsurprisingly, the temperature variation over the surface, as produced by the solar insolation. Variation in brightness temperature associated with known surface features are not discernable, unlike the results of the Venus observation.



S(Jy x 10^{-4})	10	20	25	30	40	45	Peak 4.86 mJy
T_B(K)	87	174	218	261	348	392	Peak 423 K
T_P(K)	83	167	209	250	333	376	Peak 405 K (Assuming ε=2.1, e=0.958)

Figure 2-19
Contour-grey scale plot of Mercury - April 4, 1985 λ = 2 cm.

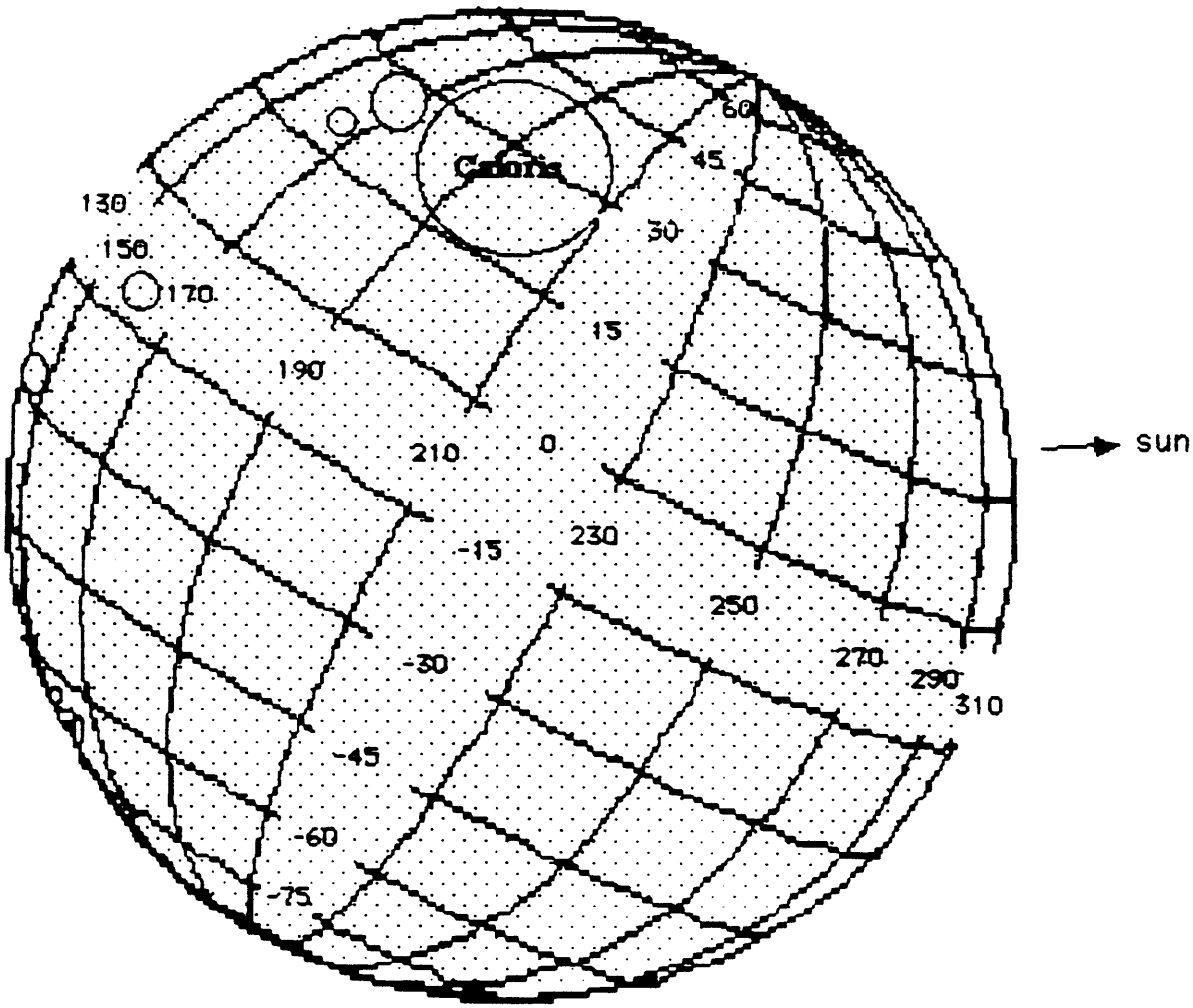


Figure 2-20
Planetocentric coordinates corresponding to Figure 2-19 and 2-23. Stippled area is not illuminated by the sun.

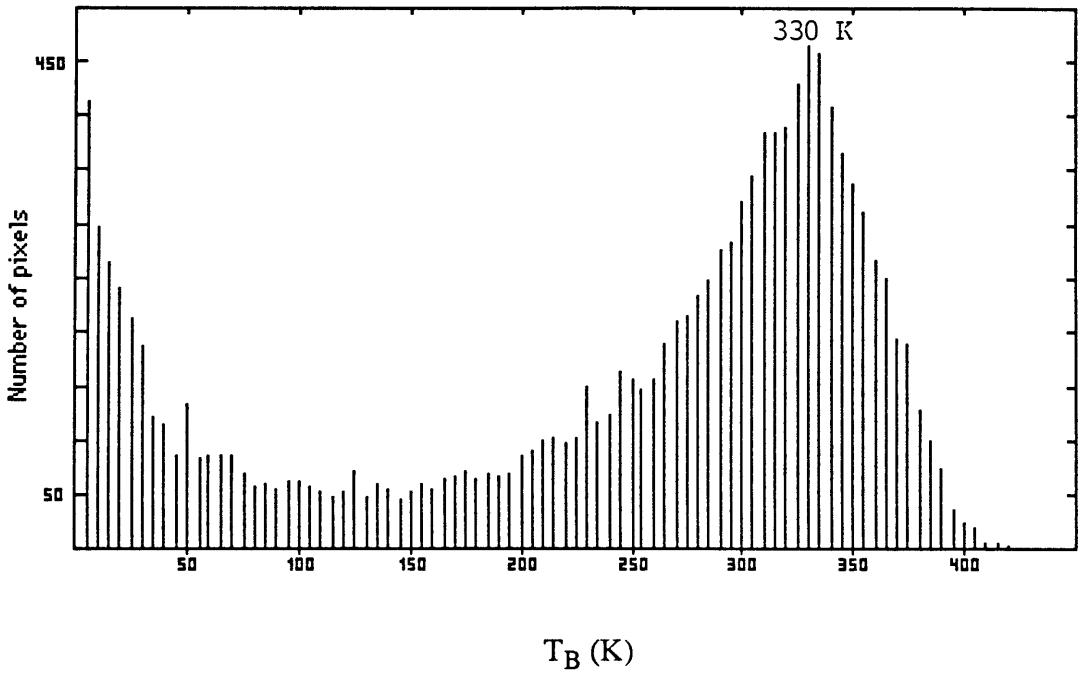


Figure 2-21
Histogram of T_B for Figure 2-19.

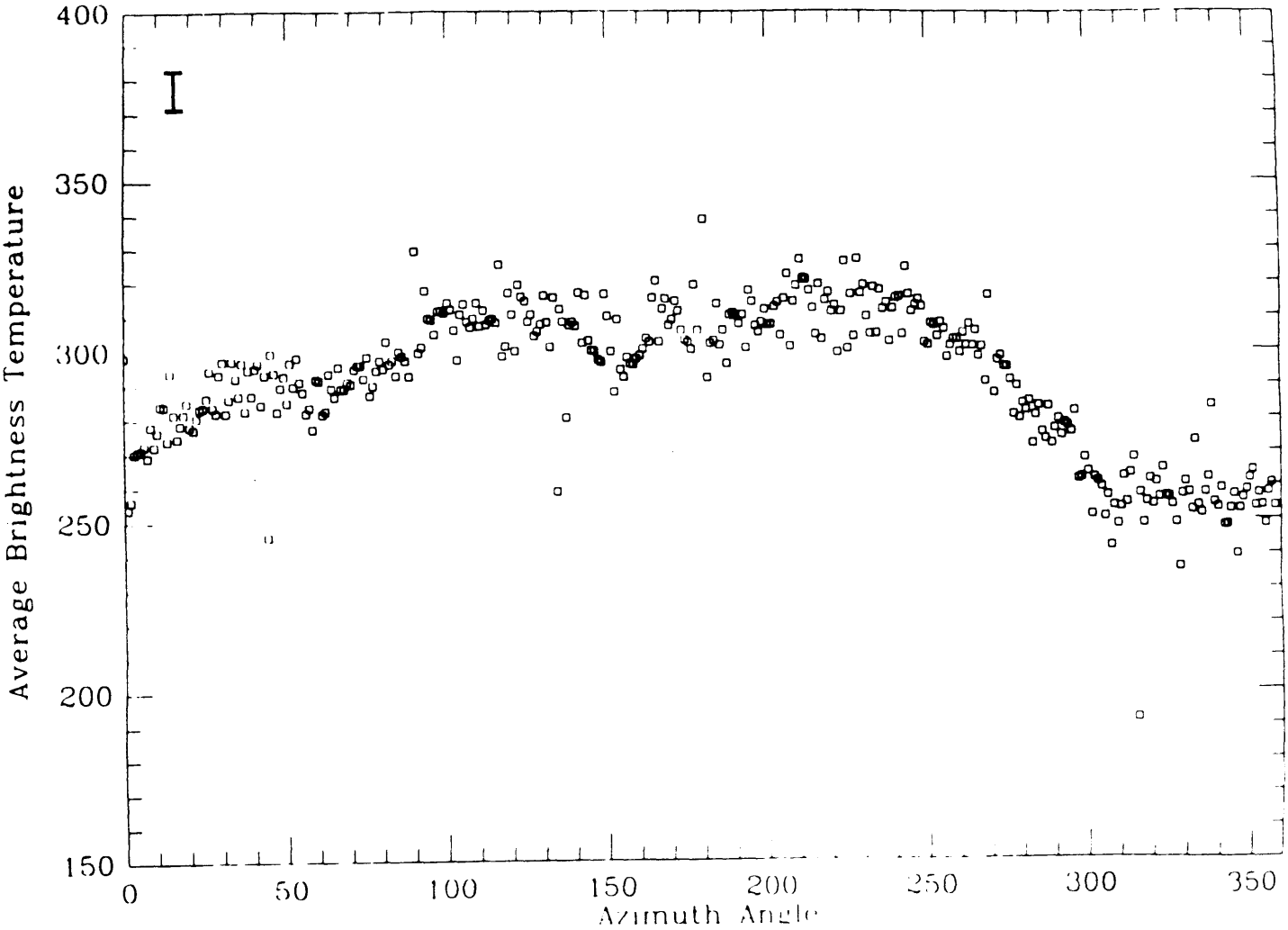
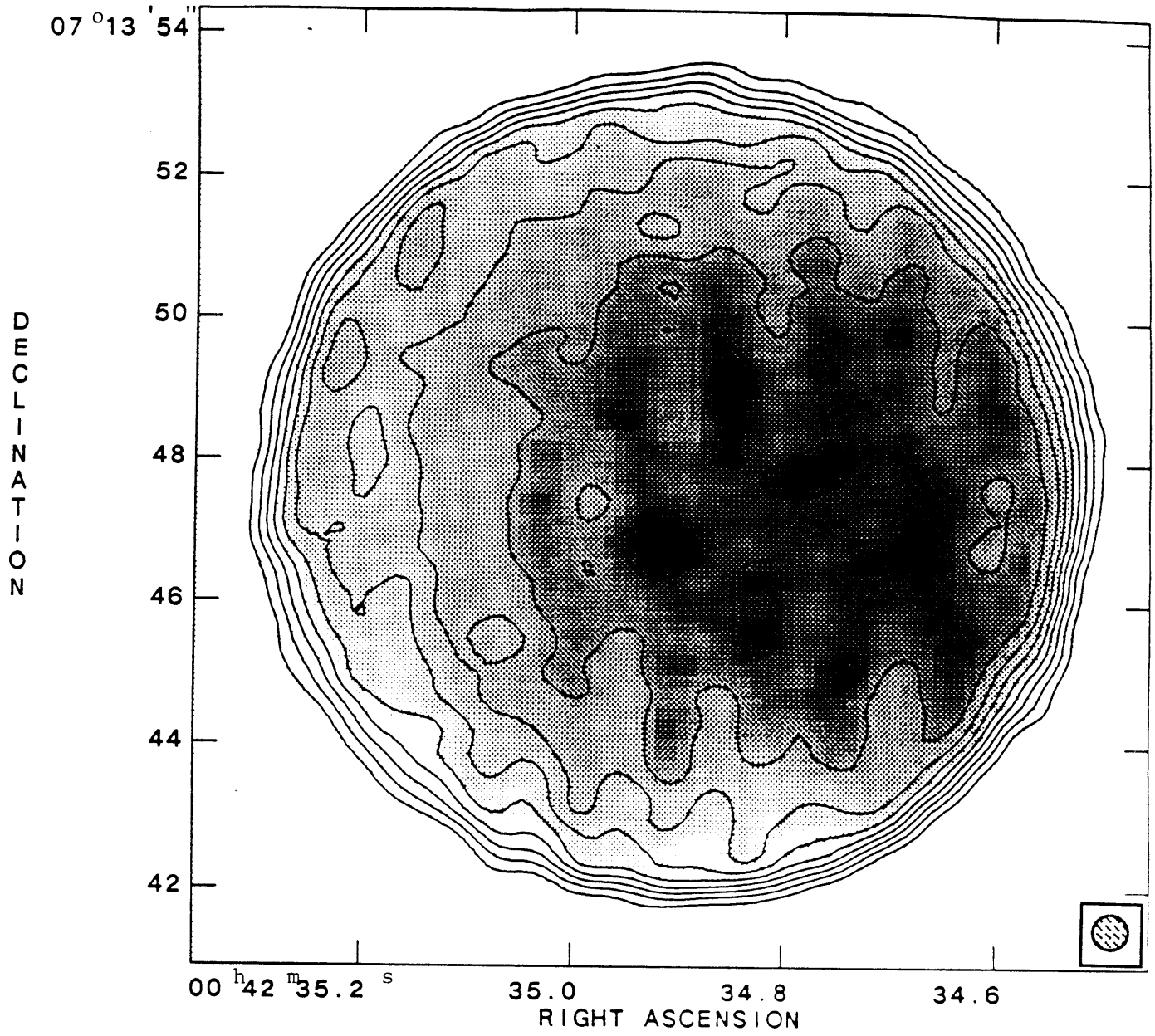


Figure 2-22
Average brightness temperature versus azimuth angle counterclockwise from South for Mercury April 4, 1985 λ = 2 cm.



S(Jy x 10^{-4})	3	5	7	9	11	13	15	17	19	Peak 2.025 mJy
T_B(K)	59	98	137	176	215	255	294	333	372	Peak 396 K
T_P(K)	57	94	131	169	206	244	282	319	356	Peak 379 K

(Assuming ε=2.3, e=0.958)

Figure 2-23
Contour-grey scale plot of Mercury - April 5, 1985 λ = 6 cm.

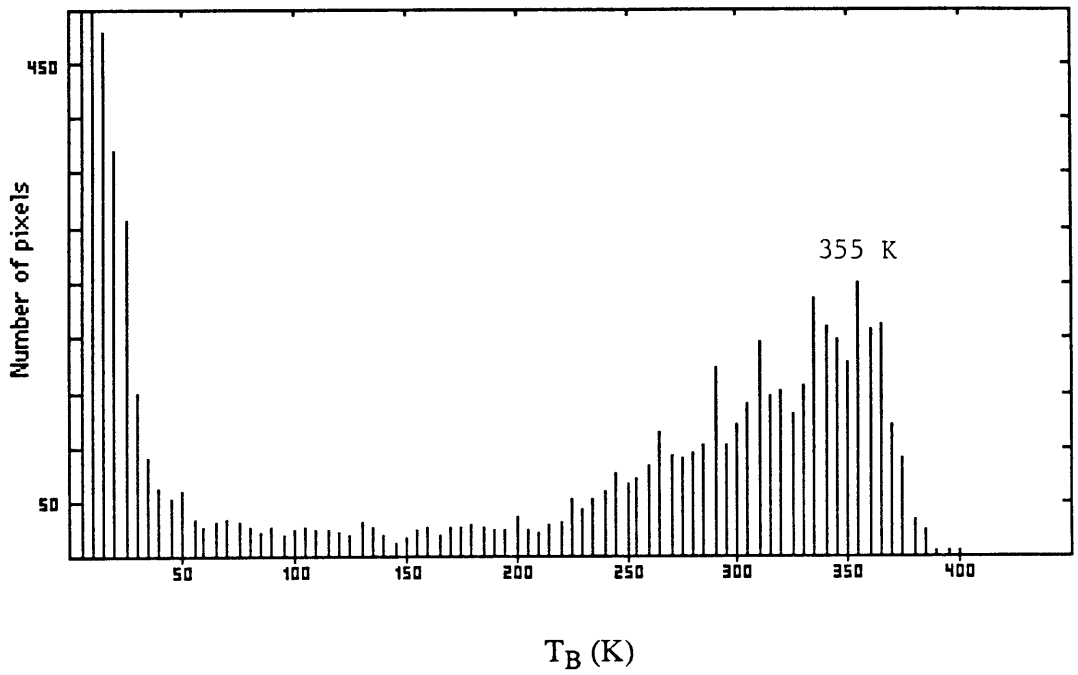


Figure 2-24
Histogram of T_B for Figure 2-23.

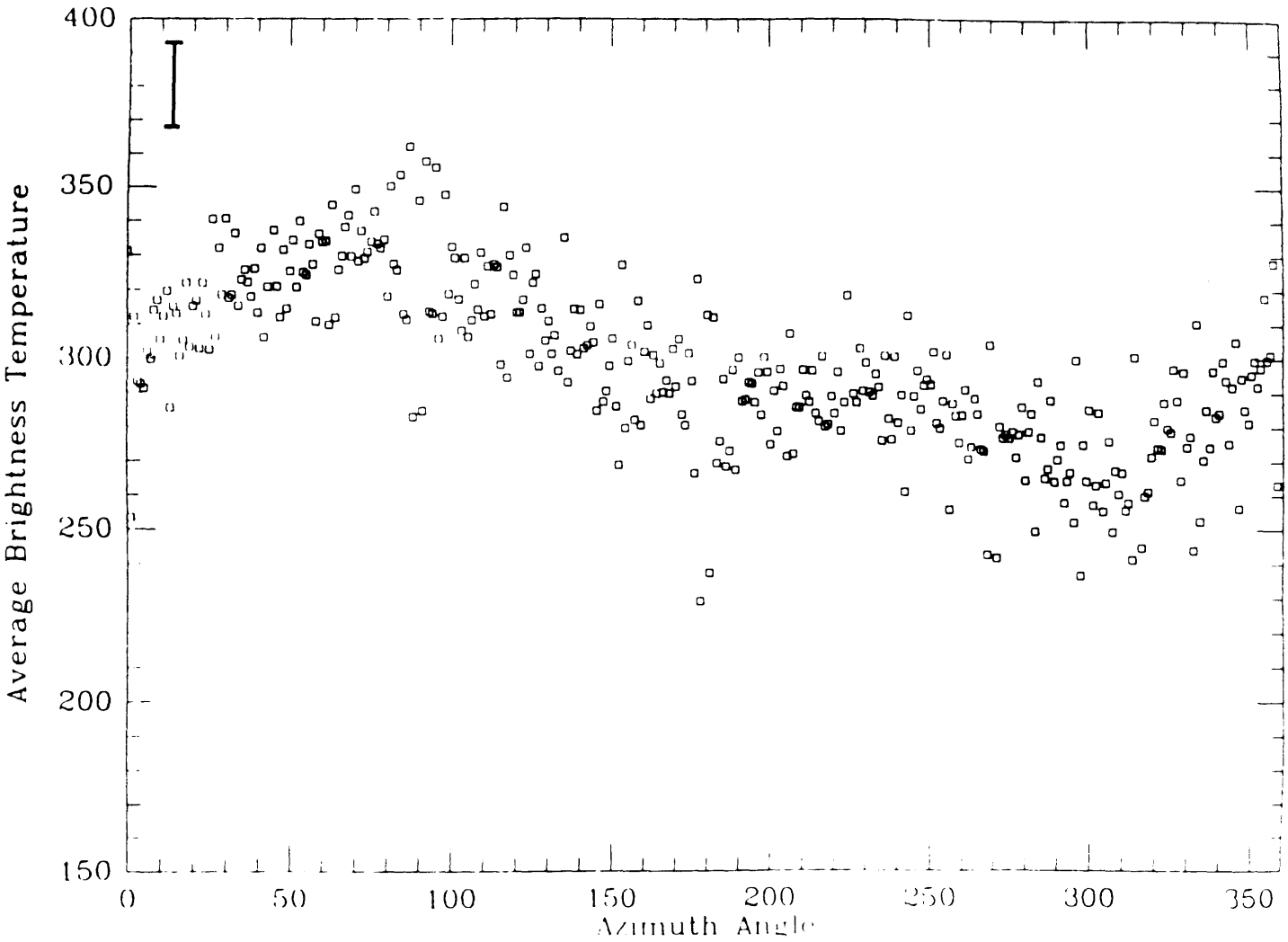


Figure 2-25
Average brightness temperature versus azimuth angle counterclockwise from South for Mercury April 5, 1985 λ = 6 cm.

2.4.3 The Polarization Intensity Maps

Figures 2-26 to 2-30 are maps of the observed polarization intensity (PI) obtained for Venus and Mercury. As discussed in section 2.3, these images were obtained from the Stokes U and Q maps by finding the quantity $\sqrt{U^2 + Q^2}$ in the map plane. Of course, by the nature of this operation, no value in the resultant map can be less than zero. The corresponding maps of the polarization angle agree closely with that expected: i.e., where the polarized flux is significantly above the noise, the angle of polarization points toward the center of the disk (See section 3.1).

Figures 2-26, 2-27, and 2-29 show that the polarization increases rapidly near the limb of the planet. Figure 2-26 is a map of the polarization of Venus that was obtained on October 3, 1983 at a wavelength of 20 cm, and is from the same database as Figure 2-7. Figure 2-27 is a PI map obtained concurrently with the Stokes I map of Figure 2-11. The elevated polarization near the center of the image is anomalous, and appears to be unrelated to normal emissions from the planet's surface or to illumination by the sun (see discussion of central T_B anomaly of Figure 2-7 in section 2.4.2.1). Figure 2-29 is the PI map corresponding to the April 5, 1985 λ = 6 cm observations of Mercury.

Figures 2-28 and 2-30 are plots of the polarization intensity that yielded low values. Figure 2-28, which shows the polarization intensity for the observations of Venus on November 12, 1983 at λ = 6 cm, still indicates a hint of the expected polarization behaviour. However, due, most likely, to surface roughness and attenuation (and unpolarized emission) by the atmosphere, the values are substantially reduced relative to the λ = 20 cm Venus PI maps. Similarly to Figure 2-27, there are anomalously elevated polarization values near the center. It is possible that VLA artifacts have produced both the λ = 20 cm and λ = 6 cm features (see section 2.4.2.1). Figure 2-30 demonstrates the low polarization values found during the April 4, 1985 λ = 2 cm observations of Mercury. Surface roughness, which acts to reduce Fresnel emission polarization, has obviously

become a critical factor at this wavelength. The polarization intensity is only slightly above the noise.

These maps of the polarization intensity have clear azimuthal asymmetries. Factors that may influence these variations in polarization include observational (low signal to noise, instrumental polarizations, inadequate CLEANing) and physical (variations in surface roughness, dielectric constant, morphology, temperature, atmospheric effects) causes. See section 2.5 for a discussion of the reliability of the PI maps, and their quantitative errors.

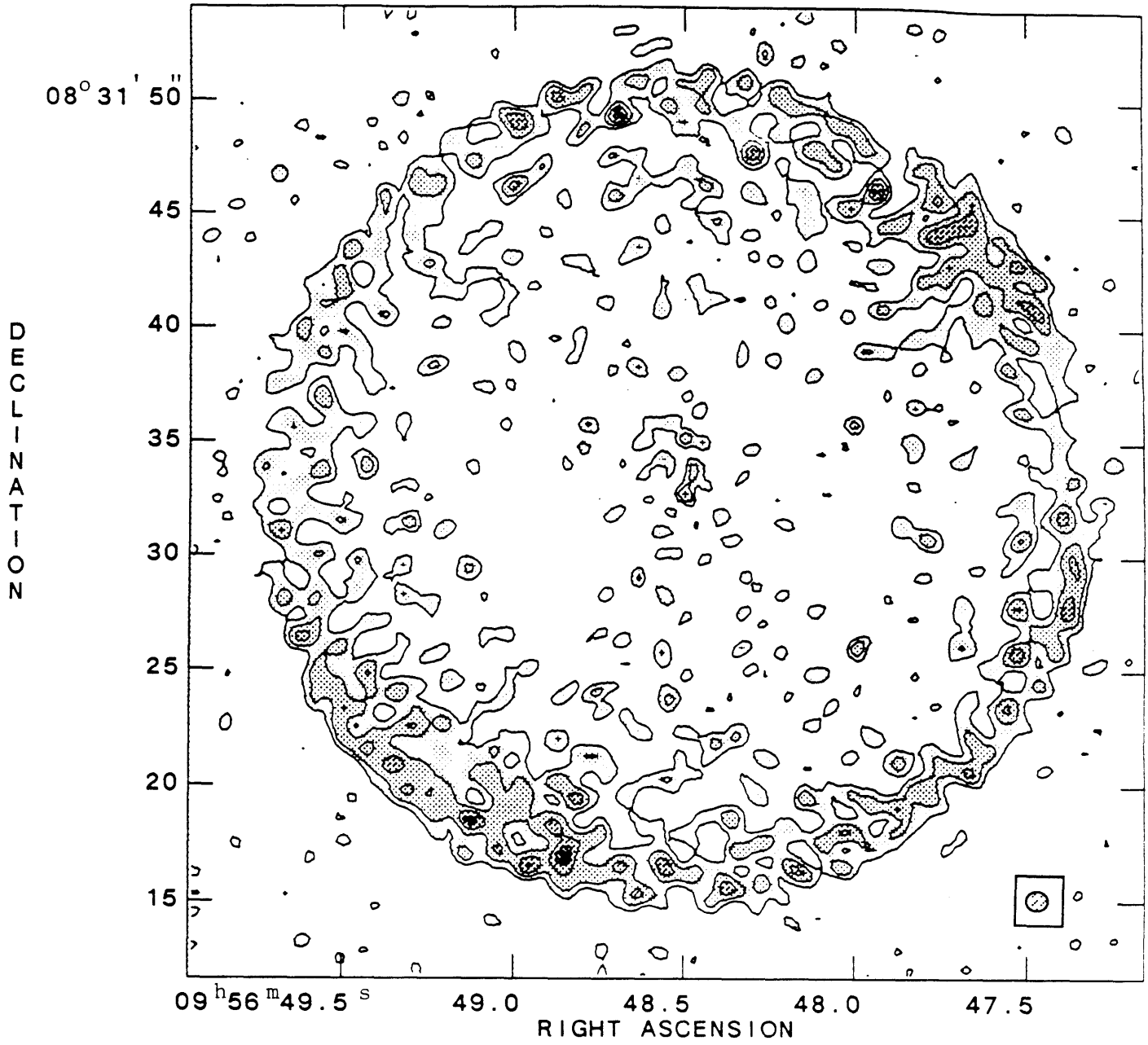


Figure 2-26
Polarization intensity of Venus on October 3, 1983 at $\lambda = 20$ cm.

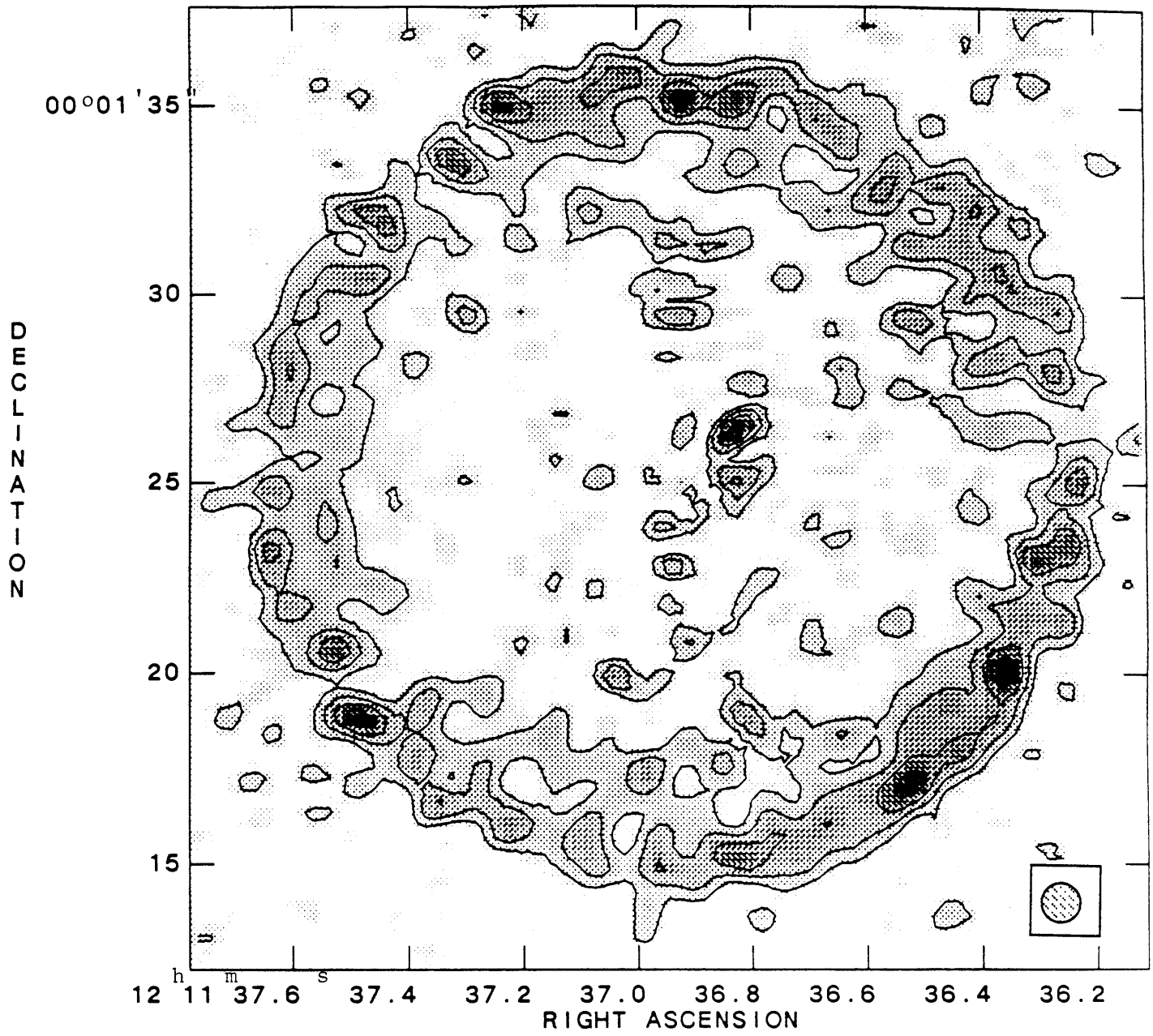


Figure 2-27
Polarization intensity of Venus on November 12, 1983 at λ = 20 cm.

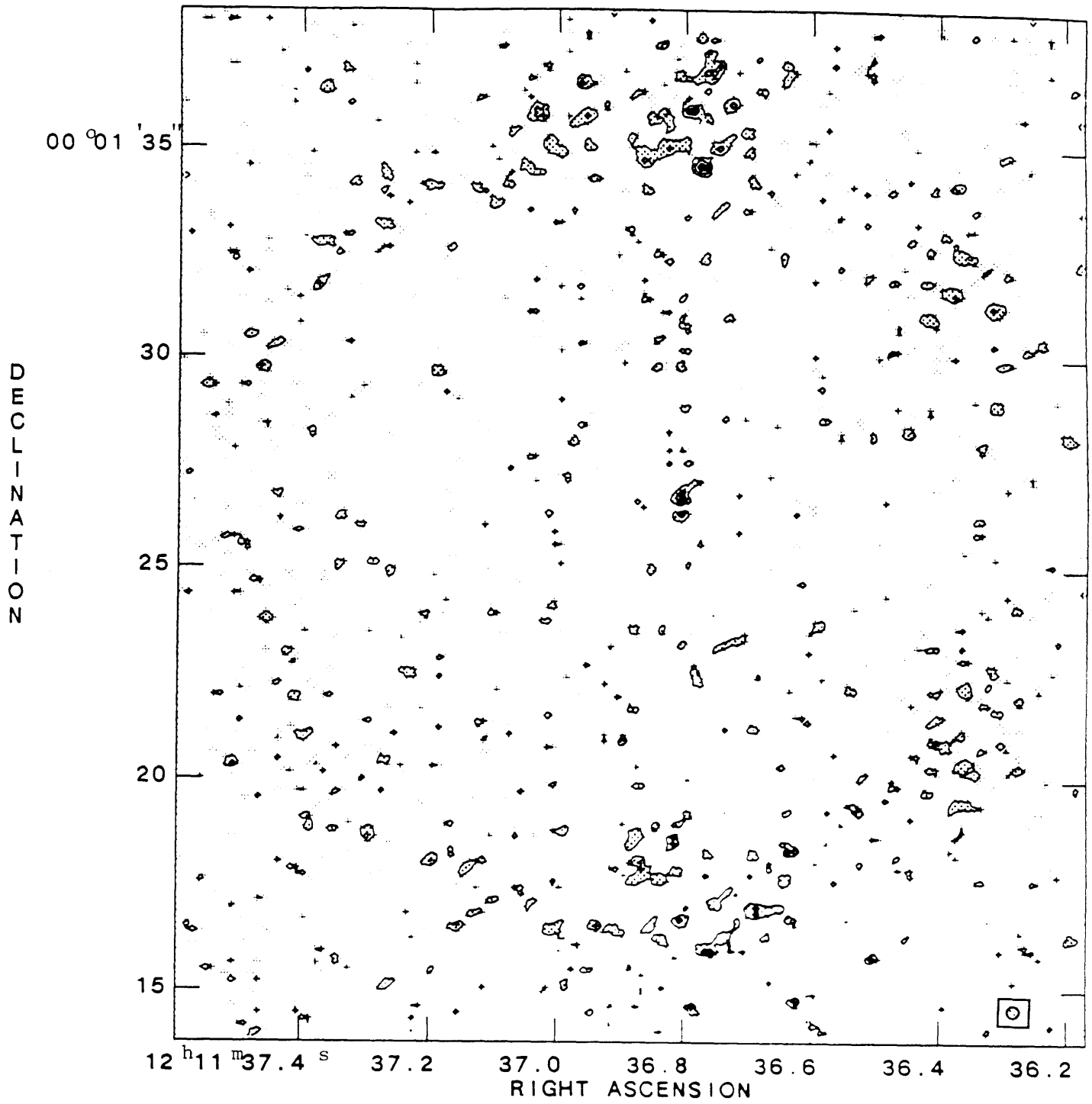


Figure 2-28
Polarization intensity of Venus on November 12, 1983 at λ = 6 cm.

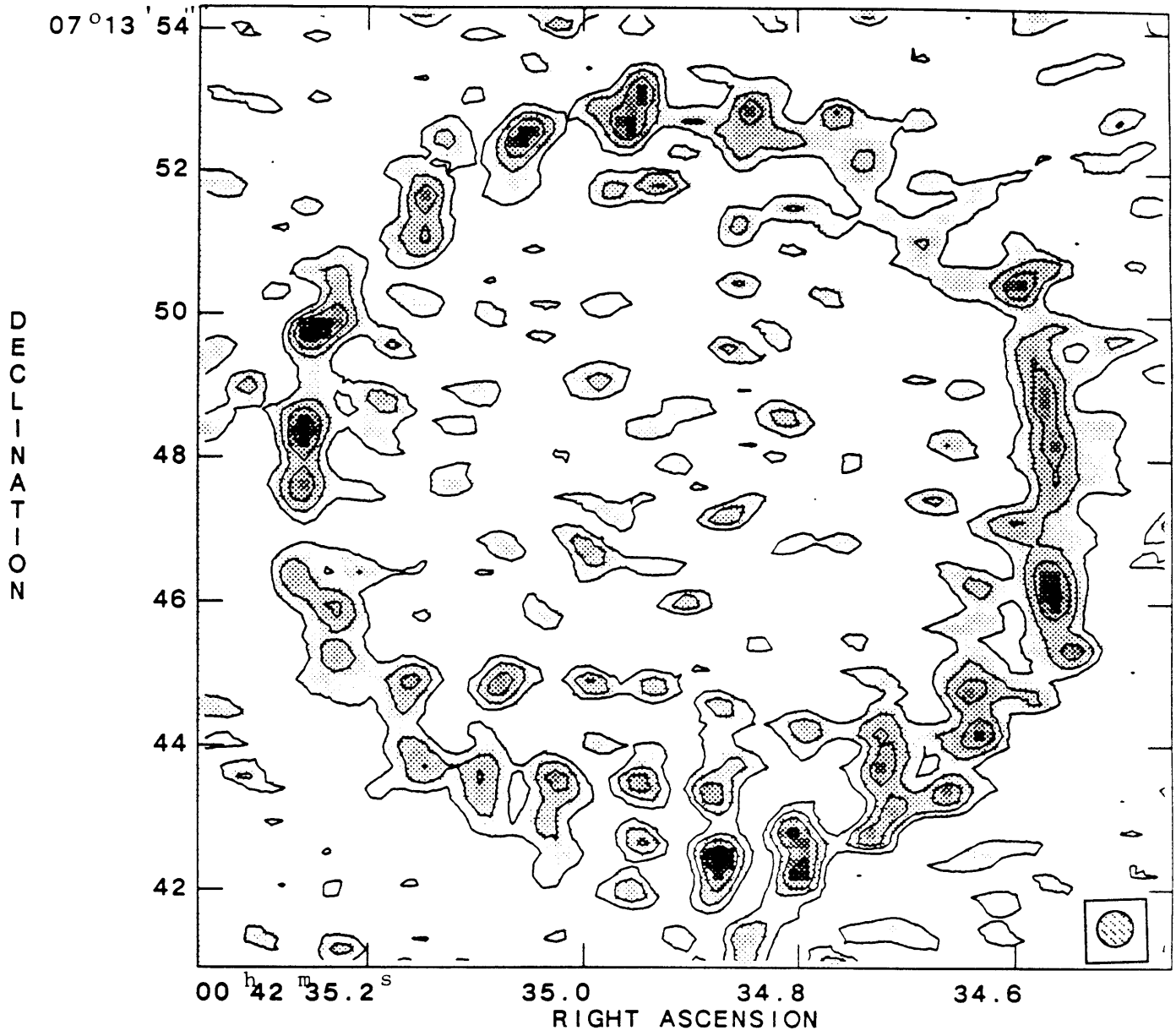


Figure 2-29
Polarization intensity of Mercury on April 4, 1985 at λ = 6 cm.

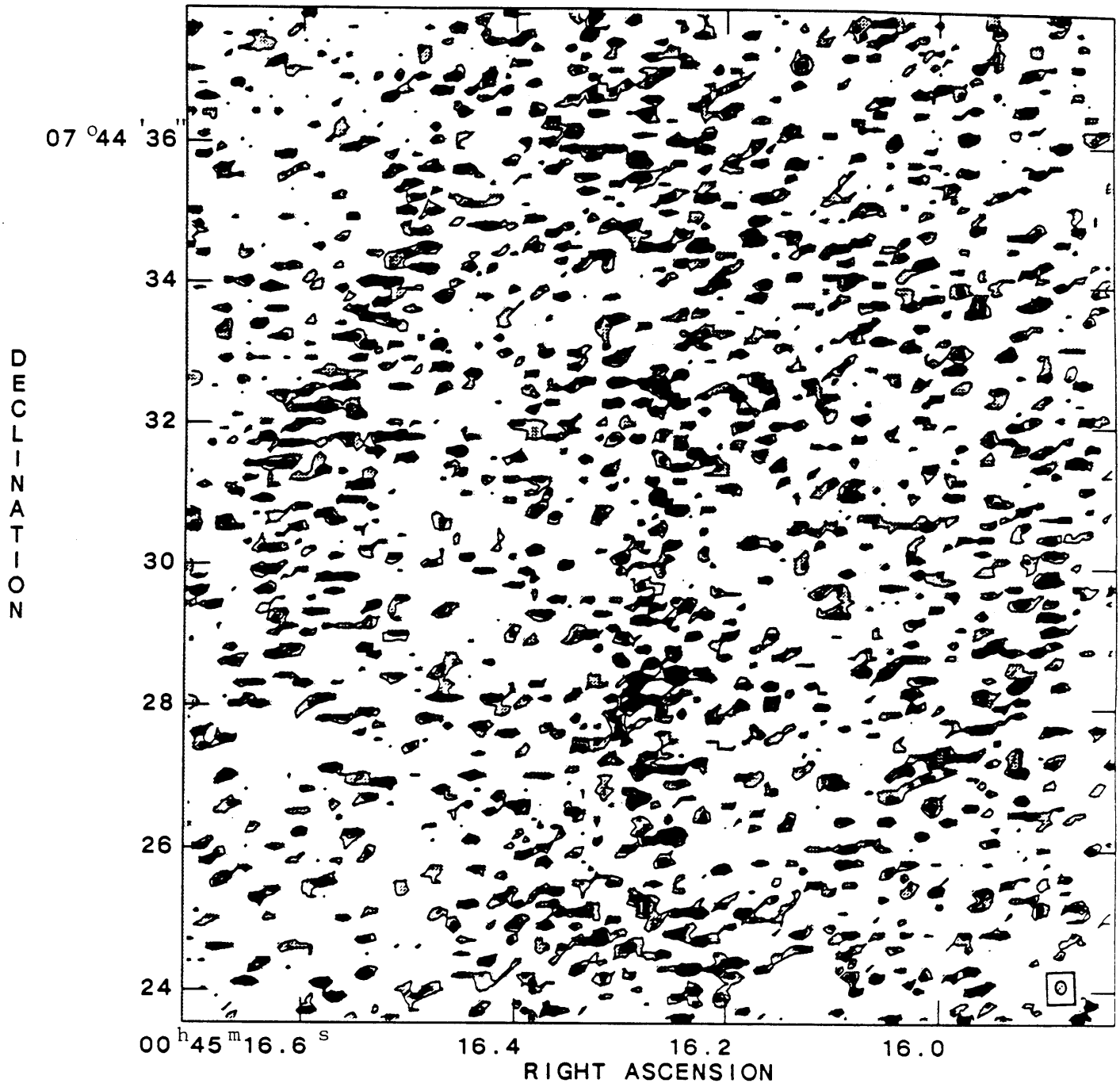


Figure 2-30
Polarization intensity of Mercury on April 5, 1985 at λ = 2 cm. Note the almost total absence of measurable polarization at this wavelength.

2.5 Reliability of Images

Given the incomplete sampling of the visibility data, the dirty maps are but one solution to the Fourier transform, where the amplitude of the visibility functions at the unsampled spatial frequencies u and v were set to zero. This 'principal solution' (Cornwell, 1982) may be constrained by additional conditions that may resolve the confusion over the true distribution of the emissions.

The CLEAN algorithm assumes that the field of view is comprised of an assemblage of point sources. CLEAN iteratively finds the position and strength of those point sources, and then reconstructs the image. In the absence of noise, CLEAN will produce a unique solution. In practice, noise (and using a Fast Fourier Transform to produce the dirty image) prevents us from ascertaining whether the result is unique.

CLEAN is not understood theoretically. For instance, CLEAN has not been successfully subjected to an error analysis (Cornwell, 1982). Also, depending on the parameters chosen that control the algorithm, slightly different images may be produced from identical data sets. Monte Carlo analyses provide the only tests of the reliability and repeatibility of the images, as well as a measure of which parameters significantly effect the outcome. It is thus up to the observer to select the most effective cleaning strategy.

The maximum entropy method (implemented as VM on AIPS) has been developed as an alternative to CLEAN in analysing VLA data (Cornwell and Evans, 1985). Its most successful application has been its use with radio sources of large extent, and where the sidelobe level is small. It is less successful for small images consisting of point sources with very high dynamic ranges (Cornwell and Evans, 1985). VM is well suited to planetary images, because of the flat, extended, well-defined plateau of emission that is characteristic of planetary thermal emission.

VM has not been used as extensively as CLEAN, and therefore has not been subjected to the test of time that CLEAN has. However, it has been shown that for objects

covering many resolution elements, the performance of VM can match or exceed that of CLEAN (Cornwell and Evans, 1985).

When using VM, we should be aware of two potential sources of misinformation : 1) the resultant map will not have zero mean noise, but will be positively biased, as an inherent result of the maximization of entropy. This bias arises because the solution is a function of the logarithm of the ratio of the reconstructed to expected map pixel values (subject to the constraints imposed by the data); and 2) superresolution is possible, depending on the signal to noise. In order to minimize this effect, the VM maps were convolved with a gaussian corresponding in width to the synthesized beam.

All of the CLEANed and VMed maps presented in the previous section were subjected to Monte Carlo tests to ascertain the reliability and repeatibility of the images. In general, the sampling at the spatial frequencies was sufficiently complete that the sidelobes of the dirty maps did not exceed about 10% or less of the map maximums. Significant features in the CLEANed or VMed maps were generally also present to some extent in the dirty maps. We feel that the best estimate of the quality of the images is the noise level outside the planetary emissions (see Table 2-5).

The polarization intensity maps were particularly difficult to CLEAN, because of the low signal to noise of the extended emissions. As can be seen in Figures 2-26 to 2-30, artifacts at the center, and vertical striping are common to all of the polarization maps. Because there are no negative values, the effect of these deconvolution errors is to introduce a positive bias to the data, particularly at the center of the images. The rms error of the Venus λ = 20 cm polarization maps is 0.05 mJy (calculated outside of the physical extent of the disk of Venus), while for the Mercury λ = 6 cm map the rms error is 0.07 mJy. The rms error of the λ = 6 Venus PI map is 0.03 mJy, and is 0.2 mJy for the λ = 2 cm Mecury PI map.

Chapter 3. Polarization Properties

3.1 Theory

It is well known that the radio emission from planets is increasingly linearly polarized as one looks closer to the limb. We wish to determine the relationship between the degree of polarization of emitted radiation from the surface of a planet and that surface's dielectric constant. Such a relationship exists due to the polarization behaviour of electromagnetic waves as they interact with the surface of a dielectric medium. In the past, the method commonly used for determining the dielectric constant from the polarization of planetary radio emissions has been to measure the difference in brightness between orthogonal linear polarizations (Heiles and Drake, 1963), at varying projected baselines. If we assume the planet is a smooth dielectric sphere, the difference in brightness temperature observed in the two polarizations is :

$$\Delta T_B = \gamma T_s (e_p - e_n)$$

Where,

$$\gamma = \cos^2 (D - D_0) - \sin^2(D - D_0)$$

and,

$$e_n = \frac{4 \sqrt{\varepsilon_1 \mu_2 / \varepsilon_2 \mu_1} \cos\theta_i \cos\theta_t}{\{\sqrt{\varepsilon_1 \mu_2 / \varepsilon_2 \mu_1} \cos\theta_i + \cos\theta_t \}^2} \qquad (3.1)$$

$$e_p = \frac{4 \sqrt{\varepsilon_1 \mu_2 / \varepsilon_2 \mu_1} \cos\theta_i \cos\theta_t}{\{\sqrt{\varepsilon_1 \mu_2 / \varepsilon_2 \mu_1} \cos\theta_t + \cos\theta_i \}^2} \qquad (3.2)$$

ΔT_B is the difference in brightness temperature between the two orthogonal polarizations, θ_t is the angle between the direction of propagation and a normal to the surface, ε is the complex dielectric constant (the subscripts 1 and 2 indicate the region interior and exterior to the surface of the planet, respectively; see appendix A2 and figure A-1), μ is the magnetic permeability, T_s is the actual surface temperature, e_p is the transmission coefficient for emission polarized parallel to the plane of incidence, e_n is the transmission coefficient for emission polarized normal to the plane of incidence, D_0 is the direction the angle of linear polarization oriented on the planet's disc makes with respect to the planet's equator, and D is the angle at any point on the disc with respect to the planet's equator .

While this procedure is valid, current instrumentation such as that found at the Very Large Array simultaneously measures the incoming radiation with two orthogonal, circularly polarized feeds, and allows the mapping of the data in terms of Stokes polarization parameters. We therefore prefer a direct relationship between the dielectric constant and Stokes parameters for black body thermal radiation emitted by the surface of a dielectric sphere. We may describe the partial polarization of an electromagnetic wave by defining the parameters introduced by Stokes (Kraus,1966) :

$$I = \langle |E_x|^2 + |E_y|^2 \rangle = S$$

$$Q = \langle |E_y|^2 - |E_x|^2 \rangle = S \cos 2\eta \cos 2\tau$$

$$U = \langle E_y E_x^* + E_x E_y^* \rangle = S \cos 2\eta \sin 2\tau$$

$$V = \langle E_y E_x^* - E_x E_y^* \rangle = S \sin 2\eta$$

E_x and E_y are the electric field components in an (x,y) coordinate system. I = S represents the total flux of radiation received, V denotes the amount of circularly polarized power, and Q and U describe the amount of linearly polarized power. τ is the angle relating the arbitrary (x,y) coordinate system with the coordinate system defined by the polarization ellipse. The polarization ellipse is the ellipse traced out by the E vector due to the phase difference between two orthogonally polarized waves (see figure 3-1). η is the inverse cotangent of the axial ratio of the polarization ellipse (Kraus, 1966, p. 112).

When considering the transmission through a dielectric boundary, the axial ratio of the polarization ellipse is the magnitude of the transmitted E vector parallel to the plane of incidence divided by the magnitude of the transmitted E vector normal to the plane of incidence. We can make this association because of the tendency at all angles of transmission for the transmitted wave to be predominately polarized parallel to the plane of incidence (which implies that the magnitude of the transmitted E vector is a minimum when normal to the plane of incidence) (Jackson, 1975, P. 275). τ is then the tilt angle, or the angle of the transmitted E vector polarized parallel to the plane of incidence; that is, the angle of the normal to the interface with respect to the x reference axis.

Since we have no circularly polarized component, the degree of polarization, m, is defined as :

$$m = \sqrt{Q^2 + U^2} \; / \; I = \cos 2\eta \qquad (3.3)$$

See appendix 2 for a derivation of the relationship between η and the transmission coefficients e_n and e_p, where we find from equation A.2 that :

$$\eta = \cot^{-1} (e_p / e_n)^{1/2}$$

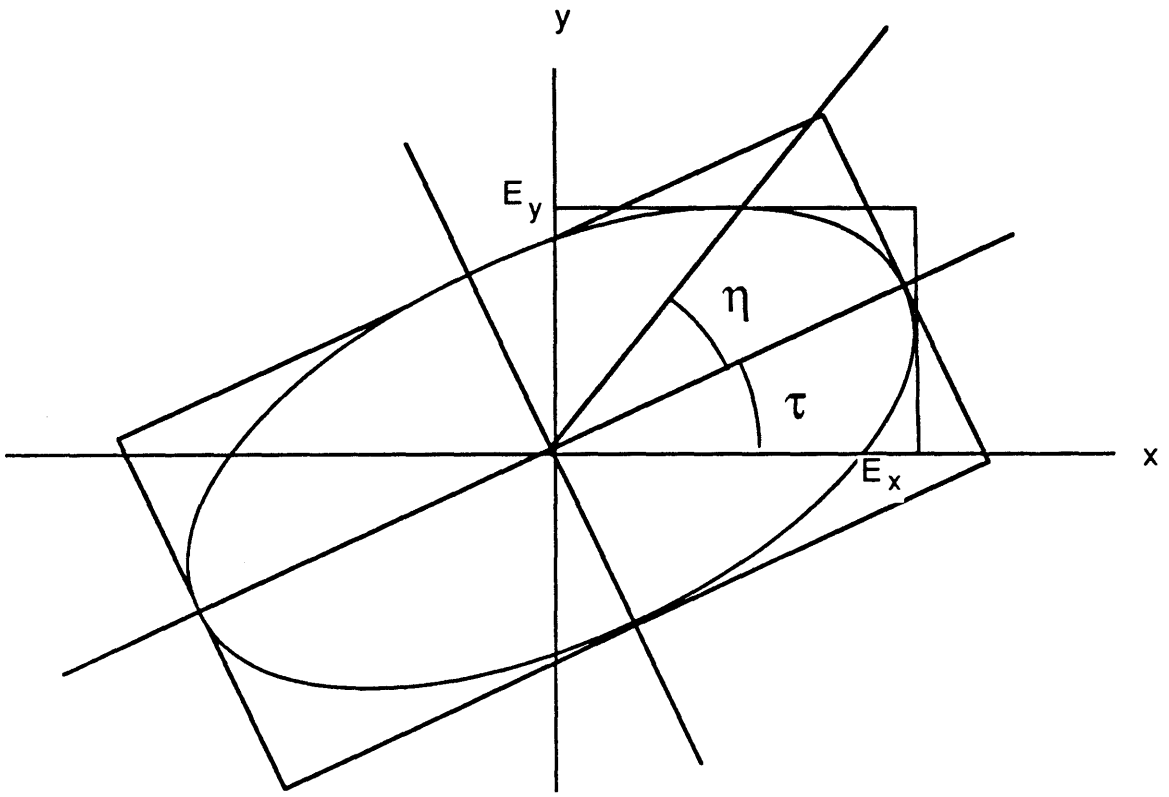


Figure 3-1
Polarization Ellipse

which, from equation 3.3, implies that

$$m = \cos \{2 \cot^{-1} (e_p / e_n)^{1/2} \} \qquad (3.4)$$

We see in equation (3.4) that the degree of polarization of radiation from a smooth dielectric sphere is simply a function of the transmission coefficients at the boundary. In order to obtain a simple analytical expression for the transmission coefficients we will assume that the conductivity of the surface is nearly zero (the dielectric constant is dominated by the real component). The transmission coefficients are then simply given by equations 3.1 and 3.2 .We find for the ratio of e_p / e_n:

$$\frac{e_p}{e_n} = \left[\frac{\sqrt{\varepsilon_1 \mu_2 / \varepsilon_2 \mu_1}\ \cos\theta_i + \cos\theta_t}{\sqrt{\varepsilon_1 \mu_2 / \varepsilon_2 \mu_1}\ \cos\theta_t + \cos\theta_i} \right]^2$$

which implies for the degree of polarization :

$$m = \cos \{2 \cot^{-1} \left[\frac{\sqrt{\varepsilon_1 \mu_2 / \varepsilon_2 \mu_1} \cos\theta_i + \cos\theta_t}{\sqrt{\varepsilon_1 \mu_2 / \varepsilon_2 \mu_1} \cos\theta_t + \cos\theta_i} \right] \} \qquad (3.5)$$

Similarly, the degree of polarization may be found for reflected radiation from the surface of a planet. Using the reflection coefficients instead of the transmission coefficients to relate the ratio of the normal and tangential components of the electric field vectors to the degree of polarization, we find that :

$$\frac{R_p}{R_n} = \left[\frac{\sqrt{\varepsilon_1\mu_2 / \varepsilon_2\mu_1}\cos\theta_t - \cos\theta_i}{\sqrt{\varepsilon_1\mu_2 / \varepsilon_2\mu_1}\cos\theta_t + \cos\theta_i}\right]^2 \cdot \left[\frac{\sqrt{\varepsilon_1\mu_2 / \varepsilon_2\mu_1}\cos\theta_i + \cos\theta_t}{\sqrt{\varepsilon_1\mu_2 / \varepsilon_2\mu_1}\cos\theta_i - \cos\theta_t}\right]^2$$

where :

$$m = \cos\{2\cot^{-1}(R_p / R_n)^{1/2}\} \qquad (3.6)$$

so :

$$m = \cos\left\{2\cot^{-1}\left[\frac{\sqrt{\varepsilon_1\mu_2 / \varepsilon_2\mu_1}\cos\theta_t - \cos\theta_i}{\sqrt{\varepsilon_1\mu_2 / \varepsilon_2\mu_1}\cos\theta_t + \cos\theta_i}\right] \cdot \left[\frac{\sqrt{\varepsilon_1\mu_2 / \varepsilon_2\mu_1}\cos\theta_i + \cos\theta_t}{\sqrt{\varepsilon_1\mu_2 / \varepsilon_2\mu_1}\cos\theta_i - \cos\theta_t}\right]\right\}$$

The above equations for m assume that the planet has a smooth dielectric surface, and that the conductivity of the surface is zero. Analytical expressions for the transmission and reflection coefficients for surfaces having non-zero conductivity or for layered surfaces (see Born and Wolf, 1970) may, of course, be inserted in equations 3.4 and 3.6.

3.2 Comparison with Observations

In order to compare the model of the degree of polarization with the data, the model has been convolved with a gaussian corresponding in width to the half power beam width of the synthesized beam. The model of the degree of polarization has been additionally modified to account for atmospheric attenuation. *e.g.*

$$m_a(\theta) = \cos 2\eta\,(\theta,\varepsilon)\,(1-\alpha(\theta))\,/\,\{(1-\alpha(\theta)^2 + \alpha(\theta)(2-\alpha(\theta))\,/\,e(\theta,\varepsilon)\} \qquad (3.7)$$

Where $\cos 2\eta$ is given by equation 3.4, $\alpha(\theta)$ is the attenuation coefficient, e is the emissivity, ε is the dielectric constant, and θ is the angle of emission.

As discussed in section 2.3, the maps of the degree of polarization were obtained by dividing the PI maps by the total intensity (TI) maps.

As can be seen from the VLA images of the degree of polarization, figures 3-2, 3-4, and 3-6, there is a great deal of azimuthal variation in the degree of polarization. These variations are due, partly, to the effects of noise. The peak polarization flux density is 0.3 mJy/beam, whereas the noise is almost 0.05 mJy/beam (see section 2.5). However, surface roughness (and atmospheric attenuation, where applicable) also may have a significant effect on the polarization intensity, and would become especially noticeable at wavelengths as short as 6 cm. This is compounded by the highest polarization occurring at large angles of transmission, where effects of surface roughness and the atmosphere are most significant.

In order to take advantage of our knowledge of the angle of linear polarization (we know that for a smooth sphere, the direction of the linear polarization is radially directed towards the center of the disk), we have measured the difference between the expected polarization angle and the measured polarization angle ($1/2\ \tan^{-1}U/Q$; see section 2.3). The cosine of this difference was multiplied with the degree of polarization. At the center of the disk, where the emission is not expected to be polarized, the measured polarization angle

should be random, while towards the limb of the planet, the measured polarization angle should correspond closely with the azimuth angle from the center of the disk. This was, in fact, found to be the case. The effect of projecting the degree of polarization along radials from the center of the disk was to reduce the noise to closer to zero mean (by half), minimizing the positive bias it has otherwise, by using our *a priori* and measured knowledge of the polarization angle. As discussed in section 2.5, there are noise biases present in the PI maps that are still present in the degree of polarization maps. In order to facilitate comparison of the model with the data, the model was adjusted by assigning a minimum value of m to the model (where we have selected $m_{min} = 0.02$, following inspection of the data), corresponding to the approximate noise bias of the degree of polarization maps.

Figures 3-3, 3-5, and 3-7 were obtained by combining the results of equation 3.7 with the observed data (projected along radials from the center). The error bars for each data point were determined by :

$$\{ [n \sum x_i^2 - (\sum x_i)^2] / [n(n-1)] \}^{1/2} / [n]^{1/2}$$

Where the x_i's are the pixel values summed at each plotted radius from the center of the disk, and n is the number of pixels summed at each radius.

For those locations at or beyond the limb of the observed emissions, dividing the polarization (PI) values by the corresponding total intensity (TI) values may produce anomalously high values for the degree of polarization. Naturally, these data do not imply peculiar properties for the surface, particularly if the points lie off the disk of the planet. Some artifacts were eliminated by setting limits within the AIPS task COMB (see section 2.3) that excluded values if the TI intensity fell below a preset amount. However, it was difficult to eliminate all of the spurious results within the limitations of the AIPS software.

3.2.1 Comparison with Observations - Mercury Data

Figure 3-2 is a plot of the degree of polarization (PI / TI) of the radio emissions from the surface of Mercury, at a wavelength of 6 cm. Figure 3-3 displays the result of plotting the theoretical degree of polarization *versus* angular distance from the center of Mercury's disk (which is related to the angle of transmission by the law of sines), for various dielectric constants (ε = 2.0, 2.25, 2.5, and 2.75). The average values of the observed λ = 6 cm degree of polarization at a given angular distance from the center of the disk are plotted, as well as the error bars calculated from the distribution of values at each radius. (See section 3.2).

We find good agreement with the data and the theory at distances greater that about 2.5 arseconds from the center of the disk ($\theta_t = 25^\circ$) . At radial distances less than 2.5 arcseconds, the degree of polarization is not larger than the noise (see table 3-6). The data at distances greater than 2.5 arcseconds from the planet's center are consistent with a dielectric constant of 2.1 ± 0.2 . This is in fair agreement with the value obtained by Cuzzi (1973) of 2.4 ± 0.3, but is lower than the radar value of 2.9 (Pettengill, 1978). See section 3.3 for a discussion. Table 3-1 shows a compilation of the averaged degree of polarization values, where the maximum, minimum, and mean m's (and standard deviation of the tabulated average), along with their associated radial distances (in pixels), angular distances, and angles of transmission are tabulated with respect to the center of the disk. Also listed are the number of pixels and the number of resolution elements (where each resolution element is 0.5 arcseconds) associated with each radius.

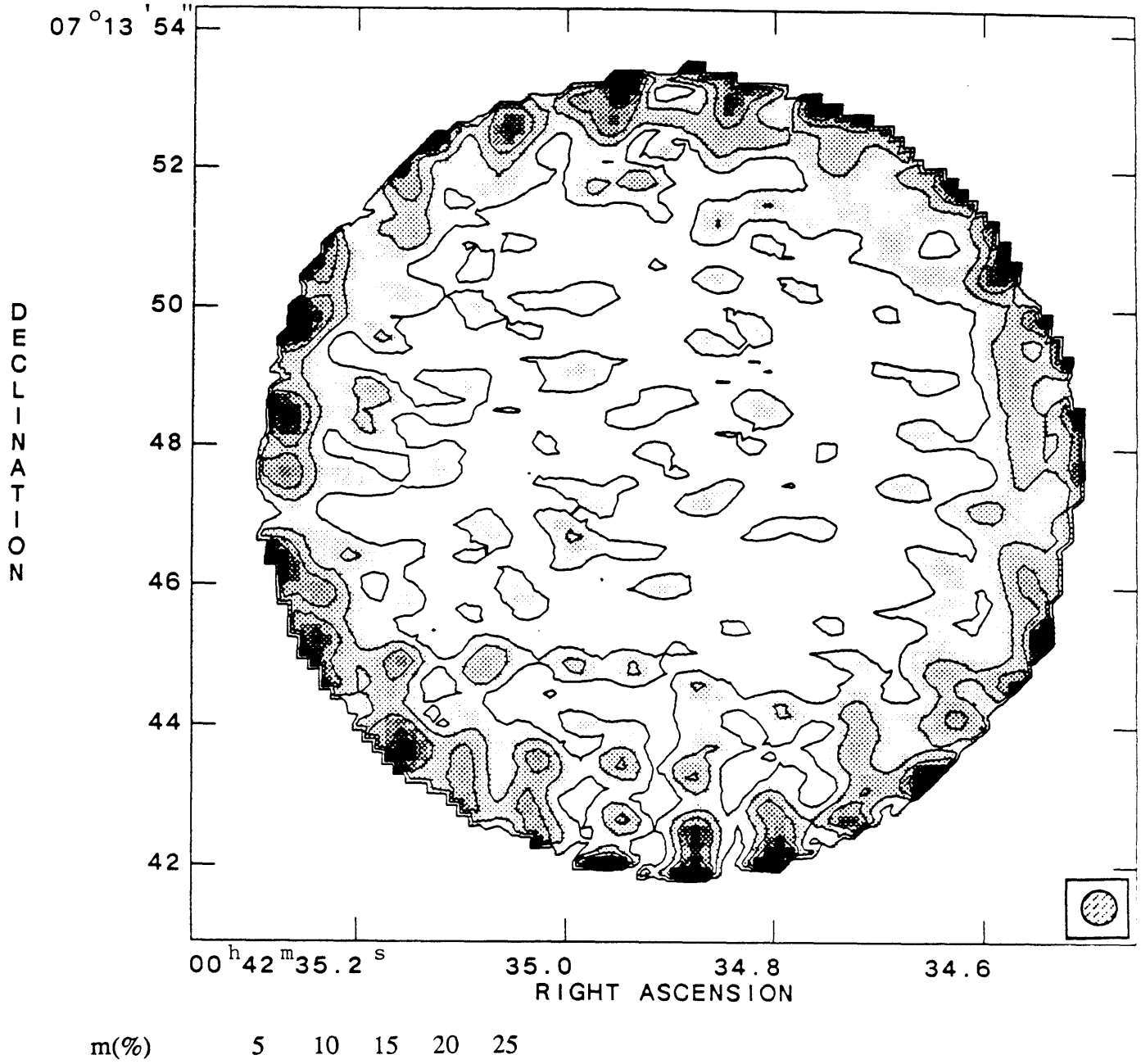


Figure 3-2
Contour-grey scale plot of the degree of polarization (m) of the emissions from the surface of Mercury on April 5, 1985 at $\lambda = 6$ cm

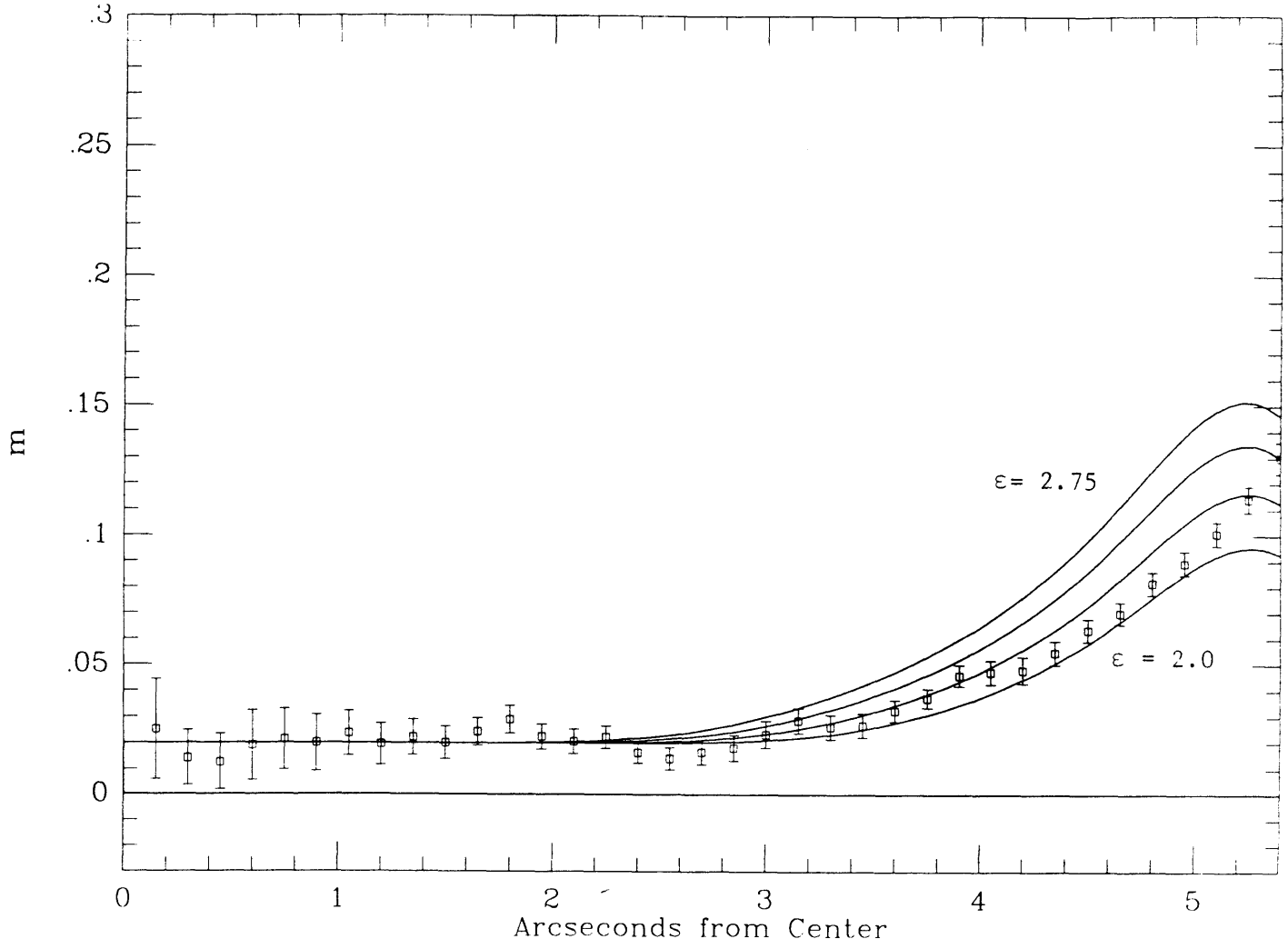


Figure 3-3
The degree of polarization (m) *versus* arcseconds from the center of the disk for the April 5, 1985 λ = 6 cm Mercury dataset. Theoretical curves for the expected m (convolved with a gaussian corresponding to the resolution) for dielectric constants of 2, 2.25, 2.5, and 2.75 have also been drawn.

Table 3-1

Mercury April 5, 1985 $\lambda = 6$ cm degree of polarization

distance from center of disk			Circumference		the degree of polarization			
pixels	arcseconds	θ_t (deg)	pixels	resolution cells	m_{max}	m_{min}	m_{avg}	s.d. of m_{avg}
1	0.150	1.492	8	1.88	0.0509	-0.0233	0.0251	0.0193
2	0.300	2.986	16	3.77	0.0465	-0.0178	0.0141	0.0106
3	0.450	4.481	20	5.65	0.0784	-0.0273	0.0126	0.0108
4	0.600	5.979	24	7.54	0.0995	-0.0421	0.0189	0.0134
5	0.750	7.482	40	9.42	0.0975	-0.0467	0.0213	0.0116
6	0.900	8.990	36	11.31	0.0748	-0.0483	0.0200	0.0107
7	1.050	10.504	48	13.19	0.0719	-0.0537	0.0236	0.0085
8	1.200	12.025	56	15.08	0.0800	-0.0544	0.0195	0.0079
9	1.350	13.555	56	16.96	0.0898	-0.0435	0.0221	0.0067
10	1.500	15.095	68	18.85	0.0907	-0.0259	0.0201	0.0061
11	1.650	16.647	64	20.73	0.0771	-0.0178	0.0242	0.0052
12	1.800	18.211	80	22.62	0.0899	-0.0250	0.0289	0.0053
13	1.950	19.789	92	24.50	0.0636	-0.0517	0.0224	0.0048

Table 3-1 (Continued)

Mercury April 5, 1985 $\lambda = 6$ cm degree of polarization

distance from center of disk			Circumference		the degree of polarization			
pixels	arcseconds	θ_t (deg)	pixels	resolution cells	m_{max}	m_{min}	m_{avg}	s.d. of m_{avg}
14	2.100	21.383	88	26.39	0.0642	-0.0591	0.0205	0.0047
15	2.250	22.994	96	28.27	0.0661	-0.0615	0.0222	0.0042
16	2.400	24.625	96	30.16	0.0530	-0.0506	0.0164	0.0038
17	2.550	26.278	116	32.04	0.0647	-0.0413	0.0141	0.0041
18	2.700	27.954	120	33.93	0.0796	-0.0409	0.0166	0.0046
19	2.850	29.657	120	35.81	0.1043	-0.0530	0.0183	0.0048
20	3.000	31.389	124	37.70	0.1076	-0.0513	0.0234	0.0051
21	3.150	33.154	144	39.58	0.1104	-0.0662	0.0287	0.0048
22	3.300	34.955	136	41.47	0.0979	-0.0748	0.0262	0.0047
23	3.450	36.797	140	43.35	0.1027	-0.0685	0.0268	0.0046
24	3.600	38.684	152	45.24	0.1220	-0.0658	0.0325	0.0042
25	3.750	40.622	168	47.12	0.1316	-0.0467	0.0374	0.0037
26	3.900	42.618	176	49.01	0.1477	-0.0412	0.0461	0.0041

Table 3-1 (Continued)

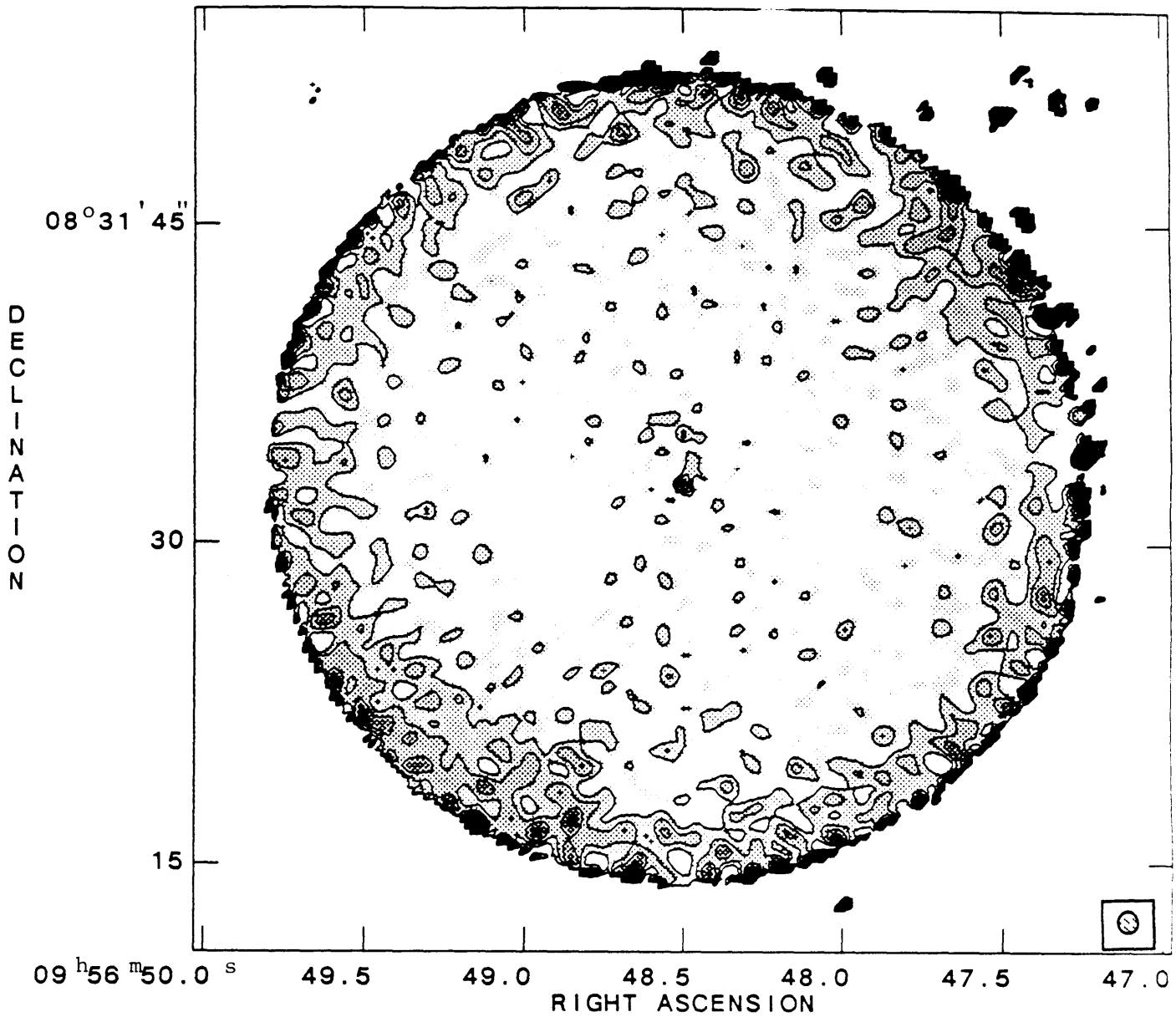
Mercury April 5, 1985 $\lambda = 6$ cm degree of polarization

distance from center of disk			Circumference		the degree of polarization			
pixels	arcseconds	θ_t (deg)	pixels	resolution cells	m_{max}	m_{min}	m_{avg}	s.d. of m_{avg}
27	4.050	44.680	164	50.89	0.1445	-0.0533	0.0474	0.0046
28	4.200	46.819	168	52.78	0.1493	-0.0990	0.0482	0.0051
29	4.350	49.046	192	54.66	0.1589	-0.0767	0.0549	0.0046
30	4.500	51.377	188	56.55	0.1814	-0.0498	0.0636	0.0043
31	4.650	53.835	208	58.43	0.1669	-0.0492	0.0701	0.0043
32	4.800	56.445	200	60.32	0.1878	0.0000	0.0816	0.0045
33	4.950	59.250	208	62.20	0.1974	0.0079	0.0894	0.0046
34	5.100	62.306	228	64.09	0.2071	0.0000	0.1007	0.0046
35	5.250	65.712	208	65.97	0.2376	0.0372	0.1140	0.0051
36	5.400	69.641	232	67.86	0.3098	0.0000	0.1300	0.0061
37	5.550	74.488	228	69.74	0.3869	-0.0791	0.1338	0.0083
38	5.700	81.736	256	71.63	0.4045	-0.3236	0.0881	0.0124

3.2.2 Comparison with Observations - Venus Data

Figures 3-4 and 3-6 are contour grey scale plots of the degree of polarization observed for Venus on October 3 and November 12, 1983, at a wavelength of 20cm. As expected, the polarization increases steadily towards the limb of the planet. However, there are significant azimuthal variations as a result of the low signal to noise ratio and possible surface roughness and atmospheric effects. We see in figure 3-4, for example, that, at the location of Aphrodite on the limb of the planet, the degree of polarization is significantly reduced. This may be a result of the surface roughness known to exist in that region. As discussed in section 3.2.1, the large values of the degree of polarization occurring beyond the physical extent of the planet should be ignored, as they do not represent anything of physical significance, and are the result of the division by small values in the regions of the TI map outside of the disk of the planet.

Figure 3-5 is a plot of the degree of polarization (m) versus angular distance from the center of the disk, along with error bars representing the range of values found azimuthally (see section 3.2), at 0.25 arcsecond increments in the angular distance from the center. Also plotted are theoretical curves for dielectric constants starting at 2, and incremented by 0.25 up to $\varepsilon = 4$. As can be seen, the average m does not exceed the noise until approximately 8 arcseconds from the center of the disk. See table 3-2 for a detailed description of the polarization values found. The resolution is one arcsecond. Close to the center of the disk (between 8 and 12 arcseconds) the degree of polarization indicates values of ε of about 4 (where, however, the signal to noise ratio is small), while towards the limb of the planet, the indicated dielectric constant steadily decreases to about 2.2 . This must result from some unmodeled effect, probably associated with the surface roughness.



m(%) 10 15 20 25 30

Figure 3-4
Contour-grey scale plot of the degree of polarization (m) of the emissions from the surface of Venus on October 3, 1983 at λ = 20 cm

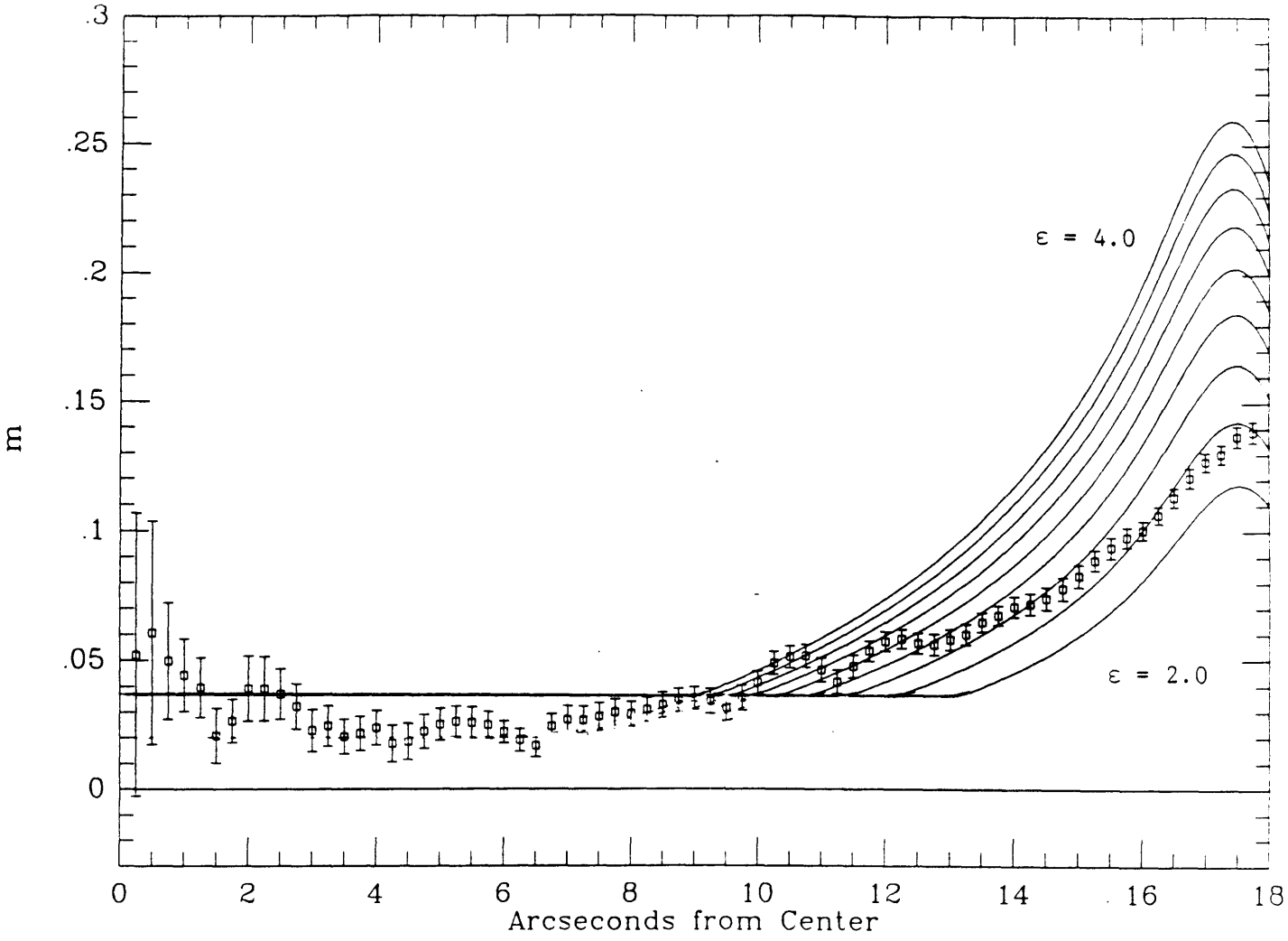


Figure 3-5
The degree of polarization (m) *versus* arcseconds from the center of the disk for the October 3, 1985 λ = 20 cm Venus dataset. Theoretical curves for the expected m (convolved with a gaussian corresponding to the resolution) for dielectric constants of 2.00, 2.25, 2.50, 2.75, 3.00, 3.25, 3.5, 3.75 and 4.00 have also been drawn.

Table 3-2

Venus October 3 1983 $\lambda = 20$ cm degree of polarization

distance from center of disk			Circumference		the degree of polarization			
pixels	arcseconds	θ_t (deg)	pixels	resolution cells	m_{max}	m_{min}	m_{avg}	s.d. of m_{avg}
1	0.250	0.769	8	1.57	0.2033	0.0000	0.0520	0.0547
2	0.500	1.537	16	3.14	0.2418	-0.0060	0.0605	0.0430
3	0.750	2.306	20	4.71	0.1867	-0.0096	0.0497	0.0225
4	1.000	3.076	24	6.28	0.1152	-0.0068	0.0443	0.0140
5	1.250	3.846	40	7.85	0.0987	-0.0549	0.0394	0.0116
6	1.500	4.617	36	9.42	0.0784	-0.0698	0.0208	0.0106
7	1.750	5.388	48	11.00	0.0924	-0.0494	0.0265	0.0084
8	2.000	6.161	56	12.57	0.1542	-0.0561	0.0391	0.0126
9	2.250	6.934	56	14.14	0.1513	-0.0605	0.0391	0.0124
10	2.500	7.709	68	15.71	0.1152	-0.0507	0.0370	0.0098
11	2.750	8.486	64	17.28	0.1185	-0.0468	0.0322	0.0088
12	3.000	9.264	80	18.85	0.1053	-0.0470	0.0228	0.0081
13	3.250	10.043	92	20.42	0.0987	-0.0684	0.0245	0.0078
14	3.500	10.825	88	21.99	0.0922	-0.0839	0.0204	0.0067
15	3.750	11.608	96	23.56	0.0922	-0.0959	0.0216	0.0066

Table 3-2 (Continued)
Venus October 3 1983 $\lambda = 20$ cm degree of polarization

distance from center of disk			Circumference		the degree of polarization			
pixels	arcseconds	θ_t (deg)	pixels	resolution cells	m_{max}	m_{min}	m_{avg}	s.d. of m_{avg}
16	4.000	12.394	96	25.13	0.1251	-0.0595	0.0239	0.0067
17	4.250	13.182	116	26.70	0.1382	-0.0934	0.0178	0.0071
18	4.500	13.973	120	28.27	0.1185	-0.0787	0.0185	0.0070
19	4.750	14.767	120	29.85	0.1284	-0.0889	0.0224	0.0066
20	5.000	15.563	124	31.42	0.1218	-0.0849	0.0251	0.0062
21	5.250	16.362	144	32.99	0.1218	-0.0857	0.0262	0.0059
22	5.500	17.165	136	34.56	0.1317	-0.0768	0.0258	0.0060
23	5.750	17.971	140	36.13	0.1053	-0.0589	0.0249	0.0052
24	6.000	18.781	152	37.70	0.0691	-0.0569	0.0222	0.0043
25	6.250	19.595	168	39.27	0.0823	-0.0591	0.0190	0.0044
26	6.500	20.413	176	40.84	0.0889	-0.0511	0.0169	0.0044
27	6.750	21.235	164	42.41	0.1020	-0.0439	0.0243	0.0050
28	7.000	22.062	168	43.98	0.1251	-0.0525	0.0269	0.0055
29	7.250	22.894	192	45.55	0.1350	-0.0528	0.0268	0.0054
30	7.500	23.731	188	47.12	0.1284	-0.0581	0.0282	0.0053

Table 3-2 (Continued)
Venus October 3 1983 λ = 20 cm degree of polarization

distance from center of disk			Circumference		the degree of polarization			
pixels	arcseconds	θ_t (deg)	pixels	resolution cells	m_{max}	m_{min}	m_{avg}	s.d. of m_{avg}
31	7.750	24.573	208	48.69	0.1185	-0.0607	0.0300	0.0051
32	8.000	25.421	200	50.27	0.1448	-0.0777	0.0292	0.0049
33	8.250	26.276	208	51.84	0.1350	-0.0792	0.0310	0.0048
34	8.500	27.136	228	53.41	0.1152	-0.0765	0.0328	0.0050
35	8.750	28.003	208	54.98	0.1185	-0.0446	0.0346	0.0046
36	9.000	28.877	232	56.55	0.1382	-0.0553	0.0354	0.0044
37	9.250	29.759	228	58.12	0.1613	-0.0620	0.0343	0.0046
38	9.500	30.648	256	59.69	0.1448	-0.0852	0.0315	0.0049
39	9.750	31.546	248	61.26	0.1251	-0.1051	0.0356	0.0049
40	10.000	32.452	236	62.83	0.1350	-0.1136	0.0415	0.0049
41	10.250	33.367	272	64.40	0.1350	-0.0908	0.0491	0.0044
42	10.500	34.293	264	65.97	0.1547	-0.0841	0.0514	0.0044
43	10.750	35.228	288	67.54	0.1415	-0.0985	0.0518	0.0043
44	11.000	36.175	276	69.12	0.1514	-0.0607	0.0465	0.0043
45	11.250	37.133	272	70.69	0.1481	-0.0904	0.0418	0.0046

Table 3-2 (Continued)

Venus October 3 1983 λ = 20 cm degree of polarization

distance from center of disk			Circumference		the degree of polarization			
pixels	arcseconds	θ_t (deg)	pixels	resolution cells	m_{max}	m_{min}	m_{avg}	s.d. of m_{avg}
46	11.500	38.103	296	72.26	0.1415	-0.0798	0.0478	0.0043
47	11.750	39.087	292	73.83	0.1382	-0.0803	0.0537	0.0039
48	12.000	40.084	312	75.40	0.1382	-0.0616	0.0574	0.0037
49	12.250	41.096	304	76.97	0.1415	-0.0693	0.0584	0.0037
50	12.500	42.124	336	78.54	0.1317	-0.0642	0.0566	0.0040
51	12.750	43.169	324	80.11	0.1580	-0.0567	0.0562	0.0041
52	13.000	44.232	312	81.68	0.1382	-0.0694	0.0580	0.0040
53	13.250	45.315	344	83.25	0.1481	-0.0866	0.0601	0.0040
54	13.500	46.419	324	84.82	0.1777	-0.0917	0.0649	0.0038
55	13.750	47.546	376	86.39	0.1876	-0.0868	0.0675	0.0037
56	14.000	48.697	344	87.96	0.1580	-0.0826	0.0709	0.0040
57	14.250	49.875	360	89.54	0.1777	-0.0934	0.0719	0.0042
58	14.500	51.083	364	91.11	0.1810	-0.0767	0.0742	0.0043
59	14.750	52.323	368	92.68	0.1909	-0.0676	0.0780	0.0044
60	15.000	53.599	392	94.25	0.2008	-0.0809	0.0829	0.0043

Table 3-2 (Continued)
Venus October 3 1983 λ = 20 cm degree of polarization

distance from center of disk			Circumference		the degree of polarization			
pixels	arcseconds	θ_t (deg)	pixels	resolution cells	m_{max}	m_{min}	m_{avg}	s.d. of m_{avg}
61	15.250	54.915	388	95.82	0.1909	-0.0825	0.0890	0.0039
62	15.500	56.276	392	97.39	0.2041	-0.0975	0.0938	0.0041
63	15.750	57.686	400	98.96	0.2403	-0.1007	0.0978	0.0038
64	16.000	59.154	388	100.53	0.2699	-0.0614	0.1005	0.0035
65	16.250	60.687	432	102.10	0.2666	0.0150	0.1064	0.0033
66	16.500	62.298	400	103.67	0.2436	0.0000	0.1133	0.0037
67	16.750	64.000	424	105.24	0.2304	0.0230	0.1209	0.0038
68	17.000	65.812	452	106.81	0.2666	0.0416	0.1273	0.0036
69	17.250	67.762	416	108.38	0.2666	-0.0823	0.1303	0.0037
70	17.500	69.890	448	109.96	0.2798	-0.0893	0.1371	0.0040
71	17.750	72.260	428	111.53	0.3226	0.0254	0.1389	0.0041

Figure 3-6, likewise, is a contour-grey scale map of the degree of polarization of Venus observed on November 12, 1983. Again, we see the tendency for the polarized emission to increase towards the limb of the planet. We also see significant variations of the degree of polarization depending on location. For example, an area to the South, and an area to the Northeast, display unusually low values of m. Figure 3-7 plots the result of azimuthal averaging of the degree of polarizations at 0.3 arcsecond increments, as in figure 3-5. Beyond 4 arcseconds, the polarization values begin to rise above the noise. Also plotted are theoretical predictions of the degree of polarization for ε's of 2, 2.5, 3, and 3.5. We note that Aphrodite extends some 5 arcseconds from the center of the disk. A dielectric constant of 2.5 ± 0.5 is indicated more than 5 arcseconds from the center of the disk. Table 3-3 tabulates the observed m's, as in tables 3-1 and 3-2, except that each resolution element now extends over 1.1 arcseconds.

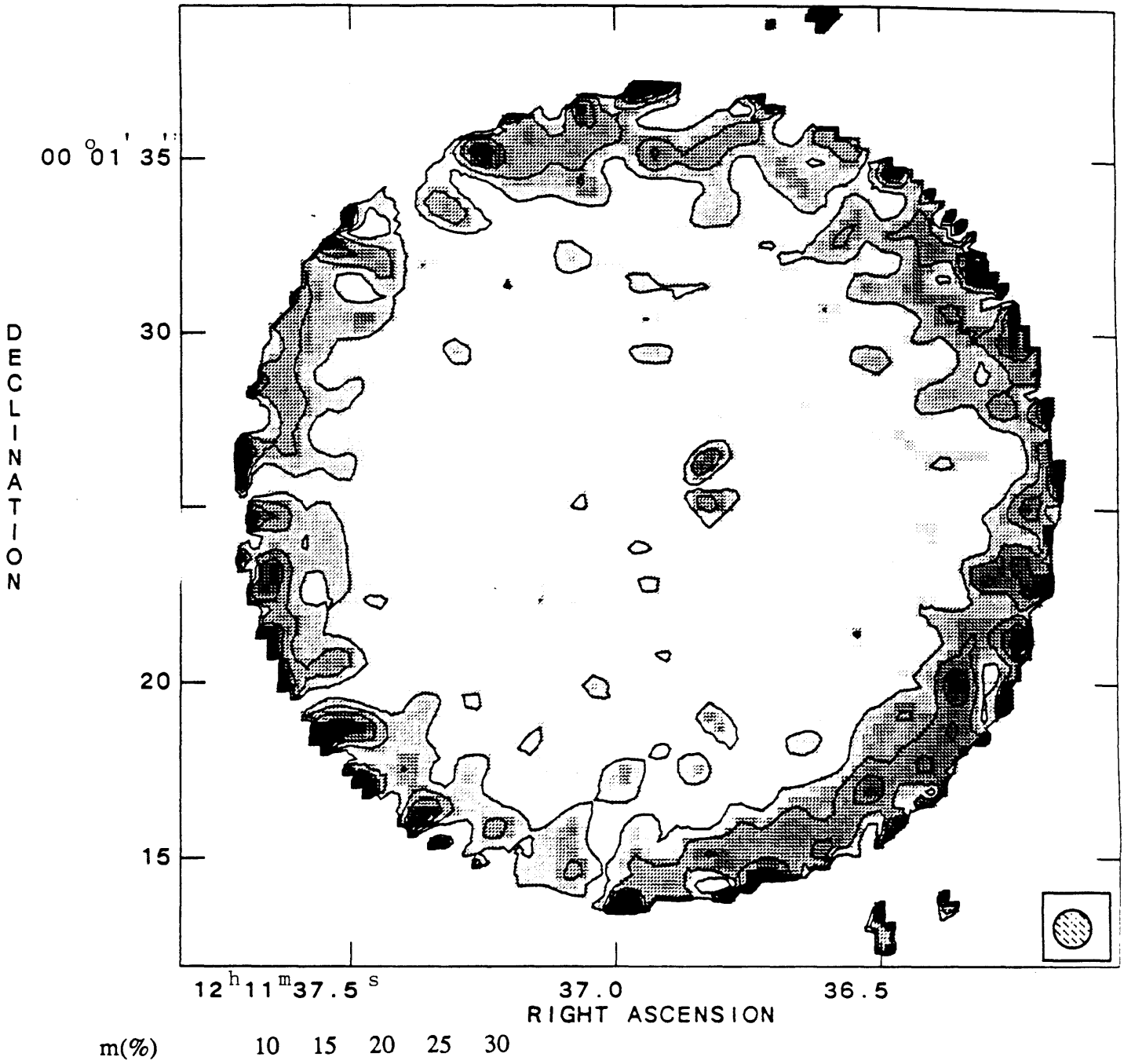


Figure 3-6
Contour-grey scale plot of the degree of polarization (m) of the emissions from the surface of Venus on November 12, 1985 at λ = 20 cm

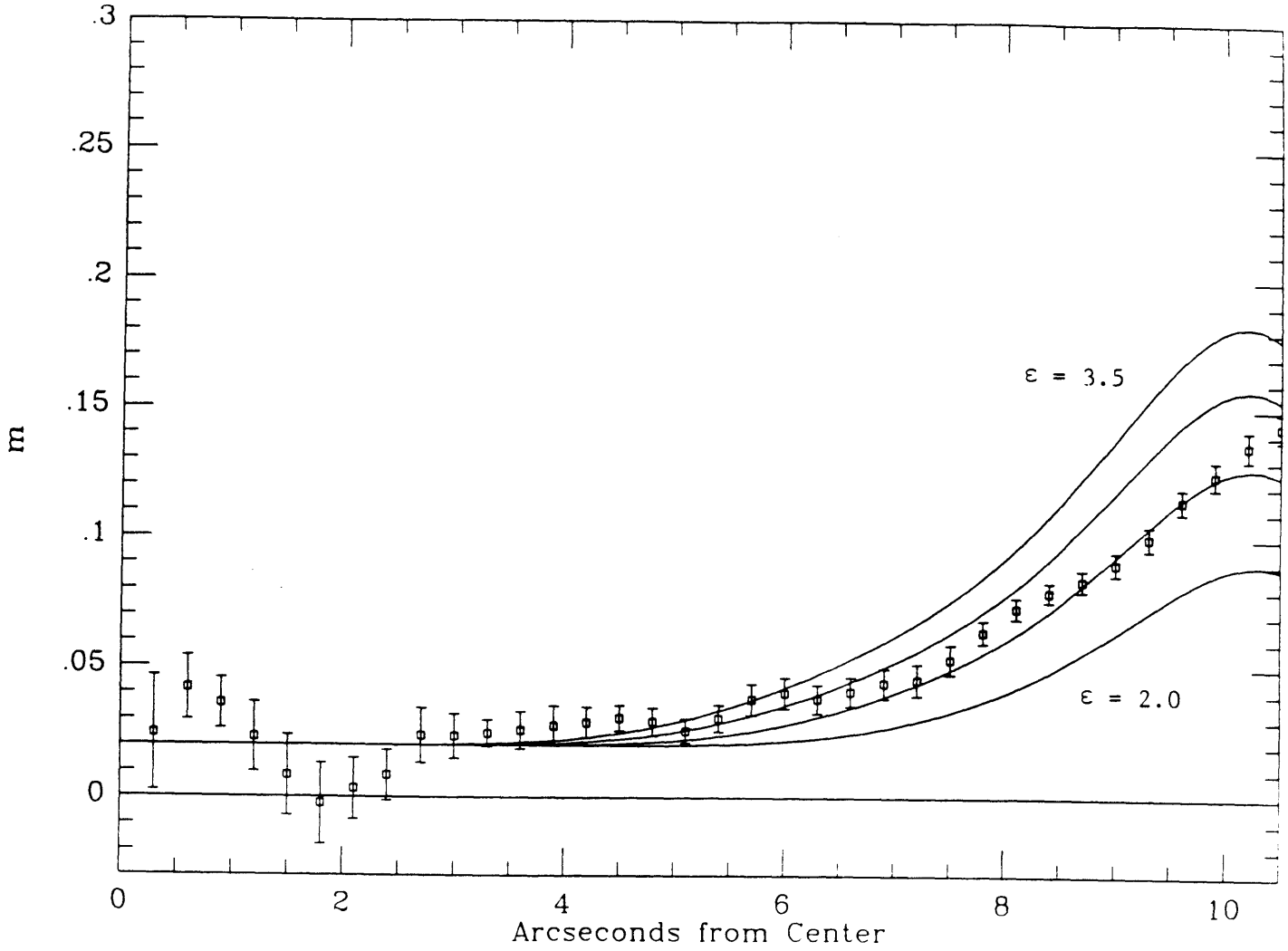


Figure 3-7
The degree of polarization (m) *versus* arcseconds from the center of the disk for the November 12, 1985 λ = 20 cm Venus dataset. Theoretical curves for the expected m (convolved with a gaussian corresponding to the resolution) for dielectric constants of 2, 2.5, 3, and 3.5 have also been drawn.

Table 3-3

Venus November 12, 1983 $\lambda = 20$ cm degree of polarization

distance from center of disk			Circumference		the degree of polarization			
pixels	arcseconds	θ_t (deg)	pixels	resolution cells	m_{max}	m_{min}	m_{avg}	s.d. of m_{avg}
1	0.300	1.520	8	1.71	0.0608	-0.0184	0.0244	0.0220
2	0.600	3.041	16	3.43	0.0738	0.0014	0.0418	0.0122
3	0.900	4.564	20	5.14	0.0701	-0.0100	0.0359	0.0097
4	1.200	6.090	24	6.85	0.1125	-0.0301	0.0230	0.0133
5	1.500	7.620	40	8.57	0.1545	-0.1331	0.0084	0.0154
6	1.800	9.156	36	10.28	0.0639	-0.1489	-0.0024	0.0155
7	2.100	10.699	48	12.00	0.0758	-0.1213	0.0033	0.0117
8	2.400	12.250	56	13.71	0.0772	-0.1005	0.0084	0.0097
9	2.700	13.810	56	15.42	0.1018	-0.0762	0.0237	0.0105
10	3.000	15.380	68	17.14	0.0932	-0.0513	0.0235	0.0085
11	3.300	16.962	64	18.85	0.0712	-0.0335	0.0246	0.0051
12	3.600	18.558	80	20.56	0.1196	-0.0532	0.0257	0.0071

Table 3-3 (Continued)

Venus November 12, 1983 λ = 20 cm degree of polarization

distance from center of disk			Circumference		the degree of polarization			
pixels	arcseconds	θ_t (deg)	pixels	resolution cells	m_{max}	m_{min}	m_{avg}	s.d. of m_{avg}
13	3.900	20.169	92	22.28	0.1336	-0.0495	0.0275	0.0077
14	4.200	21.796	88	23.99	0.0862	-0.0451	0.0289	0.0058
15	4.500	23.442	96	25.70	0.0809	-0.0294	0.0306	0.0049
16	4.800	25.109	96	27.42	0.1090	-0.0244	0.0292	0.0053
17	5.100	26.800	116	29.13	0.1002	-0.0191	0.0256	0.0046
18	5.400	28.515	120	30.84	0.0967	-0.0300	0.0305	0.0051
19	5.700	30.259	120	32.56	0.1319	-0.0388	0.0379	0.0060
20	6.000	32.035	124	34.27	0.1178	-0.0443	0.0403	0.0059
21	6.300	33.846	144	35.99	0.1231	-0.0618	0.0380	0.0054
22	6.600	35.696	136	37.70	0.1477	-0.0559	0.0409	0.0056
23	6.900	37.590	140	39.41	0.1424	-0.0520	0.0442	0.0057
24	7.200	39.533	152	41.13	0.1410	-0.0585	0.0455	0.0061
25	7.500	41.532	168	42.84	0.1336	-0.0633	0.0534	0.0057
26	7.800	43.596	176	44.55	0.1371	-0.0398	0.0640	0.0044

Table 3-3 (Continued)

Venus November 12, 1983 $\lambda = 20$ cm degree of polarization

distance from center of disk			Circumference		the degree of polarization			
pixels	arcseconds	θ_t (deg)	pixels	resolution cells	m_{max}	m_{min}	m_{avg}	s.d. of m_{avg}
27	8.100	45.732	164	46.27	0.1530	0.0000	0.0732	0.0041
28	8.400	47.954	168	47.98	0.1565	0.0141	0.0795	0.0038
29	8.700	50.276	192	49.69	0.1688	-0.0383	0.0840	0.0041
30	9.000	52.717	188	51.41	0.1987	-0.0441	0.0906	0.0044
31	9.300	55.303	208	53.12	0.2321	-0.0449	0.1004	0.0046
32	9.600	58.070	200	54.84	0.2461	-0.0471	0.1149	0.0047
33	9.900	61.071	208	56.55	0.2374	-0.1188	0.1250	0.0053
34	10.200	64.388	228	58.26	0.2708	-0.1525	0.1364	0.0058
35	10.500	68.165	208	59.98	0.3639	0.0615	0.1438	0.0054
36	10.800	72.704	232	61.69	0.3499	-0.1643	0.1433	0.0071
37	11.100	78.904	228	63.40	0.3710	-0.1683	0.1371	0.0100

3.3 Discussion of Results

As can be seen, at angles of transmission greater than about 30 to 40 degrees, the average polarization values of Mercury and Venus begin to exceed the noise. As discussed in section 2.5, there is a positive noise bias to the polarization intensity arising from the absence of negative values and the presence of map artifacts. However, in analogy with FM reception, we expect that when the signal rises above the noise (which is approximately 2%), the signal should dominate. The Mercury and Venus data follow the theoretical curves fairly well at angles of transmission greater than 30 to 40 degrees. However, both the Venus and Mercury polarization results indicate dielectric constants significantly less than that found *via* radar observations (as has been noted previously by others : Muhleman, Orton, and Berge, 1979; Cuzzi, 1974; for the Moon , Hagfors, 1970) or from the radio emissivity (see section 4.3). This may be a result of an increase in the surface roughness noticible on a scale less than the wavelength of the observations that would introduce a diffusely scattered component to the emissions, reducing the degree of polarization. Note the particularly low degree of polarization of the Venus λ = 6 cm observations (see figure 2-28) and of the Mercury λ = 2 cm observations (see figure 2-30). The signal to noise should also be considered, as it prevents us from measuring the polarization values at small angles of transmission where the degree of polarization is also the smallest.

In addition, particularly evident in figure 3-5 is the tendency for the Venus data to decrease relative to the model curves for increasing angles of transmission. At large angles of emission, the atmosphere may increasingly reduce the degree of polarization values. For example, unpolarized thermal emission refracted near the limb of the planet would reduce the degree of polarization; or an atmospheric layer of absorbing gases would increasingly effect the degree of polarization of the emission near the limb. A simple correction for the atmospheric attenuation, however, does not explain the decreasing values of ε. Mercury, which has a negligible atmosphere, would, naturally, not be affected in this way. One possible explanation of the results is that, at large angles of transmission, the emissions are

originating from a shallower depth where we expect that the surface material would be looser and less dense than at greater depths. This surface material would be expected to have a smaller dielectric constant than the rocks underlying it. The radar measurements at small angles of incidence would reflect the denser layer, while the radio emissions would likewise originate from greater depth.

As the angle of emission increases, even mild surface undulations will tend to confuse the angle of emission. At angles of emission greater than 70 degrees, this may well be a dominant factor for both the Venus and Mercury observations, but is particularly a problem for Mercury, as the wavelength of our observations is shorter than those used for Venus, and surface roughness might be expected to be more important. It should be noted that some locations of the surface are smoother than others, and if surface roughness is playing an important role at values of θ_t less than 70 degrees, then values of m that exceed the average may, indeed, accurately reflect the dielectric constant of those locations. The dielectric constant of Venus indicated by the maximum values of the degree of polarization exceed 7 at angles of transmission from θ_t = 40 to 70 degrees.

The absence of a significant amount of polarization near the limb of the Venus disk at λ = 6 cm indicates that surface roughness and atmospheric attenuation of the emissions has a pronounced effect on the polarization at that wavelength. The almost complete absence of polarized flux from Mercury at λ = 2 cm leads one to suspect that there is a substantial increase in the apparent surface roughness at this wavelength, as compared to the surface roughness as λ=6 cm.

Chapter 4. Deduced Results

4.1 Emissivity of the Venus surface

The thermal profile of the atmosphere of Venus was measured by the Pioneer Venus atmospheric probes. Because of the nearly adiabatic nature of the atmosphere, we may associate these temperature measurements with the physical temperature of the surface at the corresponding altitudes. The temperatures adopted for this analysis are from the Pioneer Venus day probe (Seiff et al, 1980) :

km above surface	physical temperature K
0	734
1	726
2	719
3	712
4	705
5	697
6	689
7	683
8	677
9	669
10	661
11	654

For reference, figure 4-1 is a topographic map of the surface of Venus obtained by the Pioneer Venus radar altimeter. Radio observations of the brightness temperature of the Venus surface may then be used to obtain estimates of the emissivity (Ford and Pettengill, 1983). We have :

$$T_B = (1 - \alpha) \{ e\, T_P + (1 - e) [\ \alpha\, T_{atm} + (1 - \alpha)\, T_S\ ] \} + \alpha T_{atm} \qquad (4.1)$$

where T_B is the measured radio brightness temperature, T_P is the Pioneer Venus measurements that we associate with the physical temperature of the surface, T_{atm} is the physical temperature of the atmosphere where the interaction between the radio waves and the atmosphere effectively occurs, T_S is the sky brightness temperature ($T_S \approx$ 4K), e is the emissivity of the surface, and α is the one way atmospheric attenuation of the radio

emissions at normal incidence and at mean surface altitude ($\alpha \approx 1 - e^{-15/\lambda^2}$, where λ is in cm ; Ford and Pettengill, 1983).

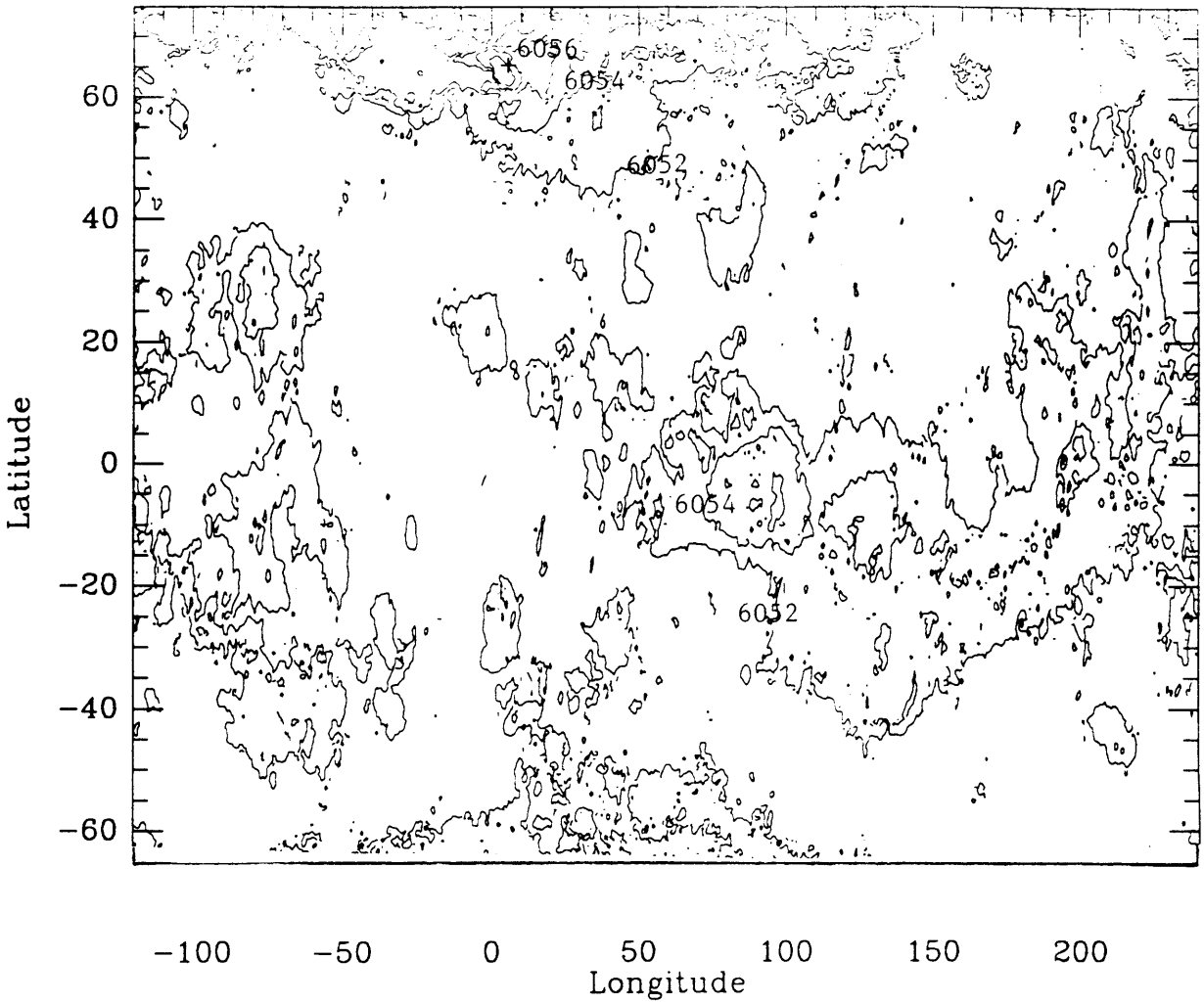


Figure 4-1

Topograpic map of Venus from Pioneer Venus radar altimeter

(Pettengill et al, 1980)

4.1.1 λ = 20 cm observations

At a wavelength of 20 cm, the atmosphere is relatively transparent (α = 0.037), $(1-\alpha)T_S$ is small compared with αT_{atm}, and $T_{atm} \approx T_P$. We find that :

$$e = [T_B / T_P - \alpha(2 - \alpha)]/(1 - \alpha)^2 \qquad (4.2)$$

or :

$$e = 1.078\ T_B/T_P - 0.0778 \qquad \text{at } \lambda = 20 \text{ cm} \qquad (4.3)$$

Given the physical temperature measured for the surface, we may then obtain the emissivity directly from the radio brightness temperature.

The mean T_B obtained from the visibility function of October 3, 1983 is 623 K ± 28 K. For a T_p = 734 K, this indicates an emissivity of 0.84 ± 0.03. The mean T_B obtained from the visibility function of November 12, 1983 is 615 K ± 45 K, which from equation 4.3 indicates an emissivity of 0.83 ± 0.06, for a T_p = 734 K. Figures 4-2 and 4-3 are plots of the emissivity as a function of azimuth, counterclockwise from South, for Venus on the two observation dates (October 3 and November 12, 1983, respectively), and were obtained from the brightness temperature figures 2-10 and 2-14, respectively (discussed in section 2.4.2.1), *via* equation 4.3, figure 4-1, and the table of physical temperatures versus altitude in section 4.1. Emissivities as low as 0.56 ± 0.05 at an azimuth of 205 degrees are reached on the October 3 orientation (see figure 4-2). This low emissivity region coincides with the location of Maxwell Montes, where the reflectivity reaches 0.4 (Pettengill, Ford, and Nozette, 1982). At the same orientation, the emissivity of the Aphrodite region lying on the limb of the planet reached as low as 0.62 ± 0.05 . This measurement at such a high angle of emission may be affected by the surface roughness associated with this area, and is poorly resolved. The Pioneer Venus radiometer (Ford and

Pettengill, 1983) determination of the emissivity indicated emissivities as low as 0.54 in the highland areas. Emissivities as low as 0.62 ± 0.07 are reached on the November 12, 1983 observation of Venus. See Figure 4-3. The emissivity is lower at Ovda than at Thetis, where the minimum emissivity is 0.70 ± 0.07. Thetis is not completely resolved, however, which may explain its higher emissivity.

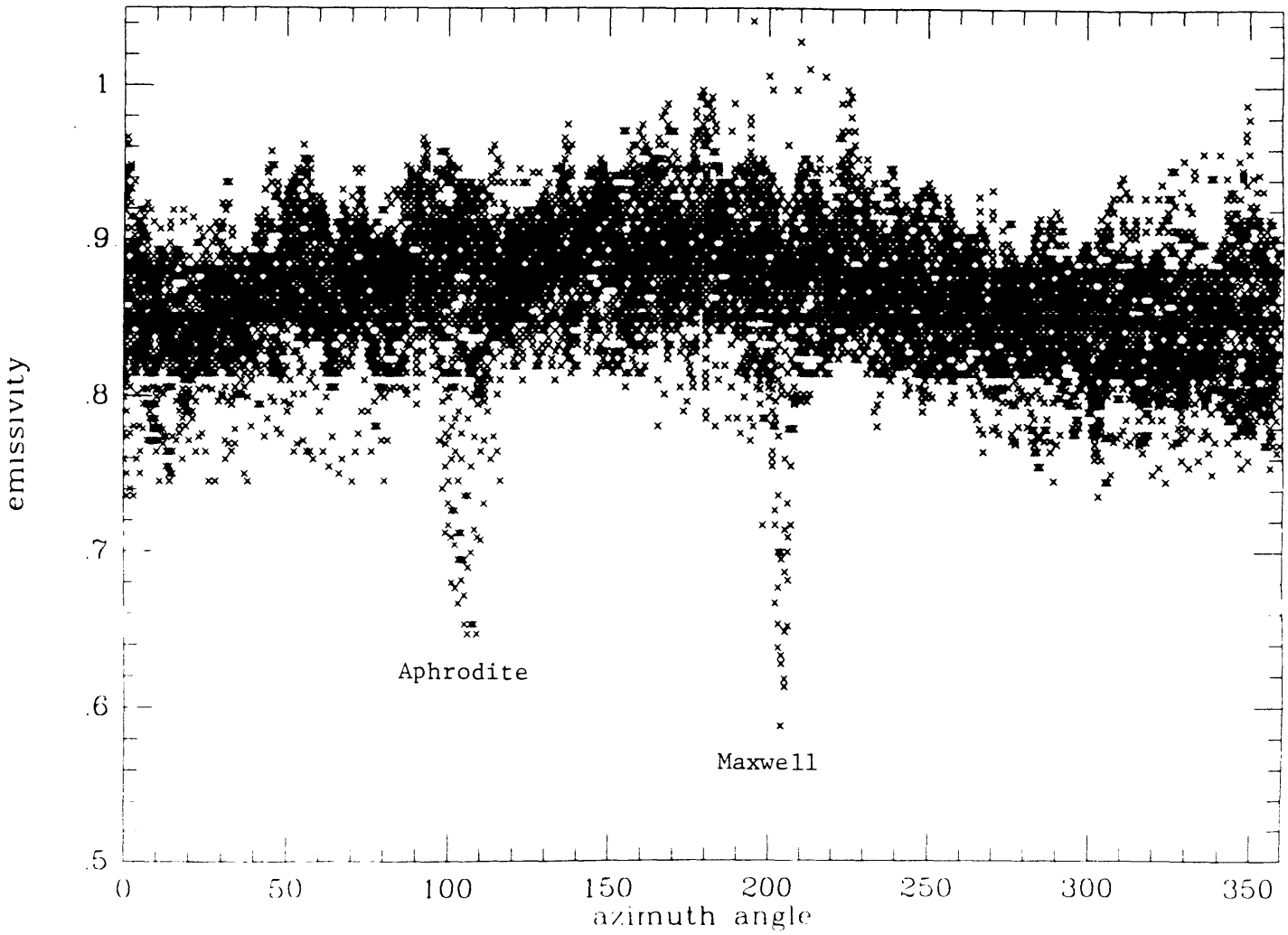


Figure 4-2
Emissivity *versus* azimuth angle measured counterclockwise starting from South for Venus October 3, 1983 λ = 20 cm data .

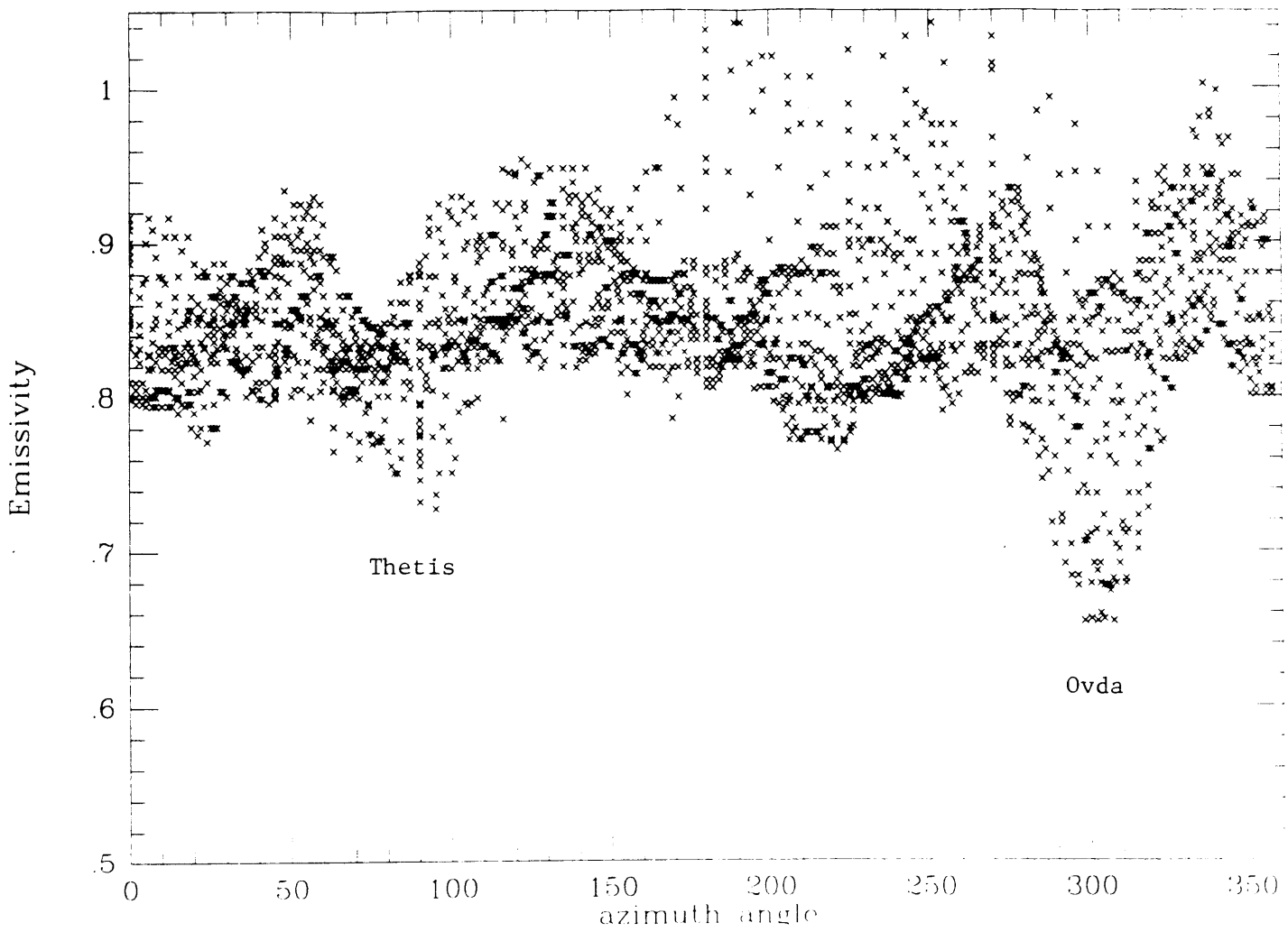


Figure 4-3
Emissivity *versus* azimuth angle measured counterclockwise starting from South for Venus November 12, 1983 λ = 20 cm data .

4.1.2 λ = 6 cm observations

At a wavelength of 6 cm, where attenuation by the atmosphere of Venus is greater than at λ = 20 cm, α is not well known. Given simultaneous measurements of the surface at λ = 6 cm and λ = 20 cm, we may solve for the attenuation coefficient assuming αT_{atm} is large compared to $(1-\alpha)T_s$:

$$\alpha = -\beta - \sqrt{\beta^2 - \gamma}$$

where,

$$\beta = [eT_P - T_{atm}(2 - e)] / [2\,T_{atm}(1 - e)]$$

$$\gamma = [eT_P - T_B] / [T_{atm}(1 - e)]$$

where e is the emissivity found at a wavelength of 20cm. If $T_{atm} = T_P$, $\beta = -1$. In that case, allowing $0<\alpha<1$, γ must be positive and less than 1, implying that $eT_P>T_B>T_P$ (2e-1) . Values of T_B falling outside of this range indicate an error in one or more of our assumptions; namely, that the range of temperatures measured by the Pioneer Venus atmospheric probes correspond to the physical temperature for the indicated local area as established by the Pioneer Venus altimetry data; the emissivity is the same at λ = 6 cm and 20cm for every portion of the surface; $T_{atm} = T_P$ at all points on the observable surface; the measured values of T_B are the true brightness temperatures at λ = 6cm. The calibration error and deconvolution difficulties of the λ = 6 cm data prevent this procedure from being effective for the data presented here. However, more reliable measurements of the emissions at λ = 6 cm, if measured simultaneously at λ = 20 cm, would provide a determination of α at this wavelength.

Alternatively, if we solve equation 4.2 for α, assuming $T_{atm} = T_P$, we obtain,

$$\alpha = 1 - (1 - (T_B/T_p - e)/(1 - e))^{1/2}$$

We may then attempt to examine likely values of α at λ = 6 cm, at normal incidence. The mean T_B obtained from the visibility function of November 12, 1983 at λ = 6 cm is 635 ± 15 K. If we assume the globally averaged emissivity of the surface is 0.84, then $\alpha = 0.08 \pm 0.07$, much smaller than that expected from the empirical relation $\alpha = 1 - e^{-15/\lambda^2} = 0.34$. If we examine α locally at Aphrodite where the brightness temperatures drop to less than 480 K and where the λ = 20 cm observations indicate emissivities of 0.62, then the implied α is 0.08.

4.2 Surface Temperatures and Emissivities of Mercury

Unlike Venus, we do not know the physical temperature of the surface of Mercury, as we lack *in situ* measurements of that quantity. Because we may calculate the solar insolation at the surface of Mercury at any point in its orbit, we may attempt to solve the equation of radiative transfer as a function of those material properties of the surface that control the heat flow out of the surface, such as thermal conductivity and heat capacity. However, given the high quality of the results obtained by Cuzzi (1974) and Morrison (1970) and the limited time span of the VLA observations presented in section 2.4.2, we don't feel we could have improved on their determinations. Additional observation of Mercury at a variety of solar illuminations could provide highly accurate estimates of Mercury's thermal parameters, but that is beyond the intended scope of this thesis. We may make a crude estimate of the physical temperature of the surface of Mercury if we assume a uniform value for the emissivity. Of course, as indicated by ground based radar measurements (Zohar and Goldstein, 1974), and lunar analogy, we expect there to be variations in the emissivity; but we will assume that they are small in comparison with other, more pronounced effects, such as solar heating. In which case, we may simply assume a value of the emissivity and solve for T_p:

$$T_P = T_B / e.$$

The degree of polarization indicates a dielectric constant of 2.1 for the surface of Mercury which corresponds to an emissivity at normal transmission of 0.958 . The physical temperature corresponding to the contours of figures 2-25 and 2-29 were then calculated and are listed in the legend. The maps indicate the physical temperture reached as high as 440° K at λ = 2 cm on April 4, 1985, and as high as 410° K at λ = 6 cm on April 5, 1985. Physical temperatures at the coolest portions of the planet reached as low as 100° K at λ = 2 cm and 200° K at λ = 6 cm. See figure 4-4 for a comparison of the

brightness temperatures at these wavelengths. Figure 4-4, which is a plot of both the $\lambda = 6$ cm and $\lambda = 2$ cm data, clearly shows that while there is a larger change in average brightness temperature a $\lambda = 6$ cm (100 K versus 60 K at $\lambda = 2$ cm), the change in T_B is more clearly defined and abrupt at $\lambda = 2$ cm. We expect the emissions at $\lambda = 2$ cm to reflect the change in illumination more than the $\lambda = 6$ cm emissions, due to the shallower depth from which the emissions originate.

Infrared observations by the Mariner 10 spacecraft at 45 μm indicated that the minimum predawn surface temperature was 93 K, assuming an emissivity of 0.9 (Chase et al, 1976). Observations at 11 μm showed a rapid rise in surface temperature beyond the terminator. These results are not inconsistent with the VLA results. We note, however, that Mercury's position in its orbit was not identical for both the VLA and Mariner 10 observations. Small scale thermal structure was noted by the Mariner 10 radiometer between longitudes of 220° and 270° that correspond generally with the enhanced brightness temperatures discernable in figure 2-19 and 2-23. A cool IR minimum found by the Mariner 10 radiometer at a longitude of 182° and a latitude of +21° is not excluded by the VLA data.

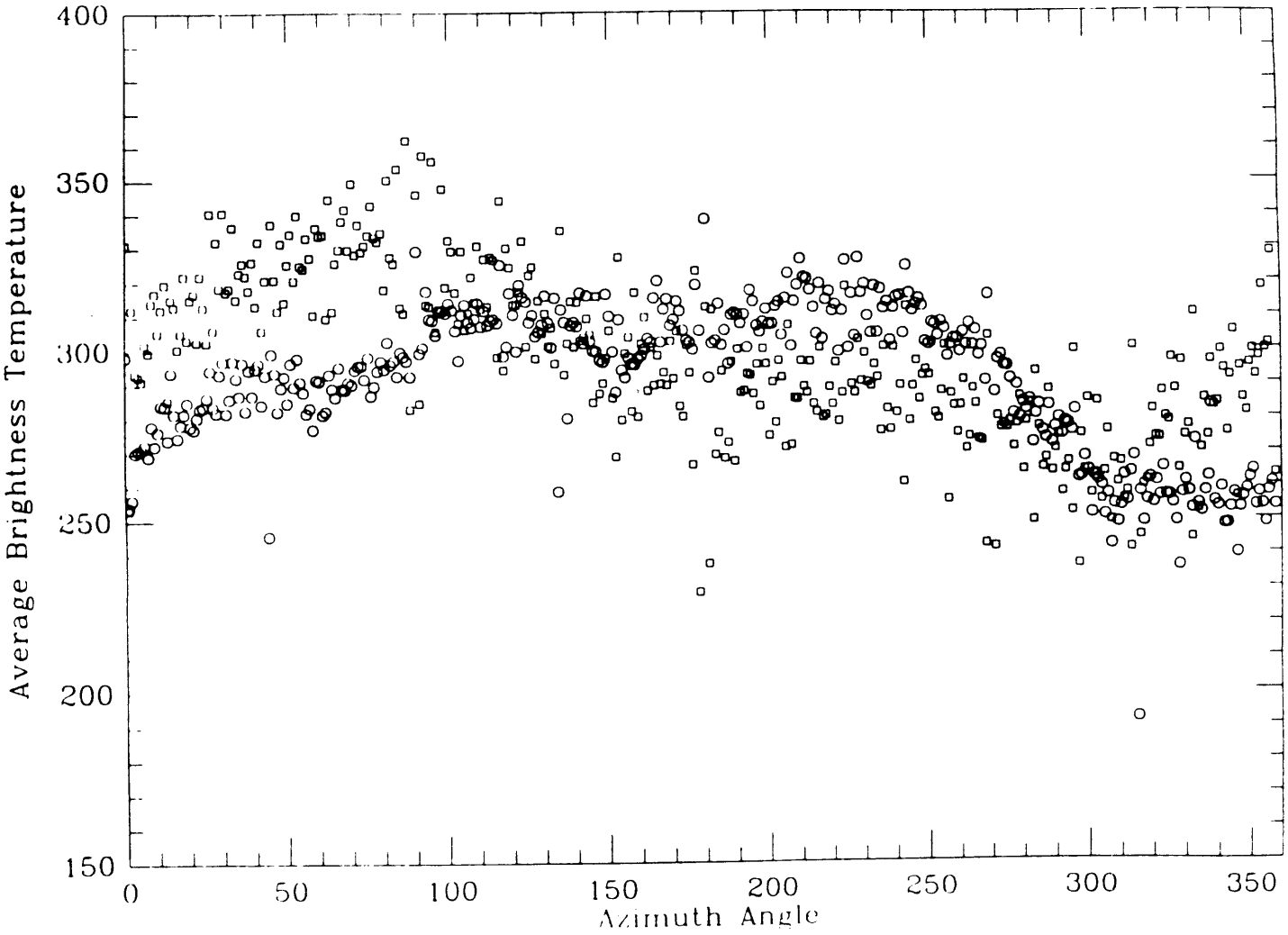


Figure 4-4
Average brightness temperature versus azimuth angle counterclockwise from South for both Mercury observations (λ = 6 cm and λ = 2 cm). Circles indicate λ = 2 cm data, while boxes indicate λ = 6 cm data.

4.3 Physical Interpretation of the Results

4.3.1 Comparison with Radar Measurements

In order to better understand and constrain models of the characteristics of the surfaces of Venus and Mercury that produce the observed radio emissions, radar measurements must be invoked. We have already used the topographic map obtained by the Pioneer Venus radar altimeter to ascertain the regional morphology of the Venus surface at those locations where we have obtained data (see Section 4.1). Radar scattering characteristics and reflectivity further constrain the determinable properties of the surface.

Specifically, we observe that the Hagfors Scattering Law (Hagfors, 1970) is a good approximation to the observed Pioneer Venus radar echo strengths, and indicates that rms slopes ranging from 1° to over 10° are present on the surface (see figure 4 in Pettengill *et al*, 1980). We see that the highland areas of Venus tend to have much larger values of surface roughness than the rolling plains or lowlands, which are, in some areas, quite smooth.

The radar reflectivity, determined from the Pioneer Venus Radar measurements, has a global mean of 0.15± 0.03 (Pettengill, Chapman, and Ford, in preparation; Pettengill, Ford and Nozette, 1982). The highland areas of Venus, notably Maxwell Montes, Aphrodite Terra, and Beta Regio have measured reflectivities substantially above this mean value, and reach as high as 0.4 ± 0.1. The mean value for Theia Mons is $\rho = 0.28 \pm 0.07$ at rms surface slopes of $5.3 \pm 1^{\circ}$.

These regions of high rms surface slopes and high reflectivities correspond to regions of low emissivity, as measured by the Pioneer Venus radar (made during its radio noise calibration while pointing down at the planet) and by the VLA. These emissivities were calculated by using the global altitude measurements of the Pioneer Venus radar in conjunction with the thermal profile determination of the Pioneer Venus atmospheric probes to establish the physical termperature of the surface. The Pioneer Venus brightness temperature measurements indicate T_B's as low as 405 ± 30 K, corresponding to

emissivities as low as 0.54 ± 0.05 at the location of Aphodite Terra (Ford and Pettengill, 1983). The VLA determinations of the brightness temperatures of Maxwell and Aphodite indicate brightness temperatures as low as 410 ± 16 K for Maxwell, and 445 ± 44 K for Aphrodite, corresponding to emissivities of 0.56 ± 0.05 and 0.62 ± 0.07, respectively. We note that the requirements of detailed thermodynamic balance and conservation of energy lead to :

$$e(\theta) = 1 - \rho(\theta)$$

(where e is the emissivity, ρ is the reflectivity, and θ is the angle of emission or reflection) when averaged over all possible scattering angles (we note that the measurements of e and ρ are made under very different geometries).

Comparison of the radar reflectivity with the radio emissivity does, reassuringly, follow this relationship. We may attempt to explain the anomalous high reflectivities and correspondingly low emissivities caused by the behaviour of the Fresnel transmission coefficient as a function of dielectric constant ε.

At normal transmission, for a smooth homogenous sphere :

$$\sqrt{\varepsilon} = [1+\sqrt{1-e}\,] / [1-\sqrt{1-e}\,] \qquad (4.4)$$

The dielectric constant must be solved iteratively for large angles of transmission.

If the subsurface of the planet is not homogeneous, the emissivity may be reduced relative to what would be expected from equation 4.4. An analysis of the lunar surface brightness temperatures has shown that subsurface imhomogeneities (isotropic or layered) may explain the reduced emissivities of the lunar microwave emission spectrum at wavelengths less than 10 cm (Fisher and Staelin, 1977). However, given the close correspondence between the independently measured emissivities e and the radar

emissivities and high reflectivities (uncertain knowledge of α at $\lambda = 6$ cm and indeterminate accuracy of the data obtained at that wavelength on November 12, 1983 precluded a definitive determination of the emissivity at $\lambda = 6$ cm; However, the brightness temperature *is* significantly reduced at the location of Aphrodite), we will assume that equation 4.4 is valid to the extent that it indicates the effective bulk dielectric constant of the surface. The measured emissivities of Maxwell and Aphrodite indicate dielectric constants as large as 25 and 17, respectively, under this assumption.

See Section 4.3.3 for a possible physical explanation for values of ε's this large.

The mean value of the radio emissivity determined by the VLA, $e = 0.84 \pm 0.03$, corresponds very closely to that expected from the Pioneer Venus radar measurements of the globally averaged reflectivity $\rho = 0.15 \pm 0.03$ (Pettengill, Chapman, and Ford, in preparation) and yields a dielectric constant of 5.4 ± 1 .

The high brightness temperatures located to the Northeast ofAphrodite (see Section 2.4.2.1 and figures 2-11 and 2-14) are less than 2σ greater than the mean. If they are not an artifact associated with the reduced brightness temperatures of Aphrodite, their origin is not immediately apparent. If the physical surface temperature is, in fact, 735 K in these areas, emissivities greater than or equal to 1 are implied, which is not, of course, physically possible. The physical temperature would have to be elevated by upwards of 75 K to reduce the emissivity in these regions to the global average of 0.84, an increase that cannot totally be ruled out (although we note that the recent Soviet VEGA probes landed only slightly South of this region, and found no temperature anomaly). There is no means known to us by which the physical temperature could be realistically elevated by this amount.

Radar observations of the surface of Mercury have not been pursued as vigorously as those of Venus. However, Zohar and Goldstein (1974) have shown that variations in reflectivity are discernible. The VLA observations of Mercury (see section 2) are indeterminate in this respect, as most of the variations in brightness temperature may be

attributed to actual physical temperature gradients across the surface, associated with the direct and recent insolation of the warmer areas.

4.3.2. Comparison with Models of the Surfaces.

Various models have been constructed which attempt to explain the observed radio and radar measurements of the surface and atmosphere of Venus. Muhleman, Orton, and Berge (1979) describe a model consisting of a dielectric sphere surrounded by a multilayered atmosphere, and examine the model in the context of radio and radar data obtained at a variety of wavelengths. Iteratively derived parameters include the normal-incidence emissivity ($e = .8852 \pm 0.009$), the radar directivity ($g = 1.31 \pm 0.10$), the surface temperature ($T_p = 755$ K), the mean surface dielectric constant ($\varepsilon = 4.10 \pm 0.15$), and the surface pressure ($p_s = 91.4$ atm). Many of the values are slightly at variance with other, individual measurements of the quantities, but the model does provide an indication of phenomena that are not explained by our current state of knowledge of Venus' atmosphere and surface. For example, the model does not fit the brightness temperature observations at wavelengths greater than 20 cm., where the measured T_B is substantially reduced. Also, the polarization of emissions is much lower than that expected at wavelengths greater than 10 cm. A comparision of these results with those obtained by the Pioneer Venus mission and the results obtained at the VLA indicate both agreement and discrepancies. The physical temperature of the surface has been found by the Pioneer Venus atmospheric probes to be 735 K at mean altitude (Seiff *et al*, 1980). A reflectivity of 0.15 ± 0.03 (Pettengill, Chapman, and Ford, in preparation) is in fair agreement with the model, but the emissivity (calculated in section 4.1) of 0.84 ± 0.03 is in slight disagreement. The dielectric constant of $\varepsilon = 2.5 \pm 0.5$ as determined from the degree of polarization at large angles of transmission is apparently in better agreement with the model at $\lambda = 20$ cm than the figures quoted by Muhleman, Orton, and Berge (1979), but is still significantly smaller than that expected from the measured reflectivities and emissivities, and from the model. This may be a result of surface roughness. The degree of polarization at smaller angles of transmission (where, we caution, the polarization is smaller, and closer to the noise) indicates dielectric constants in better agreement with the radar results ($\varepsilon \sim 4$).

Because Mercury is a difficult target to observe, attempts to model its surface are not easy. However, Cuzzi (1974,1973), Cuzzi and Muhleman (1972), and Morrison, (1970, 1969) have developed thermal models for Mercury's surface, and have found its surface to be very similar to that of the moon, in terms of its dielectric constant, thermal parameters, and morphology. The VLA observations of Mercury described in section 2 were obtained primarily for the polarization measurements, but qualitatively, we see that the variation in brightness temperature over the disk at $\lambda = 2$ cm and $\lambda = 6$ cm is a function of the history of the solar insolation, as one might expect. The determination for the dielectric constant of 2.1 ± 0.2 from the degree of polarization is in good agreement with the value obtained by Cuzzi, but is smaller than the radar value of 2.9 (Pettengill, 1978). The value of the dielectric constant of the Moon determined from its polarization is similarly lower than that determined both from *in situ* measurements and from radar reflectivity measurements.

4.3.3. Physical Interpretations

The mean emissivity of the surface of Venus of e = 0.84 ± 0.03, implying a dielectric constant of 5.4 ± 1, is consistent with the values of commonly found rocks on Earth. Very porous surface materials typically have ε's of 2, while solid, dry terrestrial rocks have dielectric constants ranging from 5 (granites) up to 9 (basalts). Meteoritic material may have dielectric constants much larger than 9, owing to metallic and sulfide inclusions (Pettengill, Ford, and Nozette, 1982). The dielectric constant of loose lunar material is typically 2 to 3 (Evans and Hagfors, 1964).

The substantially lower emissivities found at the locations of Maxwell (0.57 ± 0.05) and Aphrodite (0.62 ± 0.07), implying dielectric constants as high as 24, may be explained by the presence within the rock at these highland locations of substantial amounts of conductive inclusions, of size much smaller than the wavelength (λ = 20 cm) (Pettengill, Ford, and Nozette, 1982). This effect has been observed in meteorites, where iron-nickel mixtures and sulfides have increased the real part of the dielectric constant up to 100 or more (Campbell and Ulrichs, 1969). Iron pyrite concentrations of 15 percent in the highland areas could explain the observed emissivities and reflectivities. Chemical erosion of the surface by the atmosphere would tend to transform the conductive minerals into gases and non-conductive materials, which could then be transported to the lower elevations by strong winds or other processes (Pettengill, Ford, and Nozette, 1982). Pettengill, Ford, and Nozette suggest that if the pyrites were present in the original crustal rock, their effect on the emissivities and reflectivities would be only apparent at the higher elevations where new surfaces are constantly exposed by erosion. Or, alternatively, the high concentrations of pyrites may preferentially occur in areas of past volcanic activity.

Fisher-Staelin models that have been proposed to explain the reduced emissivities of the lunar microwave emission spectrum at wavelengths less than 10 cm (Fisher and Staelin, 1977) predict that subsurface layering or the presence of subsurface inhomogeneities could result in a reduction in emissivity. However, the radar evidence

suggests that subsurface inhomogeneities are not preferentially located in the highland regions significantly in excess of other areas of the surface of Venus, while subsurface layering predicts a wavelength dependence that has not been observed (see section 4.3.1 for additional discussion). It is more likely, therefore, that the low emissivities are a result of a high dielectric material in the observed highland areas.

Low values of the mean surface dielectric constant for Venus, as inferred from the degree of polarization, have been observed by Muhleman, Orton, and Berge (1979). They postulate that this may be related to the falloff in the brightness temperature spectrum at long ($\lambda > 20$ cm) wavelengths. Surface roughness and the large variation in values measured azimuthally may also be qualitatively responsible. We found that the degree of polarization steadily decreases relative to the model towards larger angles of transmission. This may be a simple result of the shallower depth of the emissions at larger angles of transmission, and would imply that the upper layer of surface material produces the lower estimate of ε, while a denser layer of material produces the larger polarizations relative to the model at small angles of transmission. However, the signal to noise becomes progressively worse at smaller angles of transmission. The generally low estimates of ε from the degree of polarization (compared with the radar reflectivity and radio emissivity determinations) may be a result of surface roughness on a scale less than the observing wavelength, where the effect of diffusely scattered emissions would tend to reduce the degree of polarization. Radar observations have shown that surface undulations are relatively small at $\lambda = 20$ cm wavelength size scales.

The VLA Mercury observations show that further observations of this planet at a variety of wavelengths and solar illuminations may provide a valuable remote-sensing technique in understanding the exact physical characteristics of this planet's surface. The degree of polarization determination of the dielectric constant $\varepsilon = 2.1 \pm 0.2$ is consistent with previous Mercury and Lunar results, and the variation in brightness temperature is consistent qualitatively with that found for the Moon.

Chapter 5. Conclusions

The preceding pages have presented high resolution aperture synthesis maps of the thermal radio emission from the surfaces of Venus and Mercury. The data were obtained at the Very Large Array where, at wavelengths ranging from 2 cm to 20 cm, visibility measurements of the emission from these planets were made at the variety of projected spacings and orientations that 27 antennas in a 'Y' shaped array produce over a day. Unlike other sources of astronomical interest, *in situ* measurements have been made of many of the planets, allowing direct comparison of remote sensing techniques with direct physical measurements. We found, as expected, that the visibility measurements of the disks of the planets corresponded to that of the visibility function of a circular disk. Zero-spacing fluxes of Venus corresponded to T_B 's of 623 ± 28 K and 615 ± 45 K at λ = 20 cm, and 635 ± 15 K at λ = 6 cm.

Images of Venus made at both λ = 20 cm and λ = 6 cm indicate low emissivities for Maxwell Montes and Terra Aphrodite that are consistent with the high measured reflectivities of these regions (Pettengill, Ford, and Nozette, 1982). Emissivities as low as 0.56 were found for these areas. The average emissivity was found to be 0.84 ± 0.03. The illuminated portion of the disk was found to have T_B's 40 ± 10 K higher than the unilluminated side on October 3, 1983, when Venus was near greatest elongation. It is not obvious how the illumination could induce this large a variation in brightness temperature.

Observations of the emissions from Mercury found average brightness temperatures varying by 100 K at λ = 6 cm over the disk, and 60 K at λ = 2 cm. Zero spacing fluxes corresponding to T_B's of 320 ± 6 K and 337 ± 16 were measured at 2 cm and 6 cm wavelength, respectively, at inferior conjunction.

The Stokes I, Q, and U maps were combined to produce a map of the degree of polarization of the emissions from Venus and Mercury. Equation 3.5 was derived, which relates the degree of polarization to the angle of transmission of the emissions, and the dielectric constant of the surface. A comparison of the theory with the data indicates for

Mercury a dielectric constant of 2.1 ± 0.2 at a wavelength of 6 cm. For Venus, the comparison is not quite as simple, as there is a systematic deviation of the data from the model. However, $\varepsilon = 2.5 \pm 0.5$ appears to be a reasonable estimate at large angles of transmission. These values for ε are significantly smaller than estimates made from radar measurements and from the VLA emissivity measurements discussed earlier, possibly because of an increase in surface roughness at scale sizes less thatn the wavelength of the observations.

The low emissivities found at the locations of Maxwell and Aphrodite corroborate the interpretation that high dielectric constants are responsible for the high reflectivity of the highland regions of Venus, rather than subsurface layers or inhomogeneities. Substantial amounts of pyrites (or other conducting minerals) embedded in the highland surfaces could explain these results.

Appendix

A1. Rayleigh-Jeans Law

The brightness temperature of the VM maps (section 2.4) may be obtained by the Rayleigh-Jeans approximation to Planck's blackbody radiation law (Kraus, 1966) :

$$T_B = \lambda^2 B / 2k$$
$$= \lambda^2 S / 2k\Omega F$$
$$= 1540.8 \lambda^2_{cm} S_{Jy} / (F\vartheta^2_{pix}) \qquad (A.1)$$

Where F is the factor used in the conversions from VM maps to convolved VM maps; Ω is the solid area for each pixel; B is the brightness in units of W m^{-2} hz^{-1} $ster^{-1}$; S is the flux density in units of 10^{-26} W m^{-2} hz^{-1} ; k is Boltzmann's constant; ϑ_{pix} is the pixel width in arcseconds; and λ_{cm} is the wavelength in centimeters.

The brightness temperature may similarly be obtained from the measured visibilities by setting F to 1, and associating $\Omega = \pi\theta^2$ (where θ is the angular radius in arcseconds) with the angular solid area of the planet :

$$T_B = \lambda^2 S / 2k\pi\theta^2$$

or :

$$T_B = 1540.8 \lambda^2_{cm} S_{Jy} / \pi\theta^2$$

A2 Relationship between the Ratio of the Emission Coefficients and η

The inverse cotangent of the axial ratio of the polarization of the polarization ellipse is :

$$\eta = \cot^{-1} (E_t^p / E_t^n)$$

where E_t^p and E_t^n are the magnitudes of the transmitted **E** vectors parallel and normal to the plane of incidence, respectively (see figure 3-1). In general, the notation will be $\mathbf{E}_b^a$, where a is either n(ormal) or p(arallel), refering to the polarization of the wave with respect to the plane of incidence; and where b is either i(ncident), r(eflected), or t(ransmitted), denoting the corresponding **E** vector.

We are constrained at the boundary between the surface and the atmosphere of the planet by the requirement that the normal components of **D** and **B**, and the tangential components of **E** and **H**, of the electromagnetic waves emanating from its interior be continuous.

The radiation from the interior of the planet incident on the surface will not be polarized, as the radiation is thermal radiation from the planet's interior. However, any wave can be considered a superposition of two orthogonally polarized waves. Therefore, the incident radiation can be expressed as the superposition of waves polarized with their electric field vectors normal and parallel to the plane containing the incident, reflected, and transmitted waves (*i.e.* the plane of incidence). Application of the boundary condition at the surface results in Fresnel's equations, which express the relative magnitudes of the reflected and transmitted waves parallel and normal to the plane of incidence.

The coefficient of transmission is defined as the ratio of the average energy flux transmitted to that incident per unit time and per unit area at the interface (Lorrain and Corson, 1970):

$$T = \frac{S_t \bullet n}{S_i \bullet n}$$

where **S** is the average value of the Poynting vector and **n** is the unit vector normal to the interface. The Poynting vector, for incident and transmitted waves, may be expressed as :

$$S_t = 1/2 \sqrt{\varepsilon_2/\mu_2}\ E_t^2\ k$$

$$S_i = 1/2 \sqrt{\varepsilon_1/\mu_1}\ E_i^2\ k$$

where **k** is the unit vector in the direction of energy flow. ε and μ are the dielectric constant and magnetic permeability, respectively, of regions specified by the subscripts (see figure A-1). e may then be expressed as :

$$e = \frac{\sqrt{\varepsilon_2/\mu_2}\ E_t^2 \cos\theta_t}{\sqrt{\varepsilon_1/\mu_1}\ E_i^2 \cos\theta_t}$$

Finding the ratio of the transmission coefficients of waves polarized parallel to the plane of incidence to waves polarized normal to the plane of incidence yields :

$$\frac{e_n}{e_p} = \frac{[E_t^n]^2\ [E_i^p]^2}{[E_i^n]^2\ [E_t^p]^2}$$

The ratio E_i^p / E_i^n is approximately equal to one, as these incident waves will be refracted from near normal incidence by an interface incrementally deeper. In other words, the incident radiation is the unpolarized thermal black body radiation generated interior to the interface. Therefore, we find that :

$$e_n / e_p \approx \{E_t^n / E_t^p\}^2$$

This relates the ratio of the transmission coefficients normal and parallel to the plane of incidence to the square of the ratio of the normal and tangential components of the transmitted electric field vector. It follows that :

$$\eta = \cot^{-1} (e_p / e_n)^{1/2} \qquad (A.2)$$

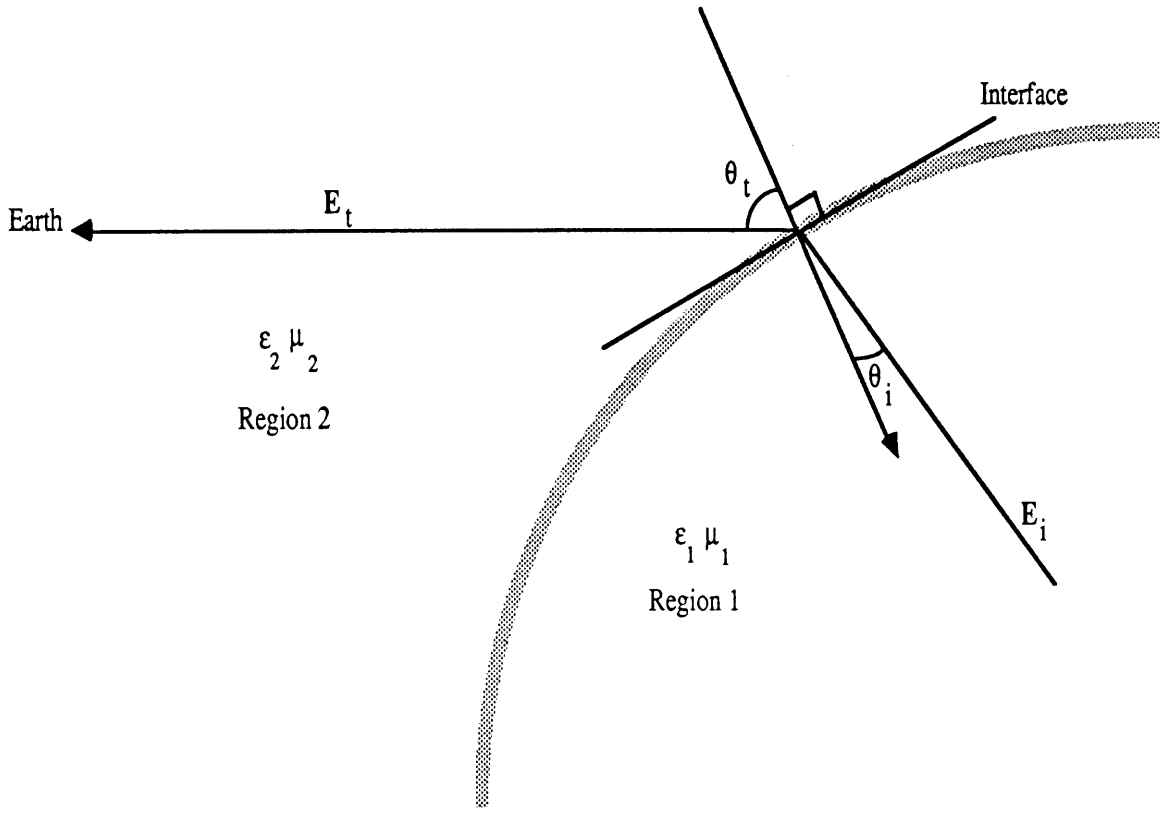


Figure A-1
Geometry of Transmission

A3. Corrections to λ = 6 cm Venus Data

If we assume likely approximate values for the emissivity of the surface of Venus and for the atmospheric absorption coefficients at $\lambda = 6$ cm and $\lambda = 20$ cm, we find that (from equation 4.1):

$$\frac{T_B^{20}}{T_B^{6}} = \frac{e(1 - \alpha_{20})^2 + \alpha_{20}(2 - \alpha_{20})}{e(1 - \alpha_6)^2 + \alpha_6(2 - \alpha_6)} \qquad \text{(A.3)}$$

where the surface emissivity e is assumed to be the same at both $\lambda = 6$ cm and $\lambda = 20$ cm, α_{20} is the atmospheric absorption coefficient at $\lambda = 20$ cm, and α_6 is the atmospheric absorption coefficient at $\lambda = 6$ cm. For values of e = 0.85, $\alpha_{20} = 0.03$, and $\alpha_6 = 0.3$; we have :

$$\frac{T_B^{20}}{T_B^{6}} = 0.93 \qquad \text{(A.4)}$$

Figure A-2 shows the dependence of this function on the assumed emissivity e and the absorption coefficients at $\lambda = 6$ cm and $\lambda = 20$ cm. This ratio is relatively independent of the likely values for α_{20} and α_6, but is significantly dependent on the emissivity e.

The observed data was in disagreement with this result by 8%, probably as a result of an overestimation of the total flux for the model disk by a similar factor. The brightness temperatures observed for Venus at $\lambda = 6$ cm were therefore reduced by this amount. The average brightness temperature of Venus inferred from the cleaned map (653 K) is then in better agreement with the brightness temperature implied by the visibility data (635 K), and with previous determinations of the average brightness temperature for Venus at $\lambda = 6$ cm (Berge, Muhleman, and Orton, 1972).

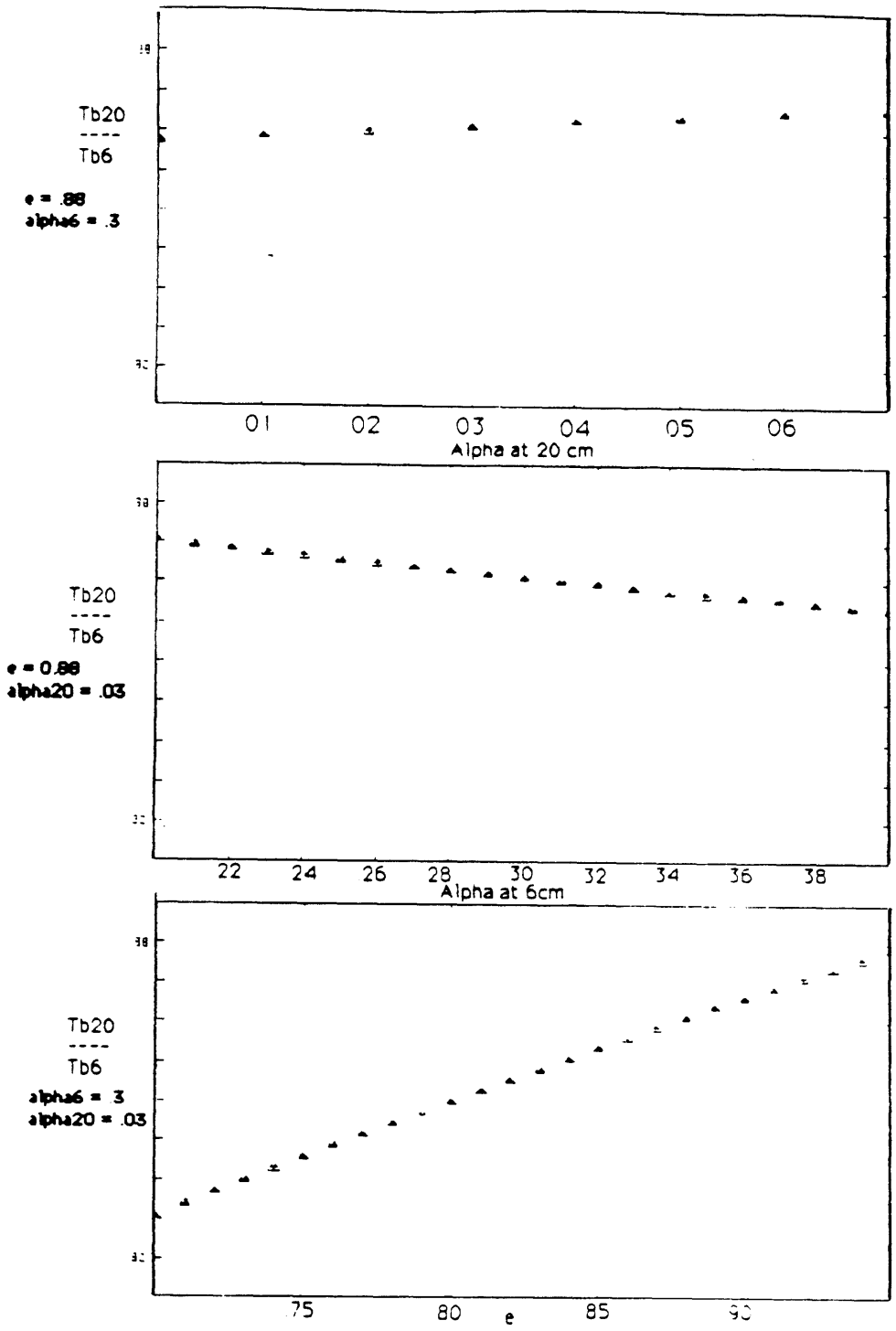


Figure A-2

The ratio of the expected brightness temperature at λ = 20 cm and at λ = 6 cm *versus* the atmospheric attenuation coefficient at a) λ = 20 cm and b) λ = 6 cm, and versus c) the emissivity of the surface.

A4 Calculated Visibilities of a Disk

Figures A-3, A-4, and A-5 are plots of the function of equation 2.3 . These plots correspond to the expected visibilites of emissions from a disk, for the indicated zero spacing fluxes.

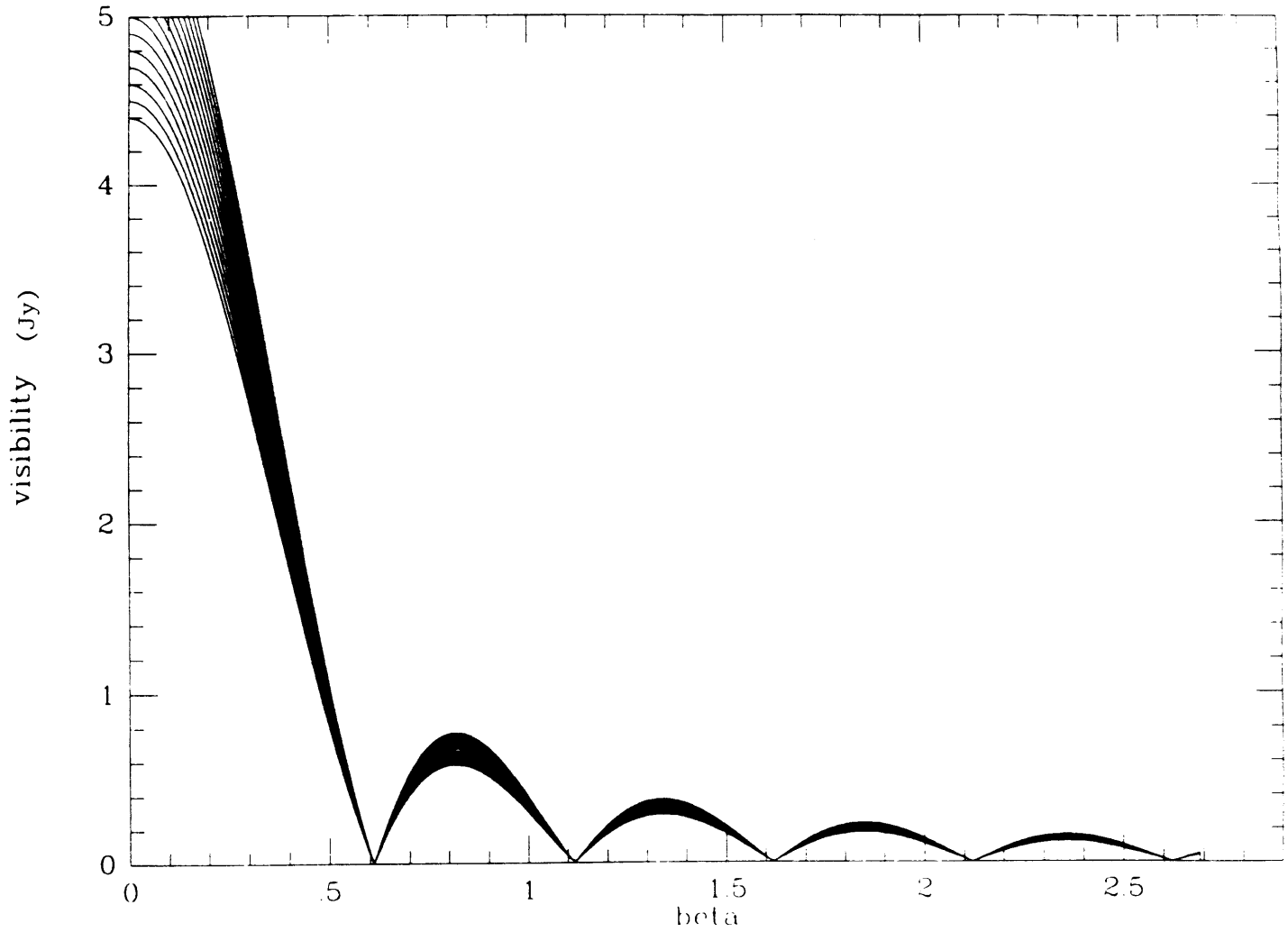


Figure A-3

Theoretical visibility function for a disk versus $\beta = yR/\lambda D$, where y is the projected interferometer spacing, λ is the wavelength, R is the radius of the planet, and D is the distance to the planet. Curves are for zero spacing fluxes of 4.4 to 5.8 Jy incremented 0.1 Jy.

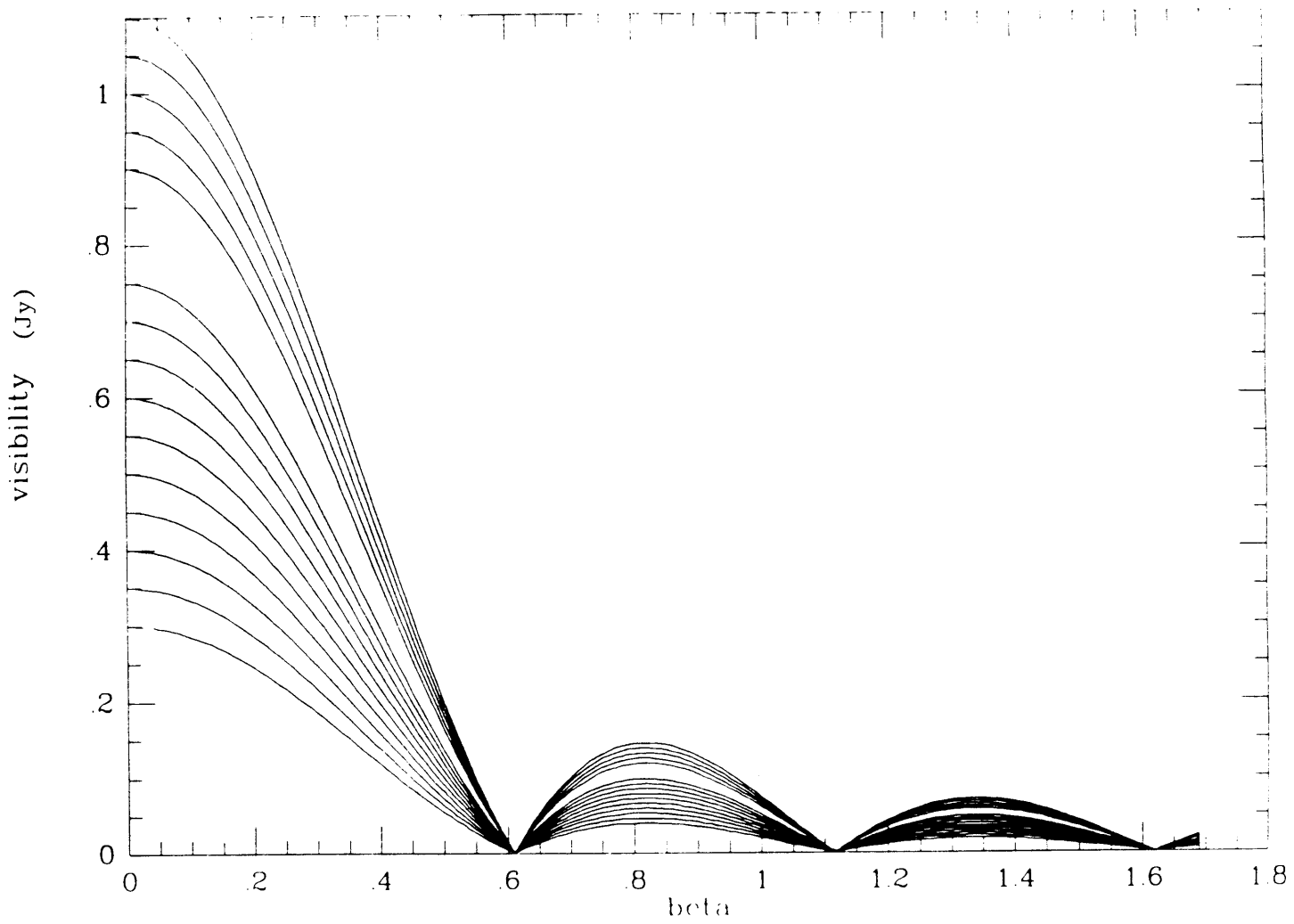


Figure A-4
Theoretical disk visibility function versus β for zero spacing fluxes of 0.3 to 0.75 Jy and 0.9 to 1.1 Jy incremented 0.05 Jy.

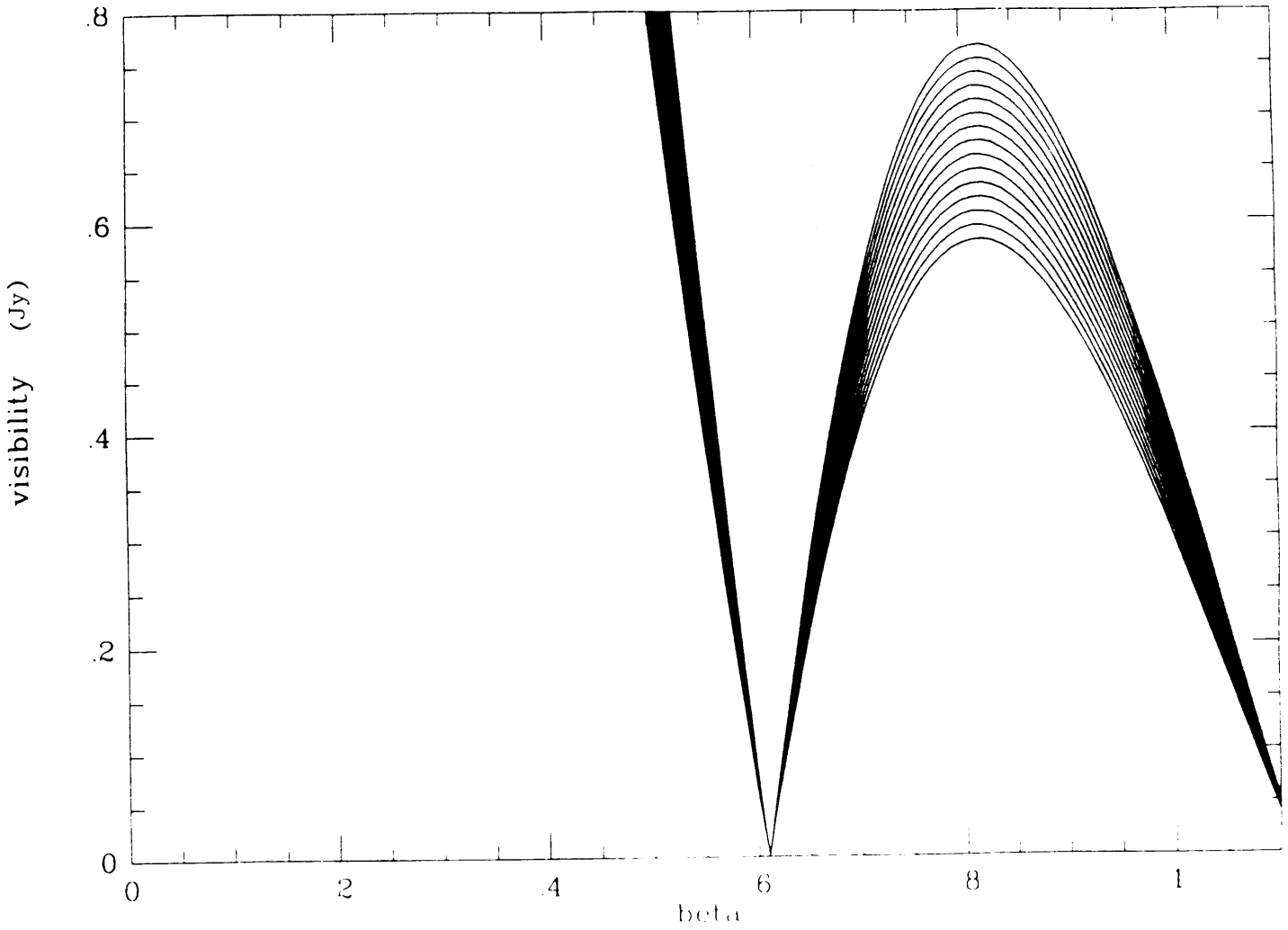


Figure A-5
Theoretical visibility versus β corresponding to figure 2-7, of zero spacing fluxes ranging from 4.4 to 5.8 Jy incremented 0.1 Jy.

References

Alexandrov, Yu.N.,Crymov, A.A., Kotelnikov, V.A., Petrov, G.M., Rzhiga, O.N., Sidorenko, A.I., Sinilo, V.P., Zakharov, A.I., Akim, E.L., Basilevski, A.T., Kadnichanski, S.A., and Tjuflin, Yu.S. (1986). Venus : Detailed Mapping of Maxwell Montes Region. *Science* **231**, 1271-1273.

Berge, G.L., Muhleman, D.O., and Orton, G.S. (1972). High resolution interferometric observations of Venus at three radio wavelengths. *Icarus* **17**, 675-681.

Blinn, J.C., and Conel, J.E. (1972). Microwave Emission from Geological Materials: Observations of Interference Effects. *Journal of Geophysical Research* **77**, 4366-4378.

Briggs, F.H., and Drake, F.D. (1972). Interferometric Observations of Mars at 21-cm Wavelength. *Icarus* **17**, 543-547.

Campbell, M.J., and Ulrichs, J. (1969). Electrical Properties of Rocks and Their Significance for Lunar Radar Observations. *Journal of Geophysical Research* **74**, 5867-5881.

Chase, S.C., Miner, E.D., Morrison, D., Munch, G., and Neugebauer, G. (1976). Mariner 10 Infrared Radiometer Results: Temperatures and Thermal Properties of the Surface of Mercury. *Icarus* **28**, 565-578.

Cimino, J.B., Elachi, C., Kliore, A.J., McCleese, D.J., and Patel, I.R. (1980). Polar Cloud Structure as Derived From the Pioneer Venus Orbiter. *Journal of Geophysical Research* **85**, 8082-8088.

Clark, B.G. (1980). An efficient Implementation of the Algorithm CLEAN. *Astron Astrophys.* **89**, 377-378.

Clark, R.N. (1979). Planetary Reflectance Measurements in the Region of Planetary Thermal Emission. *Icarus* **40**, 94-103.

Clark, B.G., and Kuz'min, A.D. (1965). The Measurement of the Polarization and Brightness Distribution of Venus at 10.6-CM Wavelength. *Astrophysical Journal* **142**, 23-44.

Condon, J.J., Jauncey, D.L., and Yerbury, M.J. (1973). The Brightness Temperature of Venus at 70 Centimeters. *The Astrophysical Journal* **183**, 1075-1080.

Cornwell, T.J. (1982). Image Restoration. In *Synthesis Mapping : Proceedings of the NRAO-VLA Workshop* (Thompson, A.R., and D'Addario, L.R., Eds.). NRAO, Greenbank, W. Virginia.

Cornwell, T.J., and Evans, K.F. (1985). A Simple Maximum Entropy Deconvolution Algorithm. *Astronomy and Astrophysics* **143**, 77-83.

Crane, P.C. (1984). Gain Codes and Map Artifacts II. *VLA Computer Memorandum* , No. 171.

Cuzzi, J.N. (1974). The Nature of the Subsurface of Mercury from Microwave Observations at Several Wavelengths. *Astrophysical Journal* **189**, 577-586.

Cuzzi, J.N. (1973). The Subsurface Nature of Mercury and Mars from Thermal Microwave Emission. Ph.D. Thesis. California Institute of Technology.

Cuzzi, J.N., and Muhleman D.O. (1972). The Microwave Spectrum and Nature of the Subsurface of Mars. *Icarus* **17**, 548-560.

Davies, M.E., Abalakin, V.K., Cross, C.A., Duncombe, R.L., Masursky, H., Morando, B., Owen, T.C., Seidelmann, P.K., Sinclair, A.T., Wilkins, G.A., and Tjuflin, Y.S. (1980). Report of the IAU Working Group on Cartographic Coordinates and Rotational Elements of the Planets and Satellites. *Celestial Mechanics* **22**, 205-230.

Davies, R.D., and Gardner, F.F. (1966). Linear Polarization of the Moon at 6, 11, and 21 cm Wavelengths. *Australian Journal of Physics* **19**, 823-836.

England, A.W. (1975). Thermal Microwave Emission from a Scattering Layer. *Journal of Geophysical Research* **80**, 4484-4496.

Epstein, E.E., and Andrew, B.H. (1985). Mercury: Thermal Emission at Radio Wavelengths. *Icarus* **62**, 448-457.

Eshleman, V.R., Muhleman, D.O., Nicholson, P.D., and Steffes, P.G. (1980). Comment on Absorbing Regions in the Atmosphere of Venus as Measured by Radio Occultation. *Icarus* **44**, 793-803.

Esposito, L.W., Winick, J.R., and Steward A.I. (1979). Sulfur Dioxide in the Venus Atmosphere: Distribution and Implications. *Geop'ysical Research Letters* **6**, 601-604.

Evans, J.V. (1969). Radar Studies of Planetary Surfaces. *Annual Review of Astronomy and Astrophysics* **7**, 201-248.

Evans, J.V., and Hagfors, T. (1964). On the Interpretation of Radar Reflections from the Moon. *Icarus* **3**, 151-160.

Fjeldbo, G., and Kliore, A.J. (1971). The Neutral Atmosphere of Venus as Studied with the Mariner V Radio Occultation Experiements. *The Astronomical Journal* **76**, 123-140.

Fomalont, E.B., and Wright, M.C.H. (1974). Interferometry and Aperture Synthesis. In *Galactic and Extragalactic Radio Astronomy* (Verscher, G.L., and Kellerman, K.I., Eds.). Springer-Verlag, 256-290.

Ford, P.G., and Pettengill, G.H. (1983). Venus: Global Surface Radio Emissivity. *Science* **220**, 1379-1381.

Gale, W., Liwshitz, M., and Sinclair, A.C.E. (1969). Venus: An Isothermal Lower Atmosphere? *Science* **164**, 1059-1060.

Golden, L.M. (1979). The Effect of Surface Roughness on the Transmission of Microwave Radiation through a Planetary Surface. *Icarus* **38**, 451-455.

Goldstein, R.M. (1972). Review of Surface and Atmosphere Studies of Venus and Mercury. *Icarus* **17**, 571-575.

Good, J.C., and Schloerb F.P. (1983). Limits on Venus' SO2 Abundance Profile from Interferometric Observations at 3.4 mm Wavelength. *Icarus* **53**, 1-25.

Hagfors, T. (1970). Remote Probing of the Moon by Infrared and Microwave Emissions and by Radar. *Radio Science* **5**, 189-227.

Hagfors, T., and Evans, J.V. (1968). Radar Studies of the Moon. *Radar Astronomy* , Evans, J.V., and Hagfors, T., Eds., McGraw-Hill, 219-273.

Heiles, C.E., and Drake, F.D. (1963). The Polarization and Intensity of Thermal Radiation from a Planetary Surface. *Icarus* **2**, 281-292.

Hjellming, R.M., and Basart, J.P. (1982a). The Theory of the Instrument. In *An Introduction to the NRAO Very Large Array*, NRAO.

Hjellming, R.M., and Basart, J.P. (1982b). The VLA Electronics System. In *An Introduction to the NRAO Very Large Array*, NRAO.

Hjellming, R.M., and Basart, J.P. (1982c). Array Control and Data Acquisition. In *An Introduction to the NRAO Very Large Array*, NRAO.

Hjellming, R.M.(1982). VLA Data Processing Systems. In *An Introduction to the NRAO Very Large Array*, NRAO.

Ingalls, R.P., and Rainville, L.P. (1972). Radar Measurements of Mercury: Topography and Scattering Characteristics at 3.8 cm. *The Astronomical Journal* **77**, 185-190.

Jackson, J.D. (1975) Classical Electrodynamics (2nd Edition). John Wiley and Sons, New York.

Janssen, M.A., and Klein, M.J. (1981). Constraints on the Composition of the Venus Atmosphere from Microwave Measurements near 1.35 cm Wavelength. *Icarus* **46**, 58-69.

Janssen, M.A., and Poynter, R.L. (1981). The Microwave Absorptio of SO2 in the Venus Atmosphere. *Icarus* **46**, 51-57.

Kaftan-Kassim, M.A., and Kellermann, K.I. (1967). Measurements of the 1.9 cm Thermal Radio Emission from Mercury. *Nature* , 272-273.

Kakar, R.K., Waters, J.W., and Wilson, W.J. (1975). Venus: Microwave Detection of Carbon Monoxide. *Science* **191**, 379-380.

Keihm, S.J. (1982). Effects of Subsurface Volume Scattering on the Lunar Microwave Brightness Temperature Spectrum. *Icarus* **52**, 570-584.

Keihm, S.J. (1984). Interpretation of the Lunar Microwave Brightness Temperature Spectrum: Feasibility of Orbital Heat Flow Mapping. *Icarus* **60**, 568-589.

Keihm, S.J., Langseth, M.G. (1975). Lunar Microwave Brightness Temperature Observatiosn Reevaluated in the Light of Apollo Program Findings. *Icarus* **24**, 211-230.

Keihm, S.J., and Langseth M.G. (1975). Microwave Emission Spectrum of the Moon: Mean Global Heat Flow and Average Depth of the Regolith. *Science* **187**, 64-66.

Kellermann, K.I. (1966). The Thermal Radio Emission from Mercury, Venus, Mars, Saturn, and Uranus. *Icarus* **5**, 478-490.

Kraus, J.D. (1966). Radio Astronomy. McGraw-Hill, New York.

Kroupenio, N.N. (1972). Some Characteristics of the Venus Surface. *Icarus* **17**, 692-698.

Landau, R. (1972). The 3.5-Micron Polarization of Mercury. *Icarus* **26**, 243-249.

Landau, R. (1982). A Comment on the Insolation at Mercury. *Icarus* **52**, 202-204.

Lorrain, P., and Corson, D. (1970). Electromagnetic Fields and Waves. W.H. Freeman and Company, San Francisco.

Masursky, H., Eliason, E., Ford, P.G., McGill, G.E., Pettengill, G.H., Schaber, G.G., and Schubert, G. (1980). Pioneer Venus Radar Results: Geology from Images and Altimetry. *Journal of Geophysical Research* **85**, 8232-8260.

McCord, T.B., and Adams, J.B. (1972). Mercury: Interpretation of Optical Observations. *Icarus* **17**, 585-588.

Moffat, P.H. (1972). Aperture Synthesis Polarimetry of the Moon at 21 cm.**160**, 139-154.

Morrison, D. (1969). Thermal Models and Microwave Temperatures of the Planet Mercury. *Research in Space Science* **292**, 1-70.

Morrison, D. (1970). Thermophysics of the Planet Mercury. *Space Science Reviews* **11**, 271-307.

Morrison, D., and Klein, M.J. (1970). The Microwave Spectrum of Mercury. *The Astrophysical Journal* **160**, 325-332.

Morrison, D., and Sagan, C. (1967). The Microwave Phase Effect of Mercury. *The Astrophysical Journal* **150**, 1105-1110.

Muhleman, D.O. (1972). Microwave Emission from the Moon. *Program of Aero. and Astro.* **28**,51-81.

Muhleman, D.O., Berge, G.L., and Orton, G.S. (1973). The Brightness Temperature of Venus and the Absolute Flux-Density Scale at 608 MHz. *Astrophysical Journal* **183**, 1081-1085.

Muhleman, D.O., Orton, G.S., and Berge, G.L. (1979). A Model of the Venus Atmosphere from Radio, Radar, and Occultation Observations. *Astrophysical Journal* **234**,733-745.

Murdock,T.L., and Ney, E.P. (1970). Mercury : the Dark Side Temperature. *Science* **170** , 535-537.

Murray, J.B., Dollfus, A., and Smith, B. (1972). Cartography of the Surface Markings of Mercury. *Icarus* **17**, 576-584.

Napier, P.J. and Crane, P.C. (1982). Signal-to-Noise Ratios. In *Synthesis Mapping : Proceedings of the NRAO-VLA Workshop* (Thompson, A.R., and D'Addario, L.R., Eds.). NRAO, Greenbank, W. Virginia.

Perley, R.A. (1985). A Step by Step Guide to VLA Data Calibration. *VLA Observers Reference Manual* , NRAO.

Pettengill, G.H. (1968) Radar Studies of the Planets. *Radar Astronomy* , Evans, J.V., and Hagfors, T., Eds., McGraw-Hill, 275-321.

Pettengill, G.H. (1978) Physical Properties of the Planets and Satellites from Radar Observations. *Annual Review of Astronomy and Astrophysics* **16**, 265-292.

Pettengill, G.H., Eliason, E., Ford, P.G., Loriot, G.B., Masursky, H., and McGill, G.E. (1980). Pioneer Venus Radar Results: Altimetry and Surface Properties. *Journal of Geophysical Research* **85**, 8261-8270.

Pettengill, G.H., Ford, P.G., and Nozette, S. (1982). Venus : Global Surface Radar Reflectivity. *Science* **217**, 640-642.

Pollack, J.B., and Sagan, C. (1965). Polarization of Thermal Emission from Venus. *Astrophysical Journal* **141**,1161-1183.

Schloerb, F.P., Muhleman, D.O., and Berge, G.L. (1976). Lunar Hear Flow and Regolith Structure Inferred from Interferometric Observations at a Wavelength of 49.3 cm. *Icarus* **29**, 329-341.

Seiff, A., Kirk, D.B., Young, R.E., Blanchard, R.C., Findlay, J.T., Kelly, G.M., and Sommer, S.C. (1980). Measurements of Thermal Structure and Thermal Contrasts in the Atmosphere of Venus and Related Dynamical Observations: Results from the Four Venus Probes. *Journal of Geophysical Research* **85**, 7903-7933.

Sramek, R.A. (1982). Map Plane - U,V Plane Relationships. In *Synthesis Mapping : Proceedings of the NRAO-VLA Workshop* (Thompson, A.R., and D'Addario, L.R., Eds.). NRAO, Greenbank, W. Virginia.

Steffes, P.G., and Eshleman, V.R. (1981). Sulfur Dioxide and other Cloud-Related Gases as the Source of the Microwave Opacity of the Middle Atmosphere of Venus. *Icarus* **46**, 127-131.

Thompson, A.R. (1982). Introduction and Basic Theory. In *Synthesis Mapping : Proceedings of the NRAO-VLA Workshop* (Thompson, A.R., and D'Addario, L.R., Eds.). NRAO, Greenbank, W. Virginia.

Tyler, G.L. (1968). Brewster Angle of the Lunar Crust. *Nature* **219**,1243-1244.

Ulich, B.L., Dickel, J.R., and de Pater, I. (1984). Planetary Observations at a wavelenth of 1.32 mm. *Icarus* **60**, 590-598.

Ulrichs, J., and Campbell, M.J. (1969). Radiative Heat Transfer in the Lunar and Mercurian Surfaces. *Icarus* **11**, 180-188.

Van Hemelrijck, E. (1983) On the Variations in the insolation at Mercury Resulting from oscillations of the Orbital Eccentricity. *Moon and the Planets*, **29**, 83-93.

Vilas, F., and McCord, T.B. (1976). Mercury: Spectral Reflectance Measurements (0.33 - 1.06 μm) 1974/75. *Icarus* **28**, 593-599.

Warnock, W.W., and Dickel, J.R. (1972). Venus : Measurements of Brightness Temperatures in the 7-15 cm Wavelength Range and Theoretical Radio and Radar Spectra for a Two-layer Subsurface Model. *Icarus* **17**, 682-691.

Wood, C.A., and Head, J.W. (1976). Comparison of impact basins on Mercury, Mars, and the Moon. *Proc. Lunar Sci. Conf. 7th*, 3629-3651.

Zohar,S., and Goldstein, R.M. (1974). Surface Features on Mercury. *Astrophysical Journal* **79**, 85-91

Biographical Note

Bruce Douglas Chapman was born (along with a twin sister, Debbie) in San Francisco, California on March 3, 1959. He attended public schools in California, New Mexico, Illinois, Colorado, and Arizona before enrolling at the University of California at Berkeley in 1977. He graduated with degrees in physics and astronomy in December, 1981. Before attending MIT in the fall of 1982, he worked at UC Berkeley's Radio Astronomy Laboratory. In June, 1983, he married Andrea Ong.